

Searches for the Anomalous Photon Polarisation in Radiative B Decays at LHCb

THÈSE N° 7339 (2016)

PRÉSENTÉE LE 18 NOVEMBRE 2016
À LA FACULTÉ DES SCIENCES DE BASE
LABORATOIRE DE PHYSIQUE DES HAUTES ÉNERGIES 3
PROGRAMME DOCTORAL EN PHYSIQUE

ÉCOLE POLYTECHNIQUE FÉDÉRALE DE LAUSANNE

POUR L'OBTENTION DU GRADE DE DOCTEUR ÈS SCIENCES

PAR

Zhirui XU

acceptée sur proposition du jury:

Prof. F. Mila, président du jury
Prof. T. Nakada, directeur de thèse
Dr B. Pietrzyk, rapporteur
Prof. L. Garrido, rapporteur
Dr J. Van Hunen, rapporteur



ÉCOLE POLYTECHNIQUE
FÉDÉRALE DE LAUSANNE

Suisse
2016

Acknowledgements

The work of this thesis would have not been done without tremendous help from many people in the LHCb collaboration directly and indirectly. I would like to use this limited page to express my gratitude to some of you who directly contributes to this thesis.

To Prof. Tatsuya Nakada, the supervisor and a role model. Thanks for the maximal freedom you have offered to me to explore the physics world and to work independently.

To Dr. Guido Haefeli, a guide, a friend and a mentor. Thanks for teaching me detector techniques and slacklining skills. Thanks for all the discussions on everything.

To Dr. Albert Puig, Dr. Maurizio Martinelli, Dr. Fatima Soomro and Dr. Fred Blanc for offering me numerous help with the analyses, softwares and everything else. Special thanks to Dr. Albert Puig for being there to offer help on everything all the past four years.

To all the colleagues on $B_s^0 \rightarrow \phi\gamma$ analysis. We have been through both good and bad times in the past three years working together on this analysis. Especially this experience is invaluable to me.

To all the people from the radiative decays working group for the numerous help on both analyses. Special thanks to Dr. Olivier Deschamps, for all the help on the analyses and the help on the postdoc searches.

To Dr. Albert Puig, Dr. Preema Pais, Prof. Karim Trabelsi, Dr. Maurizio Martinelli, Dr. Arantza Oyanguren and Dr. Manuel Schiller for helping me to improve the theis writing.

To Maxime Schubiger, Brice Maurin and Dr. Manuel Schiller for translating the abstract to French and German.

To all the members of the jury, Prof. Frédéric Mila, Prof. Lluís Garrido, Dr. Bolek Pietrzyk, Dr. Jeroen van Hunen.

To all the colleagues from LPHE. You all are part of my life in the past four years. Thanks for all the wonderful time we have spent together. Special thanks to our secretaries Erika Lüthi and Esther Hofmann for all the help you have offered to me. Special thanks also to Rita Gianì for inviting me to Sicily for a wonderful summer vocation, all the owesome people, tasty food and beautiful views, the volcano and the sea.

To my dearest mister Dr. Manuel Schiller, for your love.

To my mother and brothers as always.

Lausanne, October 12, 2016

Zhirui

Abstract

This thesis is exploring the measurements of the photon polarisation in radiative B decays at LHCb, which are mediated through $b \rightarrow s\gamma$ transitions. To ensure optimal physics performance, procedures to align the LHCb detector and to monitor the alignment quality over time are presented.

Using data corresponding to an integrated luminosity of 3 fb^{-1} , collected in the year of 2011 at the centre-of-energy $\sqrt{s} = 7 \text{ TeV}$ and the year of 2012 at $\sqrt{s} = 8 \text{ TeV}$ in proton-proton collisions, the photon polarisation parameter A^Δ , which is related to the ratio of right- over left-handed photon polarisation amplitudes in $b \rightarrow s\gamma$ transitions, is measured by performing an untagged time-dependent analysis of more than 4000 $B_s^0 \rightarrow \phi\gamma$ decays. From an unbinned simultaneous fit to the $B_s^0 \rightarrow \phi\gamma$ and the control channel $B^0 \rightarrow K^{*0}\gamma$ data samples, a value of

$$A^\Delta = -0.98^{+0.46}_{-0.52}(\text{stat.})^{+0.23}_{-0.20}(\text{syst.}),$$

is measured. This result is compatible with the Standard Model (SM) expectation of $A_{\text{SM}}^\Delta = 0.047^{+0.029}_{-0.025}$, within two standard deviations.

Furthermore, a study of the feasibility of measuring the photon polarisation in $B^+ \rightarrow \phi K^+ \gamma$ decays is performed. Background from $B^+ \rightarrow K^+ K^+ K^- \pi^0$ decays form the main experimental difficulty for the selection of signal candidates when the calorimetric photons are used for decay reconstruction, but fitting the γ/π^0 separation variable can disentangle effectively the signal from these backgrounds. About 1400 signal $B^+ \rightarrow \phi K^+ \gamma$ decay candidates are reconstructed. No clear evidence of resonances in the ϕK^+ -system is found, thus, the chance of measuring the photon polarisation in this decay is slim. When using converted photons, their good momentum resolution allows the B mass to act as a good discriminating variable to separate signal from $B^+ \rightarrow K^+ K^+ K^- \pi^0$ decays. In this case, 53 ± 17 signal candidates are found, where the uncertainty is purely statistical. This result is consistent with the expected number of signal events when correcting the yield obtained from calorimetric photons with the photon conversion rate, the reconstruction efficiency and the $K^+ K^-$ mass range.

In addition, the direct CP asymmetry in the $B^+ \rightarrow \phi K^+ \gamma$ decay amplitudes is measured to be

$$A_{CP}(B^+ \rightarrow \phi K^+ \gamma) = (1.6 \pm 2.1(\text{stat.}) \pm 0.7(\text{syst.}))\%.$$

This value is consistent with the SM prediction of $-(0.1 - 1)\%$.

Key words: LHC, LHCb, B physics, polarisation, CP violation, rare decay, radiative decay

Zusammenfassung

Diese Arbeit untersucht eine Messung der Photonpolarisation in radiativen B -Zerfällen bei LHCb, die durch $b \rightarrow s\gamma$ -Übergänge vermittelt werden. Um optimale Bedingungen bei der Datennahme und -auswertung sicherzustellen, werden Prozeduren zur Detektorausrichtung und zur Überwachung von deren zeitlicher Stabilität vorgestellt.

Mit einem Datensatz entsprechend einer Luminosität von 3 fb^{-1} , der in den Jahren 2011 mit einer Schwerpunktsenergie von $\sqrt{s} = 7 \text{ TeV}$ und 2012 bei $\sqrt{s} = 8 \text{ TeV}$ in Proton-Proton-Kollisionen genommen wurde, wird der Photonpolarisationsparameter A^Δ , der mit dem Verhältnis der rechts- zu linkshändigen Photonpolarisationsamplituden in $b \rightarrow s\gamma$ -Übergängen zusammenhängt, in einer zeitabhängigen ungetaggten Analyse von mehr als 4000 $B_s^0 \rightarrow \phi\gamma$ Zerfällen gemessen. Aus einem ungebinnten simultanen Fit im Signalkanal und dem Kontrollkanal $B^0 \rightarrow K^{*0}\gamma$ erhält man einen Wert von

$$A^\Delta = -0.98^{+0.46}_{-0.52}(\text{stat.})^{+0.23}_{-0.20}(\text{syst.}).$$

Dieses Resultat ist innerhalb von zwei Standardabweichungen mit der Erwartung für das Standardmodell (SM) von $A_{SM}^\Delta = 0.047^{+0.029}_{-0.025}$ kompatibel.

Ausserdem enthält diese Arbeit eine Machbarkeitsstudie über die Messung der Photonpolarisation in dem Kanal $B^+ \rightarrow \phi K^+ \gamma$. Wenn Photonkandidaten aus dem Kalorimeter genutzt werden, ist der Untergrund aus $B^+ \rightarrow K^+ K^+ K^- \pi^0$ -Zerfällen die größte experimentelle Schwierigkeit in der Selektion der Signalkandidaten. Ein Fit an eine γ/π^0 -Separationsvariable kann das Signal von diesem Untergrund effektiv unterscheiden. Etwa 1400 Signalkandidaten werden im Zerfall $B^+ \rightarrow \phi K^+ \gamma$ rekonstruiert. Es gibt keine klaren Hinweise auf das Vorhandensein einer Resonanz im ϕK^+ -System, weswegen die Chance, die Photonpolarisation in diesem Zerfall zu messen, klein ist. Für Konversionsphotonen erlaubt es deren gute Impulsauflösung, das Signal vom $B^+ \rightarrow K^+ K^+ K^- \pi^0$ Untergrund in der B -Masse zu trennen. In diesem Fall findet man 53 ± 17 Signalkandidaten, wobei die Unsicherheit hier nur den statistischen Anteil berücksichtigt. Dies ist konsistent mit der erwarteten Anzahl von Zerfällen, wenn man den Ertrag aus dem Resultat mit Kalorimeterphotonkandidaten von oben auf Konversionsrate, Rekonstruktionseffizienz und den $K^+ K^-$ -Massenbereich korrigiert.

Desweiteren wurde die direkte CP -Asymmetrie in $B^+ \rightarrow \phi K^+ \gamma$ zu

$$A_{CP}(B^+ \rightarrow \phi K^+ \gamma) = (1.6 \pm 2.1(\text{stat.}) \pm 0.7(\text{syst.})\%$$

gemessen. Dies stimmt mit der SM-Erwartung von $-(0.1 - 1)\%$ überein.

Zusammenfassung

Stichwörter: LHC, LHCb, *B*-Physik, Polarisation, *CP*-Verletzung, seltene Zerfälle, radiativer Zerfall

Résumé

Cette thèse étudie la polarisation du photon dans les désintégrations radiatives des mésons B à LHCb via la transition $b \rightarrow s\gamma$. Afin d'assurer une performance optimale des processus physiques, des procédures pour aligner le détecteur LHCb et vérifier sa stabilité temporelle sont présentées.

En utilisant des données provenant de collisions proton-proton et correspondant à une luminosité intégrée de 3 fb^{-1} , collectées en 2011 avec une énergie de centre de masse de $\sqrt{s} = 7 \text{ TeV}$ et en 2012 de $\sqrt{s} = 8 \text{ TeV}$, le paramètre de la polarisation du photon A^Δ , relié au rapport des amplitudes droite et gauche de la polarisation du photon, est mesuré par une analyse dépendante en temps de plus de 4000 désintégrations $B_s^0 \rightarrow \phi\gamma$, dont la saveur n'est pas déterminée. En faisant une analyse statistique simultanée de $B_s^0 \rightarrow \phi\gamma$ et du canal de contrôle $B^0 \rightarrow K^{*0}\gamma$, une valeur de

$$A^\Delta = -0.98_{-0.52}^{+0.46}(\text{stat.})_{-0.20}^{+0.23}(\text{syst.}),$$

est mesurée. Ce résultat est compatible avec la valeur prédite par le modèle standard de $A^\Delta = 0.047_{-0.025}^{+0.029}$ à deux déviations standard près.

De plus, une étude de faisabilité de la mesure de la polarisation du photon dans les désintégrations $B^+ \rightarrow \phi K^+ \gamma$ est présentée. Le bruit de fond provenant des désintégrations de $B^+ \rightarrow K^+ K^+ K^- \pi^0$ est la principale difficulté expérimentale pour sélectionner le signal lorsque des photons provenant du calorimètre sont utilisés dans la reconstruction. Toutefois, l'étude de la variable de séparation entre γ et π^0 permet de séparer efficacement le signal du bruit de fond. Environ 1400 candidats du signal $B^+ \rightarrow \phi K^+ \gamma$ sont reconstruits. Comme aucun indice de résonance dans le système ϕK^+ n'a été trouvé, la probabilité de mesurer la polarisation du photon dans cette désintégration est faible. En utilisant des photons convertis, leur bonne résolution de la quantité de mouvement permet d'utiliser la masse du méson B comme variable discriminante afin de séparer le signal des désintégrations $B^+ \rightarrow K^+ K^+ K^- \pi^0$. Dans ce cas, on trouve 53 ± 17 candidats de signal, où l'incertitude est uniquement statistique. Ce résultat est compatible avec le nombre d'événements de signal attendu une fois les corrections appliquées pour le taux de conversion des photons, l'efficacité de reconstruction et l'intervalle de masse invariante du système $K^+ K^-$.

Enfin, l'asymétrie CP directe dans les amplitudes de désintégrations du $B^+ \rightarrow \phi K^+ \gamma$ est mesurée et vaut :

$$A_{CP}(B^+ \rightarrow \phi K^+ \gamma) = (1.6 \pm 2.1(\text{stat.}) \pm 0.7(\text{syst.})\%.$$

Résumé

Cette valeur est compatible avec la prédiction du modèle standard de $-(0.1 - 1)\%$.

Mots clefs : LHC, LHCb, physique du B , polarisation, violation CP , désintégration rare, désintégration radiative

Contents

Acknowledgements	i
Abstract (English)	iii
Zusammenfassung (Deutsch)	v
Résumé (Français)	vii
List of figures	xiii
List of tables	xix
Introduction	1
1 Photon polarisation in radiative B decays	5
1.1 Radiative B decays via $b \rightarrow s\gamma$ transitions	5
1.2 Determination of the photon polarisation	7
1.3 Mixing-induced CP asymmetries in $B_s^0 \rightarrow \phi\gamma$ decays	8
1.4 CP violation in $B^+ \rightarrow \phi K^+ \gamma$ decays	9
2 The LHCb experiment	11
2.1 The LHCb detector	11
2.1.1 Tracking system	13
2.1.2 Particle identification of charged hadrons	17
2.1.3 The calorimeter system	18
2.1.4 The muon system	19
2.2 The LHCb trigger system	19
2.3 Event reconstruction and simulation framework	20
3 The LHCb tracker alignment	23
3.1 Tracker alignment in the vertical direction	23
3.2 Alignment and calibration framework	26
3.3 Tracker alignment monitoring	31

4	Study of the photon polarisation in $B_s^0 \rightarrow \phi\gamma$ decays	35
4.1	Event reconstruction and selection	35
4.1.1	Photon energy post-calibration	36
4.1.2	Trigger requirements	36
4.1.3	STRIPPING and offline selections	37
4.2	Signal lineshapes	38
4.3	Background contributions	40
4.3.1	Merged π^0 backgrounds	41
4.3.2	Baryonic radiative decays	42
4.3.3	Backgrounds with particle misidentifications	42
4.3.4	Backgrounds from partially reconstructed B decays	45
4.4	Fit on the reconstructed B mass spectra	48
4.4.1	Fit procedure	48
4.4.2	Fit to data	49
4.4.3	Validation of the mass fit model	49
4.5	Determination of A^Δ	52
4.5.1	Decay time fitter	52
4.5.2	Decay time resolution	54
4.5.3	Decay time acceptance	56
4.5.4	Decay time fit procedure	59
4.5.5	The dependence of the B decay time on its mass	61
4.5.6	The B^0 lifetime measurement	61
4.5.7	Validation of the fit procedure	62
4.5.8	Measurement of the A^Δ value	63
4.6	Systematic uncertainties	64
4.6.1	External parameters	65
4.6.2	Decay time acceptance	65
4.6.3	Models of the B mass distributions	65
4.6.4	Peaking background contribution	66
4.6.5	Correlation between B mass and decay time	66
4.7	Conclusion	67
5	CP violation in $B^+ \rightarrow \phi K^+ \gamma$ decays	71
5.1	Event reconstruction and selection	71
5.1.1	Trigger	72
5.1.2	STRIPPING and offline selection	72
5.1.3	Boosted decision tree	73
5.1.4	Particle identification	74
5.1.5	Merged π^0 background suppression	76
5.1.6	Background from partially reconstructed B decays	76
5.1.7	Invariant mass distributions of the selected events	77
5.2	Selection of $B^+ \rightarrow \phi K^+ \gamma$ decays	78

5.2.1	Selection of the ϕ state	79
5.2.2	Fit to the $\phi K^+ \gamma$ invariant mass distribution	79
5.2.3	Separation of the merged π^0 contribution from signals	82
5.3	Direct CP asymmetry measurement in the $B^+ \rightarrow \phi K^+ \gamma$ decay	84
5.4	Hadronic structures in ϕK invariant mass distribution	90
5.5	Photon polarisation measurement	92
5.5.1	Angular distribution in the $B^+ \rightarrow \phi K^+ \gamma$ decay	92
5.5.2	Extraction of the photon polarisation parameter	93
5.5.3	Subtraction of the merged π^0 background	94
5.5.4	Angular acceptance	96
5.5.5	Summary	96
5.6	Conclusion	97
6	Reconstruction of $B^+ \rightarrow \phi K^+ \gamma$ decays with converted photons	99
6.1	Reconstruction of the converted photons	99
6.2	STRIPPING and trigger selections	101
6.3	Offline selections	102
6.4	Background from partially reconstructed B decays	105
6.5	Signal and background models	107
6.6	Fit of the B invariant mass distributions	108
6.7	Conclusion	113
7	Conclusions	115
A	The STRIPPING lines	117
	Bibliography	129
	Curriculum Vitae	131

List of Figures

1	Constraints in the $(\bar{\rho}, \bar{\eta})$ plane from all available measurements.	2
2.1	Integrated luminosity collected by the LHCb experiment.	12
2.2	LHCb detector layout.	12
2.3	Top view of the placement of VELO modules.	13
2.4	VELO in open/closed state.	14
2.5	Schematic view of the TT.	14
2.6	Schematic view of the IT boxes and the geometry of an IT layer.	15
2.7	An isometric view of the first OT station and its front view.	15
2.8	A schematic illustration of the defined track types.	16
2.9	Cherenkov angle versus particle momentum for the RICH radiators and the reconstructed Cherenkov angle as a function of track momentum in the C_4F_{10} radiator.	17
2.10	Layout of calorimeter system.	18
2.11	The schematic of the overall LHCb trigger scheme.	19
3.1	Invariant mass distributions for $\Upsilon(1S)$, $\Upsilon(2S)$ and $\Upsilon(3S)$ with different alignment constants in Run I.	23
3.2	Displacement in y -axis for IT sectors with respect to the survey measurements in 2015 data.	25
3.3	Displacement in y for IT sectors with respect to the 2015 database.	25
3.4	Mean values of the unbiased residuals of the tracks from both the default procedure and the full procedure in 2016 data.	27
3.5	Schematic diagram of the LHCb trigger data-flow in Run I data-taking compared to the data-flow in Run II.	28
3.6	A finite state diagram defining the behaviour of the alignment tasks.	30
3.7	The convergence of the automatic alignment procedure for tracker in case of large misalignment at the starting point.	31
3.8	Tracker alignment variations in x -axis and z -axis respect to the start value for IT1 in each fill.	33
4.1	The reconstructed B invariant mass distributions of the $B^0 \rightarrow K^{*0} \gamma$ and $B_s^0 \rightarrow \phi \gamma$ candidates in data.	39

List of Figures

4.2	Fits of the reconstructed invariant mass distributions in the simulated $B^0 \rightarrow K^{*0}\gamma$ and $B_s^0 \rightarrow \phi\gamma$ samples.	40
4.3	The $K^{*0}\gamma$ invariant mass reconstructed in the simulated $B^0 \rightarrow K^{*0}\pi^0$ sample. .	41
4.4	Distribution of the reconstructed $K^{*0}\gamma$ invariant mass in the simulated $\Lambda_b^0 \rightarrow \Lambda^*\gamma$ sample.	42
4.5	Distribution of the reconstructed $\phi\gamma$ invariant mass in the simulated $\Lambda_b^0 \rightarrow \Lambda^*\gamma$ sample.	43
4.6	The $K^{*0}\gamma$ invariant mass distribution reconstructed in the simulated $B_s^0 \rightarrow \phi\gamma$ sample.	43
4.7	The $K^{*0}\gamma$ invariant mass distribution reconstructed in the simulated $B^0 \rightarrow \rho\gamma$ sample.	44
4.8	The $\phi\gamma$ invariant mass distribution reconstructed in the simulated $B^0 \rightarrow K^{*0}\gamma$ sample.	44
4.9	The $K^{*0}\gamma$ invariant mass distribution reconstructed in the simulated $B \rightarrow K_1(1270)(K^{*0}\pi)\gamma$ sample.	46
4.10	The $K^{*0}\gamma$ invariant mass distribution reconstructed in the simulated $B^0 \rightarrow K^{*0}\eta$ sample.	46
4.11	The $K^{*0}\gamma$ invariant mass reconstructed in (the sum of) $B \rightarrow D\rho$ simulated samples and $B^+ \rightarrow K_1(1270)^+(K^{*0}\pi^+)\eta$ simulated sample.	47
4.12	The $\phi\gamma$ invariant mass reconstructed in the simulated $B^+ \rightarrow \phi K^+\gamma$ sample. . . .	48
4.13	Invariant mass fits of the $B^0 \rightarrow K^{*0}\gamma$ and $B_s^0 \rightarrow \phi\gamma$ candidates in data.	49
4.14	Validation of the mass fit models.	51
4.15	Schematic diagram of a $B \rightarrow h^+ h^- \gamma$ decay.	52
4.16	The effective B lifetime resolution as a function of the per-event decay time resolution.	54
4.17	The calibration offset of the reconstructed B lifetime as a function of the per-event resolution.	55
4.18	The dependence of the B per-event resolution on the decay time.	56
4.19	Decay time acceptances from simulated samples.	57
4.20	High decay time acceptance parameter, $\delta\Gamma$, introduced at each reconstruction or selection step for $B_s^0 \rightarrow \phi\gamma$ and $B^0 \rightarrow K^{*0}\gamma$ decays.	59
4.21	Biases in the measured B^0 lifetime and A^Δ value from the upper decay time acceptance.	60
4.22	The reconstructed B decay time dependence on its reconstructed invariant mass in the simulated signal samples.	61
4.23	The decay time distributions in the background subtracted data samples for $B^0 \rightarrow K^{*0}\gamma$ and $B_s^0 \rightarrow \phi\gamma$ decays.	63
4.24	The decay time ratio between $B_s^0 \rightarrow \phi\gamma$ and $B^0 \rightarrow K^{*0}\gamma$	64
4.25	B decay time dependence on mass in the simulated background samples. . . .	67
4.26	B decay time dependence on mass in the combinatorial background.	68

5.1	The $K^+K^+K^-\gamma$ invariant mass distributions of the real data and simulated signal samples.	73
5.2	The BDT performance and its response distributions.	74
5.3	Figure of merit in bins of the BDT output and kaon PID cut.	75
5.4	Figure of merit, signal efficiency and purity as a function of the BDT cut and of the PID cut.	75
5.5	The calculated selection efficiencies and the background contaminations $C_{B \rightarrow \phi K \pi^0}$ to the signal $B^+ \rightarrow \phi K^+ \gamma$ decay as a function of the γ/π^0 separation variable cut using different simulated background samples.	76
5.6	The HOP mass versus the B flight distance χ^2	77
5.7	The effect of the HOP cut on the $K^+K^+K^-\gamma$ invariant mass distribution.	78
5.8	The K^+K^- and $K^+\gamma$ invariant mass distributions in the selected data sample.	78
5.9	The ϕ , $\phi K^+\gamma$, ϕK^+ and $K^+\gamma$ invariant mass distributions in data.	79
5.10	Fit of the invariant $\phi K^+\gamma$ invariant mass distribution in simulated $B^+ \rightarrow \phi K^+\gamma$ sample.	80
5.11	Fit of the invariant mass distribution of $\phi K^+\gamma$ for simulated $B^+ \rightarrow \phi K^{*0}$ sample.	81
5.12	Fit of the invariant mass distribution of $\phi K^+\gamma$ in simulated $B^0 \rightarrow \phi K^{*0}\gamma$ sample.	81
5.13	Fits on the invariant mass distribution of $\phi K^+\gamma$ in data.	82
5.14	Distributions of the γ/π^0 separation variable in the calibration samples of $B^0 \rightarrow K^{*0}\gamma$ decay and $D^0 \rightarrow K\pi\pi^0$ decay.	83
5.15	Fit of the γ/π^0 separation variable on the background subtracted data sample using the templates from calibration samples.	83
5.16	Distributions of the transverse momentum and the pseudorapidity of the merged π^0 s from the calibration samples.	84
5.17	The γ/π^0 separation variable distributions with and without the weights included in the merged π^0 calibration sample.	84
5.18	Fit of the γ/π^0 separation variable distributions for the data sample with the magnet polarity up (left) and down (right).	86
5.19	Fit of the reconstructed B invariant mass distributons.	87
5.20	Likelihood profile as a function of the A_{CP}^{raw} values.	88
5.21	The resolution and pull distributions of the A_{CP}^{raw} parameter obtained with 1000 pseudoexperiment data samples.	88
5.22	Measure $K^-\pi^+$ detection asymmetry as a function of the kaon momentum and the measured kaon momentum in the background subtracted $B^+ \rightarrow \phi K^+\gamma$ data sample.	88
5.23	The relative detection efficiency curves from the simulated samples.	90
5.24	The background subtracted ϕK^+ invariant mass distributions and the contamination of the merged π^0 background in each ϕK^+ mass bin.	91
5.25	Background subtracted ϕK^+ invariant mass distributions in a ϕ mass region and the ϕ sideband region.	91
5.26	Angle conventions for the decay $B^+ \rightarrow [\phi \rightarrow K^+(\vec{p}_1)K^-(\vec{p}_2)]K^+(\vec{p}_3)\gamma(\vec{p}_\gamma)$	93
5.27	Fits on the $\phi K\gamma$ invariant mass and the γ/π^0 separation variable distributions.	95

List of Figures

5.28	The angular distributions in the background subtracted data sample.	96
5.29	The angular acceptances for angles η , θ , θ^* and ϕ^* from the simulated sample.	97
6.1	The reconstructed invariant mass of the converted photons and the r - z coordinates of the conversion points in simulated $B^+ \rightarrow K^+ K^+ K^- \gamma$ sample using long tracks.	100
6.2	The reconstructed invariant mass of the converted photons and the r - z coordinates of the conversion points in simulated $B^+ \rightarrow K^+ K^+ K^- \gamma$ sample using downstream tracks.	100
6.3	The ratio of efficiencies of converted photons to calorimetric photons measured in data and simulation as a function of photon p_T	101
6.4	Distributions of reconstructed the invariant mass and p_T of the converted photons in the simulated $B^+ \rightarrow \phi K^+ \gamma$ and $B^+ \rightarrow \phi K^{*0}$ samples.	101
6.5	Distributions of the invariant mass and p_T of the reconstructed B candidates in the simulated $B^+ \rightarrow \phi K^+ \gamma$ and $B^+ \rightarrow \phi K^{*0}$ samples.	102
6.6	The p_T distributions of the converted photons and the invariant mass distribution of the $K^+ K^+ K^-$ -system reconstructed in the simulated $B^+ \rightarrow K^+ K^+ K^- \gamma$ sample with different trigger requirements.	103
6.7	The ROC curve and the BDT response distribution of the average of the 10 BDTs on the reserved test sample for DD.	104
6.8	The ROC curve and the BDT response distribution of the average of the 10 BDTs on the reserved test sample for LL.	104
6.9	Figure of merit for LL and DD in bins of the BDT output and the kaon PID cut.	105
6.10	The curves of the figure of merit, signal efficiency and purity as a function of the BDT cut and of the PID cut for LL.	105
6.11	The curves of the figure of merit, signal efficiency and purity as a function of the BDT cut and of the PID cut for DD.	106
6.12	The distribution of M_{HOP}^B versus the B flight distance χ^2 in data.	106
6.13	The reconstructed B invariant mass distributions in the simulated $B^+ \rightarrow K^+ K^+ K^- \gamma$ sample before and after applying HOP cut.	106
6.14	The reconstructed B invariant mass distributions in data before and after applying the HOP cut.	107
6.15	Fit of the invariant mass of $K^+ K^+ K^- \gamma_{e^+ e^-}$ in the simulated samples of $B^+ \rightarrow K^+ K^+ K^- \gamma$ and $B^+ \rightarrow \phi K^+ \gamma$ for LL.	107
6.16	Fit of the invariant mass of $K^+ K^+ K^- \gamma_{e^+ e^-}$ in the simulated samples of $B^+ \rightarrow K^+ K^+ K^- \gamma$ and $B^+ \rightarrow \phi K^+ \gamma$ for DD.	108
6.17	Fit of the invariant mass of $K^\pm K^+ K^- \gamma_{e^+ e^-}$ from simulated $B^+ \rightarrow \phi K^{*+}$, $B^+ \rightarrow \phi K_2^*(1430)^+$ and $B^+ \rightarrow \phi K^*(1680)^+$ samples.	109
6.18	The reconstructed $K^\pm K^+ K^- \gamma_{e^+ e^-}$ invariant mass distributions in the simulated $B^0 \rightarrow \phi K^{*0} \gamma$ sample.	110
6.19	The reconstructed $K^\pm K^+ K^- \gamma_{e^+ e^-}$ invariant mass distributions in the simulated $B_s^0 \rightarrow \phi \phi \gamma$ sample.	110

6.20 The reconstructed $K^+_{\text{slow}}K^-$ invariant mass versus the $K^+_{\text{fast}}K^-$ invariant mass distributions in data.	111
6.21 Fit of the invariant mass of $K^+K^+K^-\gamma_{e^+e^-}$ in data.	112
6.22 Likelihood profiles as a function of the fitted signal yields.	112

List of Tables

3.1	IT tracker vertical alignment results for 2015 data	24
3.2	IT tracker vertical alignment results for 2016 data	24
4.1	Fit results of the B invariant mass distributions from the simulated signal events.	39
4.2	Invariant mass fit parameters for the $B^0 \rightarrow K^{*0} \gamma$ and $B_s^0 \rightarrow \phi \gamma$ candidates in data.	50
4.3	The mean and sigma of Gaussian fits to the pull distributions from the pseudo-experiments.	50
4.4	Input values for the decay time fit, from HFAG 2016.	52
4.5	Average decay time resolution.	56
4.6	The parameters of the resolution functions fitted in the simulated samples. . .	57
4.7	Decay time acceptance parameters as fitted on the simulated samples.	58
4.8	The mean μ of Gaussian fits to the distributions of the fitted A^Δ values and sigma σ of Gaussian fits to the pull distributions for the 5 sets of pseudoexperiment samples.	63
4.9	List of systematic uncertainties on A^Δ	64
5.1	The number of signal N_{Signal} and the merged π^0 contamination $C_{\text{Merged } \pi^0}$ from the fit on the γ/π^0 separation variable distribution using the templates for merged π^0 s weighted by different simulated sample.	85
5.2	Fit parameters of the simultaneous fit on the B invariant mass distributions using the data samples with opposite charges and different magnet polarities. .	87
5.3	Systematic uncertainties on the measured A_{CP}^{raw}	89
5.4	Fitted yields of each component from the two-dimensional fit on the B invariant mass and the γ/π^0 separation variable.	95
6.1	Invariant mass fit parameters for the $B^+ \rightarrow K^+ K^+ K^- \gamma_{e^+ e^-}$ candidates in data. .	112
A.1	A list of cuts applied in the STRIPPING line StrippingB2KstGamma_B2VG. . . .	117
A.2	A list of cuts applied in the STRIPPING line StrippingB2PhiGamma_B2VG. . . .	118
A.3	A list of cuts applied in the STRIPPING line StrippingB2XGamma3pi.	119
A.4	A list of cuts applied in the STRIPPING line StrippingB2XGamma3pi_wCNV. . . .	120

Introduction

The observed universe is composed almost entirely of matter with little or no primordial anti-matter [1] whilst the big bang should have produced equal amounts of matter and antimatter. The numerical analysis of the imbalance in matter and antimatter in the observable universe demonstrates that the universe should be fundamentally matter-antimatter asymmetric [1, 2]. Charge-Parity (CP) violation is needed to produce the observed baryon number asymmetry in the universe [3].

In the Standard Model (SM), the complex phase of the Cabibbo-Kobayashi-Maskawa (CKM) matrix [4, 5] provides the only source of CP violation observable. The CKM matrix can be parametrised using three rotation angles and one phase. The standard parametrisation uses $\theta_{12}, \theta_{13}, \theta_{23}$ in $[0, \pi/2]$ and δ in $[-\pi, \pi]$ defined as

$$V_{CKM} = \begin{pmatrix} V_{ud} & V_{us} & V_{ub} \\ V_{cd} & V_{cs} & V_{cb} \\ V_{td} & V_{ts} & V_{tb} \end{pmatrix} = \begin{pmatrix} s_{12}c_{13} & s_{12}c_{13} & s_{13}e^{-i\delta} \\ -s_{12}c_{23} - c_{12}s_{13}s_{23}e^{-i\delta} & c_{12}c_{23} - s_{12}s_{13}s_{23}e^{i\delta} & c_{13}s_{23} \\ s_{12}s_{23} - c_{12}s_{13}c_{23}e^{i\delta} & -c_{12}s_{23} - s_{12}s_{13}c_{23}e^{i\delta} & c_{13}c_{23} \end{pmatrix}, \quad (1)$$

where s and c are abbreviations for $\sin\theta$ and $\cos\theta$, respectively. The Wolfenstein parametrisation [6] follows the observed hierarchy between the different matrix elements and introduces four real parameters λ , A , ρ and η :

$$V_{CKM} = \begin{pmatrix} 1 - \lambda^2/2 - \lambda^4/8 & \lambda & A\lambda^3(\rho - i\eta) \\ -\lambda - A^2\lambda^5(\rho + i\eta - 1/2) & 1 - \lambda^2/2 - (1/8 + A^2/2)\lambda^4 & A\lambda^2 \\ A\lambda^3[1 - (\rho + i\eta)(1 - \lambda^2/2)] & -A\lambda^2 - A\lambda^4(\rho + i\eta - 1/2) & 1 - 1/2A^2\lambda^4 \end{pmatrix} + \mathcal{O}(\lambda^6), \quad (2)$$

where the complex phase δ is encapsulated in a nonzero value of η . The parameters λ and A are relatively well known from semileptonic decays which provide V_{us} and V_{cb} . The unitary relation of the CKM matrix applied to the first and third columns $V_{ud}V_{ub}^* + V_{cd}V_{cb}^* + V_{td}V_{tb}^* = 0$ is referred to as the unitary triangle (UT). The UT is particularly related to B decays. It can be normalised by $V_{cd}V_{cb}^*$ and using the Wolfenstein parametrisation, the other two terms of

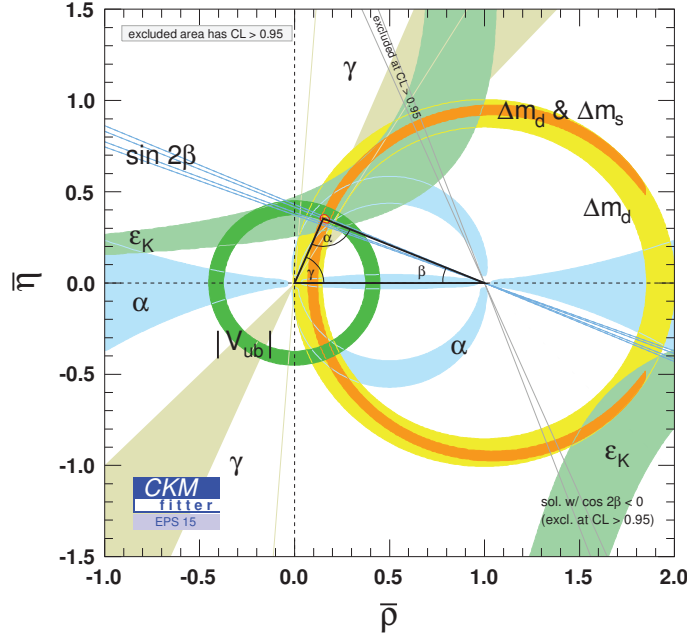


Figure 1: Constraints in the $(\bar{\rho}, \bar{\eta})$ plane from all available measurements. The red hashed region of the global combination corresponds to 68% CL. Figure from the CKMfitter website [7].

the UT can be rewritten as

$$\begin{aligned} -\frac{V_{ud}V_{ub}^*}{V_{cd}V_{cb}^*} &= (1 - \lambda^2/2)(\rho + i\eta) + \mathcal{O}(\lambda^4) = \bar{\rho} + i\bar{\eta} + \mathcal{O}(\lambda^4), \\ -\frac{V_{td}V_{tb}^*}{V_{cd}V_{cb}^*} &= 1 - (1 - \lambda^2/2)(\rho + i\eta) + \mathcal{O}(\lambda^4) = 1 - (\bar{\rho} + i\bar{\eta}) + \mathcal{O}(\lambda^4), \end{aligned} \quad (3)$$

where the apex of the UT has the coordinate $(\bar{\rho}, \bar{\eta})$. The three angles of the UT represent the complex phase of the combinations

$$\alpha = \arg\left(-\frac{V_{td}V_{tb}^*}{V_{ud}V_{ub}^*}\right), \quad \beta = \arg\left(-\frac{V_{cd}V_{cb}^*}{V_{td}V_{tb}^*}\right), \quad \gamma = \arg\left(-\frac{V_{ud}V_{ub}^*}{V_{cd}V_{cb}^*}\right). \quad (4)$$

A global fit [7, 8] that combines all available measurements related to the weak interaction processes is shown in Fig. 1.

Models of baryogenesis suggest that it is quantitatively insufficient if the complex phase of the CKM matrix is the only source of the CP violation [1, 2, 3]. The neutrino flavour mixing seen in the neutrino oscillations [9, 10], represents compelling experimental evidence for the incompleteness of the SM and is a clear sign of the existence of new physics beyond the SM. Several scenarios have been proposed for physics beyond the SM. Extensions of the SM generally contain new sources of CP violation. They introduce new particles, dynamics,

symmetries or even extra-dimensions at the TeV energy scale.

Studies of B , D and K decays [11] have yielded a detailed understanding of different aspects of the CKM paradigm and suggest promising places to look for new physics. The LHCb experiment has been designed to perform precision measurements of rare decays of b - and c -hadrons produced in proton-proton (pp) collisions at the LHC [12]. The primary goal of LHCb is to search for effects of new particles and forces beyond the SM. Rare decays of b - and c -hadrons provide a unique laboratory for these searches since in the SM these suppressed decays can only proceed through quantum-loops involving the exchange of virtual particles. New heavy degrees of freedom could lead to new amplitudes which would modify the measurable quantities. Confronting precision measurements to precise SM predictions allows to identify the new physics appearing as additional quantum corrections.

Radiative B meson decays are one of the “standard candles” of flavour physics and are especially distinctive for searches of physics beyond the SM [13]. The Flavour Changing Neutral Current (FCNC) process $b \rightarrow s\gamma$, suppressed by the Glashow-Iliopoulos-Malini (GIM) mechanism, was discovered by the CLEO experiment through the observation of the $B^0 \rightarrow K^{*0}\gamma$ decay [14]. The inclusive $b \rightarrow s\gamma$ branching ratio was first measured by the CLEO experiment [15] and has been followed by increasingly precise measurements by the BaBar [16, 17] and Belle [18] experiments. The measurements of the branching ratios provide constraints on new physics but suffer from large theoretical uncertainties in the hadronisation process, especially the exclusive hadronic matrix elements that are extremely difficult to calculate reliably. Measurement of the polarisation of the emitted photons in radiative decays via $b \rightarrow s\gamma$ transitions is expected to constrain the contribution from the right-handed component which is highly suppressed in SM and suffers little from hadronic uncertainties, thus making it a good observable to detect the existence of new physics [19, 20].

The structure of this thesis is organised as follows. Chapter 1 gives a short overview of the theoretical aspects of the photon polarisation measurements. A brief introduction to the LHCb experiment is presented in Chapter 2. Chapter 3 is dedicated to the alignment of the LHCb tracker performed during data-taking in 2015 and at the beginning of 2016. The first experimental study of the photon polarisation presented in this thesis is conducted using $B_s^0 \rightarrow \phi\gamma$ decays at LHCb. A detailed description of the extraction of the photon polarisation information from the collected LHCb data sample is documented in Chapter 4. Chapter 5 and Chapter 6 contain a detailed description of the studies of $B^+ \rightarrow \phi K^+ \gamma$ decays. In Chapter 5, the signal candidates are reconstructed using calorimetric photons whilst in Chapter 6, converted photons are used. The strategies of separating the merged π^0 background from the signal are discussed in these two chapters. The measurement of the $B^+ \rightarrow \phi K^+ \gamma$ CP asymmetry with a much improved precision with respect to the previous measurements is reported in Chapter 5. An attempt to probe the photon polarisation in the angular distributions in the $B^+ \rightarrow \phi K^+ \gamma$ decay is discussed in Chapter 5. Finally, a discussion on the results and on future prospects is given in Chapter 7.

1 Photon polarisation in radiative B decays

The quark level transition $b \rightarrow s\gamma$ is generated by the FCNC process, which is therefore not allowed at the tree level in the SM and must occur through a loop level diagram. Inside of the loop, heavy particles can propagate: top quarks in the case of SM or as yet unknown particles introduced by given models beyond the SM. Therefore, the $b \rightarrow s\gamma$ process can be used to indirectly probe such heavy particles.

Measurements of the CP asymmetries of $b \rightarrow s\gamma$ decays provide a sensitive probe to look for physics beyond the SM. A $b \rightarrow s\gamma$ transition mediated by non-SM particles could affect the CP asymmetry of these decays, because the virtual particles responsible for mediating the decay could have different current structures.

1.1 Radiative B decays via $b \rightarrow s\gamma$ transitions

The dominant effective Hamiltonian relevant for decays via $b \rightarrow s\gamma$ transitions in the SM (detailed in Ref. [21]) can be written as

$$H_{\text{eff}} = -\frac{4G_F}{\sqrt{2}} V_{tb} V_{ts}^* \left(\sum_{i=1}^8 \mathcal{C}_i(\mu) \mathcal{O}_i(\mu) + \sum_{i=7}^8 \mathcal{C}'_i(\mu) \mathcal{O}'_i(\mu) \right), \quad (1.1)$$

where the operators \mathcal{O}_{1-6} are the SM four-quark operators, $\mathcal{O}_7^{(\prime)}$ is the electromagnetic dipole operator, and $\mathcal{O}_8^{(\prime)}$ is the chromomagnetic dipole operator. The Wilson coefficients \mathcal{C}_7 and \mathcal{C}'_7 correspond to the amplitudes for emission of left- and right-handed photons in $b_R \rightarrow s_L \gamma_L$ and $b_L \rightarrow s_R \gamma_R$ decays, respectively. The dipole operator $\mathcal{O}_7^{(\prime)}$ is the dominant contribution and given by

$$\begin{aligned} \mathcal{O}_7 &= \frac{e}{16\pi^2} m_b [\bar{s}_L \sigma_{\mu\nu} (\frac{1+\gamma_5}{2}) b_R F^{\mu\nu}], \\ \mathcal{O}'_7 &= \frac{e}{16\pi^2} m_b [\bar{s}_R \sigma_{\mu\nu} (\frac{1-\gamma_5}{2}) b_L F^{\mu\nu}]. \end{aligned} \quad (1.2)$$

Chapter 1. Photon polarisation in radiative B decays

In the SM, $\mathcal{C}'_7/\mathcal{C}_7$ is proportional to the mass ratio m_s/m_b because only left-handed components of external fermions couple to W -boson in the SM. Since $m_s/m_b \approx 0.02$, the photon in $b \rightarrow s\gamma$ transitions in the SM is known to be predominantly left-handed. The exact level of suppression is mode dependent when QCD effects are considered.

Here only the dipole type effective Hamiltonian part in Eq. 1.1 [19, 20] is considered

$$H_{\text{eff}} = -\sqrt{8}G_F \frac{em_b}{16\pi^2} \left[F_L^s (\bar{s}_L \sigma_{\mu\nu} \frac{1+\gamma_5}{2} b_R) + F_R^s (\bar{s}_R \sigma_{\mu\nu} \frac{1-\gamma_5}{2} b_L) \right] F^{\mu\nu} + h.c., \quad (1.3)$$

where $F_{L(R)}^s$ corresponds to the amplitude for the emission of left(right)-handed photons in the $b_{R(L)} \rightarrow s_{L(R)} \gamma_{L(R)}$ decay. The $F_{L(R)}^s$ has a CKM phase given by the phase of $V_{tb} V_{ts}^*$. By defining a parameter ψ , the F_L^s and F_R^s can be related through

$$F_L^s = F^s e^{i\phi_L^s} \cos\psi, \quad F_R^s = F^s e^{i\phi_R^s} \sin\psi, \quad (1.4)$$

where ϕ_L^s and ϕ_R^s are CP violating phases. The parameter ψ is the fraction of “wrongly”-polarised photons, $\tan\psi \simeq \mathcal{C}'_7/\mathcal{C}_7$.

In radiative decays of the form $B \rightarrow f_s \gamma$, where f_s is either a single meson or a multiparticle state, we can denote their helicity amplitudes as follows

$$\begin{aligned} \bar{M}_L &= \mathcal{M}(\bar{B} \rightarrow \bar{f}_s \gamma_L), \\ \bar{M}_R &= \mathcal{M}(\bar{B} \rightarrow \bar{f}_s \gamma_R), \\ M_R &= \mathcal{M}(B \rightarrow f_s \gamma_R), \\ M_L &= \mathcal{M}(B \rightarrow f_s \gamma_L). \end{aligned} \quad (1.5)$$

The strong interaction is symmetric under parity and charge conjugation which allows to isolate the polarisation of the photon in the short distance $b \rightarrow s\gamma$ process from the subsequent long distance hadronisation to the final state. The total decay amplitude $M_{L(R)}$ can then be defined as a convolution of weak radiative amplitude $F_{L(R)}^s$ and strong polarisation amplitude $G_{L(R)}^s$ for the consequent decay of the left(right)-polarised f_s into the final state, including all necessary form-factors and Breit-Wigner forms.

Considering the f_s as a resonance with the fixed quantum numbers, the photon polarisation parameter λ_γ [22] can be defined as

$$\lambda_\gamma = \frac{|F_R^s|^2 - |F_L^s|^2}{|F_R^s|^2 + |F_L^s|^2}, \quad (1.6)$$

and the SM implies $\lambda_\gamma \simeq -1(+1)$ for radiative \bar{B} (B) decays. The amplitudes corresponding to emission of left-handed and right-handed photons do not interfere since they correspond to different final state and the photon helicity can be measured independently. Summing decay rates for the left-handed and right-handed photon helicity states over the decay final states,

the partial decay width takes the following form:

$$\begin{aligned}\frac{d\Gamma}{d\Omega} &\propto |F_L^s G_L^s|^2 + |F_R^s G_R^s|^2, \\ &\propto |G_R^s|^2 + |G_L^s|^2 + \lambda_\gamma (|G_R^s|^2 - |G_L^s|^2),\end{aligned}\tag{1.7}$$

where $d\Omega$ is the phase space of the final state particles. If one can extract the angular part from the branching ratio, the λ_γ can be measured.

1.2 Determination of the photon polarisation

The branching fractions of inclusive and exclusive $b \rightarrow s\gamma$ decays are proportional at leading order to $|\mathcal{C}_7|^2 + |\mathcal{C}_7'|^2$. It is not practical to determine the handedness of the emitted photon with large theoretical uncertainties in the hadronisation processes.

The direct determination of the photon polarisation, proposed by Gronau *et al.* [23, 24], is based on the study of the angular distribution of the three-body final state, $K\pi\pi$, coming from the axial vector $K_1(1^+)$ meson decay, in $B \rightarrow K_1(K\pi\pi)\gamma$. The LHCb experiment succeeded in observing a nonzero polarisation of the photons for the first time in $B^+ \rightarrow K^+\pi^+\pi^-\gamma$ decays¹ [25] by measuring up-down asymmetries that include both the angular dependence and the dependence on the invariant mass of the $K^+\pi^+\pi^-$ -system. To determine the photon polarisation from these asymmetries, detailed knowledge of the strong interactions in the different intermediate states in the $K^+\pi^+\pi^-$ -system is required.

The photon polarisation can also be directly measured in baryon decays such as in $\Lambda_b^0 \rightarrow \Lambda(pK)\gamma$ [26, 27]. The helicity of the emitted photon can be extracted from the angular part of the differential $\Lambda_b^0 \rightarrow \Lambda\gamma$ decay rate. This could be one of the promising ways to determine the photon polarisation at LHCb during Run II.

The photon polarisation can be indirectly determined from the measurement of the time-dependent mixing-induced CP -asymmetry in the radiative neutral B -meson decays $B \rightarrow f^{CP}\gamma$ [19, 20], where f^{CP} is a CP eigenstate. Time-dependent analyses of radiative b -hadron decays such as $B^0 \rightarrow K_s^0\pi^0\gamma$ have been performed by both the Belle and BaBar collaborations to probe the polarisation of the photon [28], where a large SM phase is suppressed due to the left-handedness of the photon. The pollution from SM backgrounds to the observables can play an essential role in the interpretation of new physics signals since the new physics is not required to carry a CP violation phase [29]. Compared to $B^0 \rightarrow K_s^0\pi^0\gamma$ decays, there is only a small SM phase in $B_s^0 \rightarrow \phi\gamma$ and $B^+ \rightarrow \phi K^+\gamma$ decays discussed in this thesis and it is further helicity suppressed. For new physics to be detected in the observables in these decays, the new physics is required to not only possess a different current structure to the SM but also a new CP violation phase.

¹Charge conjugation implied through out this thesis if not otherwise stated explicitly.

Another indirect method is to study the right-handed current based on the angular analysis in the semileptonic $B^0 \rightarrow K^{*0} e^+ e^-$ decay. In the low q^2 region, some theoretical uncertainties from long distance contributions are greatly reduced [30, 31]. The contribution from a virtual photon coupling to the lepton pair allows to measure the helicity of the photon in $b \rightarrow s\gamma$ transitions [32, 33]. The transverse asymmetries A_T^{Im} and $A_T^{(2)}$, that are sensitive to the polarisation of the virtual photon, were measured at LHCb by performing an angular analysis in $B^0 \rightarrow K^{*0} e^+ e^-$ decays at low q^2 [34]. The results are consistent with SM predictions.

These methods provide complementary information for the photon polarisation measurement. A combination of different methods [21] can in principle put a strong constraint on the short-distance \mathcal{C}_7 and \mathcal{C}_7' coefficients.

1.3 Mixing-induced CP asymmetries in $B_s^0 \rightarrow \phi\gamma$ decays

New physics can generate Lorentz structures such that \bar{B}_s^0 (B_s^0) decays with left-handed (right-handed) photons, and thus the two processes, where initial B_s^0 remains as B_s^0 and decays like $B_s^0 \rightarrow f_s^{CP} \gamma$ and initial B_s^0 first oscillates to \bar{B}_s^0 then decays like $\bar{B}_s^0 \rightarrow f_s^{CP} \gamma$, can interfere. The interference term can be studied using the time dependent decay rates of initial B_s^0 and \bar{B}_s^0 decaying into $f_s^{CP} \gamma$. The LHCb experiment is a good platform to study the B_s^0 system with high statistical precision because of its large production rate of B_s^0 mesons. The study of the time evolution of $B_s^0 \rightarrow \phi\gamma$ decays where ϕ has $J^{PC} = 1^{--}$ and decays immediately into $K^+ K^-$, offers the opportunity to test the $V - A$ structure of the SM [35].

The time-dependent decay rate for initial B_s^0 and \bar{B}_s^0 decaying into $\phi\gamma$ can be conventionally parametrised as follows [12, 35]

$$\begin{aligned}\Gamma_{B_s^0 \rightarrow \phi\gamma} &\propto |A|^2 e^{-\Gamma_s t} \left(\cosh \frac{\Delta\Gamma_s t}{2} - A^\Delta \sinh \frac{\Delta\Gamma_s t}{2} + C \cos \Delta m_s t - S \sin \Delta m_s t \right), \\ \Gamma_{\bar{B}_s^0 \rightarrow \phi\gamma} &\propto |A|^2 e^{-\Gamma_s t} \left(\cosh \frac{\Delta\Gamma_s t}{2} - A^\Delta \sinh \frac{\Delta\Gamma_s t}{2} - C \cos \Delta m_s t + S \sin \Delta m_s t \right),\end{aligned}\tag{1.8}$$

respectively, where

$$C = \frac{1 - |\lambda_f|^2}{1 + |\lambda_f|^2}, \quad S \approx \sin 2\psi \sin \varphi_s, \quad A^\Delta \approx \sin 2\psi \cos \varphi_s,\tag{1.9}$$

with λ_f defined as $\lambda_f \equiv \frac{q}{p} \frac{\bar{A}_f}{A_f}$ for decays with common final state, where A_f and \bar{A}_f are the amplitudes for B_s^0 and \bar{B}_s^0 to decay to the final state $\phi\gamma$, respectively. The phase ϕ_s involved in the B_s^0 - \bar{B}_s^0 mixing process can be written as $\frac{q}{p} = \left| \frac{q}{p} \right| e^{-i\phi_s}$. The phase φ_s is the phase difference between ϕ_s and CP violating phases $\phi_R^s + \phi_L^s$.

The SM prediction of ϕ_s is $-0.0363_{-0.0015}^{+0.0016}$ rad and is measured by the LHCb experiment to be -0.010 ± 0.039 rad [36, 37, 38]. The CP violating parameter $1 - \left| \frac{q}{p} \right|^2$ is expected to be $\lesssim \mathcal{O}(10^{-4})$ [39], thus $C \approx 0$ in SM is a good approximation for this decay. In the case of B_s^0

decays from $b \rightarrow s\gamma$, the weak phases satisfy $\phi_L^s = \phi_R^s \approx 0$ [19, 20, 35]. Therefore, the time-dependent CP -violating asymmetry parameter S of Eq. 1.9 is suppressed. On the other hand, the parameter $\Delta\Gamma_s$ is measured to be $0.083 \pm 0.006 \text{ ps}^{-1}$ [28] which gives a good prospect of measuring A^Δ through the $\sinh \frac{\Delta\Gamma_s t}{2}$ term. The parameter A^Δ is related to the ratio of right-over left-handed photon polarisation amplitudes in $b \rightarrow s\gamma$ transitions through parameter ψ .

The SM prediction on the photon polarisation sensitive parameter A^Δ is $0.047 \pm 0.025 + 0.015$ [35]. As seen from Eq. 1.8, a measurement of A^Δ does not require the initial flavour tagging and the sum of the B_s^0 and \bar{B}_s^0 samples can be used for this measurement.

1.4 CP violation in $B^+ \rightarrow \phi K^+ \gamma$ decays

The same technique proposed to measure the photon polarisation in $B \rightarrow K\pi\pi\gamma$ decays can be used for $B \rightarrow \phi K\gamma$ decays, as discussed in Ref. [22, 29]. If the hadron system f_s from the radiative B decay $B \rightarrow f_s\gamma$ can be characterised by a total angular momentum $J \geq 1$ and its z component m in the f_s rest frame, with the z -axis in the opposite direction of the photon, the angular distribution of the final state particles can be used to probe the photon polarisation. The resonance state f_s decay strongly into a pseudoscalar P_3 and a vector V :

$$f_s(J^P, m) \rightarrow VP_3, \quad \text{and} \quad V \rightarrow P_1P_2, \quad (1.10)$$

where \vec{l} is the relative orbital momentum between V and P_3 and the vector V has the spin s , helicity λ and momentum p . For each p , if the vector meson V has a nonzero mass, there are $2s + 1$ helicity states: $\lambda = -s, \dots, s - 1, s$. The partial wave amplitude in the helicity basis can be written as

$$A_{lm} \approx \sum_{\lambda} (l, 0, s, \lambda | J, \lambda) \bar{A}_{\lambda m} \quad (1.11)$$

where $(l, 0, s, \lambda | J, \lambda)$ are Clebsch-Gordan coefficients. In the case of $l \neq 0$, the interference pattern $|G_R^q|^2 - |G_L^q|^2 \approx \vec{p}_\gamma \cdot (\vec{p}_1 \times \vec{p}_2)$ which changes sign under the parity transformation starts to show up. This parity-odd triple correlation, resulting from the interference between left and right helicity amplitudes and leading to direct CP asymmetries, is a particularly powerful null test in $b \rightarrow s$ transitions.

Theoretical studies [22, 29] assume that the ϕK -system as a resonance with spin-parity J^P , in order to extract the photon polarisation parameter λ_γ from the angular distributions of the hadronic final states. The study of the possible contributions from kaonic resonances to ϕK performed by the Belle collaboration [40] shows that most of the events populate the low ϕK mass region but their small data sample precludes any definite conclusion. With the higher statistics of LHCb data sample, there is an opportunity to carry out a more detailed study of this system. To extract information on the photon polarisation pattern experimentally relies on strong interference between the partial waves in the ϕK -system with the latter being in the vector state [22]. The confirmation of the existence of such interferences is a crucial step to

Chapter 1. Photon polarisation in radiative B decays

measure the photon polarisation in this decay.

2 The LHCb experiment

The Large Hadron Collider (LHC) is a 27 km long circular accelerator built in an underground tunnel across the border of France and Switzerland, hosted by the European Organisation for Nuclear Research (CERN). In the LHC, two proton beams are accelerated in opposite directions and collide at four points where the beams cross each other. The LHCb experiment is one of the four main experiments (ALICE, ATLAS, CMS and LHCb) located at the LHC. It is designed to study properties of B and D mesons, with emphasis on precision measurements of CP violating processes and rare decays.

The integrated luminosity collected by the LHCb experiment is shown in Fig. 2.1. A full data set of about 3 fb^{-1} was collected with the LHCb detector during Run I in 2011 and 2012 at the centre-of-mass energies $\sqrt{s} = 7 \text{ TeV}$ and $\sqrt{s} = 8 \text{ TeV}$, respectively. The main physics results in this thesis are obtained from this data sample. After a shutdown period from the end of 2012 to summer 2015, the long shutdown 1 (LS1), the LHC restarted the Run II with pp collisions at an energy of 13 TeV.

2.1 The LHCb detector

The LHCb detector [41, 42] shown in Fig. 2.2 is a single-arm forward spectrometer covering the pseudorapidity (η) range $2 < \eta < 5$ as the $b\bar{b}$ pairs of interest in the experiment are emitted mostly either in forward or backward direction. A right-handed coordinate system is adopted in which the x -axis is horizontal and points towards the outside of the LHC ring, the positive z -axis points from the interaction point into the experiment following the LHC beam and the y -axis is perpendicular to the x - and z -axes. The region of the detector at positive (negative) z -axis is known as the forward (backward) or downstream (upstream) end. The LHCb detector systems are described in the following sections, organised according to the main purpose of the subdetectors.

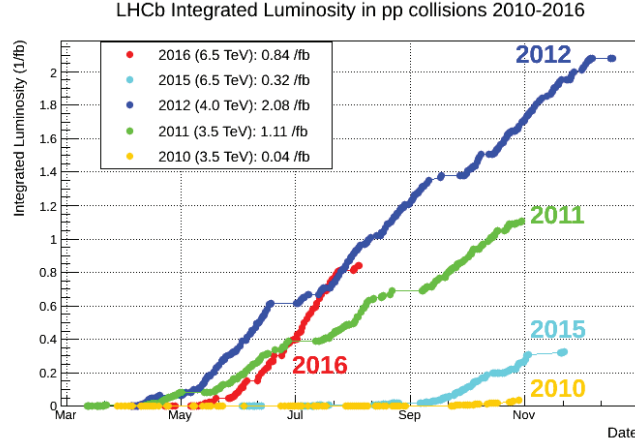


Figure 2.1: Integrated luminosity collected by the LHCb experiment split by year of data-taking.

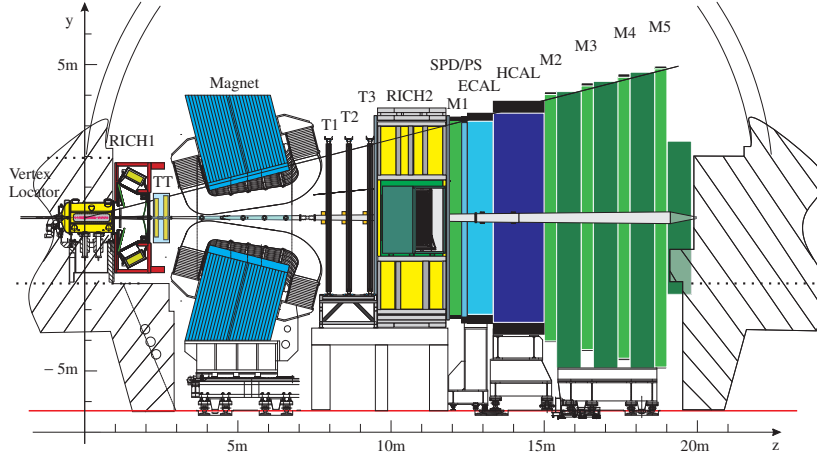


Figure 2.2: Side view of the LHCb detector. The vertex locator (VELO) surrounds the interaction point and together with the dipole magnet and the tracking stations (TT and T1, T2, T3) form the LHCb tracking system. The two RICH detectors RICH1 and RICH2 provide the particle identification. The calorimeter system includes a scintillating pad detector (SPD), a preshower detector (PS), an electromagnetic and a hadronic calorimeter (ECAL and HCAL). The muon system includes five muon stations (M1– M5).

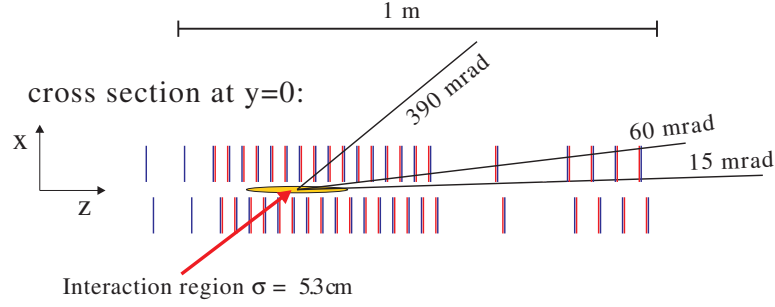


Figure 2.3: Top view of the placement of VELO modules.

2.1.1 Tracking system

The tracking system of the detector consists of a silicon-strip vertex locator (VELO) surrounding the pp interaction region, a large-area silicon-strip detector (TT) located upstream of a dipole magnet, and three stations (T1, T2 and T3) with a combination of silicon-strip detectors in the inner region (IT) and straw tubes in the outer region (OT), placed downstream of the magnet. The dipole magnet [41, 43], with a bending power of about $\int \vec{B} \cdot d\vec{l} = 4.2 \text{ Tm}$, permits access to the momentum of charged particles by measuring their deflection in its field.

The VELO [41, 42, 44, 45] is a silicon microstrip detector designed to identify primary and secondary vertices with good precision. The high spatial resolution of the VELO enables a precise determination of the particle's flight direction close to the primary interaction point, resulting in a good vertex resolution and a good lifetime resolution for b -hadron lifetime measurements. A sketch of the placement of the VELO modules is shown in Fig. 2.3. There are 21 stations with pairs of half-disc shaped sensors mounted back-to-back positioned on the left and right of the beam. Each pair contains one r -sensor and one ϕ -sensor to provide a measurement in r - ϕ coordinate: the r -sensor measures the radial coordinate with circular-shaped strips, subdivided into four 45° regions; the ϕ -sensor have strips in approximately radial direction and subdivided into inner and outer regions, to readout the orthogonal coordinate to the r -sensor. Two additional stations in the backward direction forming the pile-up¹ system with a single r -sensor each. The pile-up system is used in the hardware trigger to veto events with multiple interactions and provide tracks in the backward direction to improve the spatial resolution of reconstructed vertices. The silicon sensors are very close to the beam during the detector operation, about 8 mm from the beam to the edge of the sensitive area of the silicon. The beam vacuum is only separated from the sensors by a thin aluminium foil which shields the sensors from RF pickup from the beam. To avoid beam induced damage in the sensors during beam set-up or beam dump, the sensors can be retracted away from the beam to safe positions, as shown in Fig. 2.4.

The IT and TT [41, 42, 46, 47] together are called the silicon tracker (ST) due to the use of the same silicon-strip technology. Silicon strips offer good hit resolution and fast response time,

¹The average number of pp interactions in visible events.

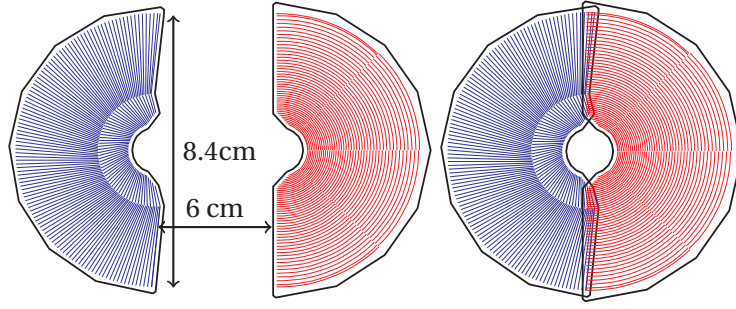


Figure 2.4: VELO in open/closed state.

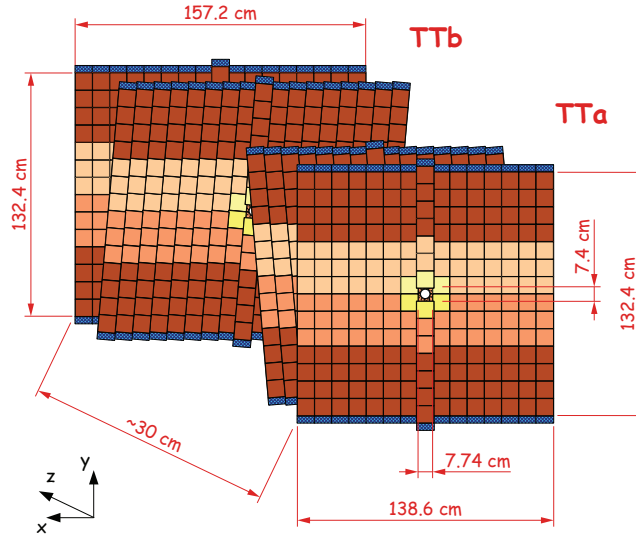


Figure 2.5: Schematic view of the TT where readout electronics are indicated in blue.

which are needed to operate in regions of high track density and radiation. The TT consists of two stations separated by about 27 cm along z direction, with two layers of silicon-strip sensors in each station. The four layers are arranged in an x - u - v - x configuration, as shown in Fig. 2.5. The x -layers have their measurement direction along the x -axis and the strips parallel to the y -axis, whilst the u (v) layer is rotated by a stereo angle of -5° ($+5^\circ$) around the z -axis (The stereo angle is defined to be positive for a counter-clockwise rotation.). This arrangement allows coordinates to be determined in three dimensions.

The IT covers the area with the highest track density of the tracking stations downstream of the dipole magnet. Each IT station consists of four detector boxes and depending on their position with respect to the beam pipe, the boxes are named “Top Box”, “Bottom Box”, “ASide Box” and “CSide Box” (Fig. 2.6). Each box contains four layers of silicon sensors arranged in an x - u - v - x configuration with the same stereo angles as used for TT. The silicon ladders consist

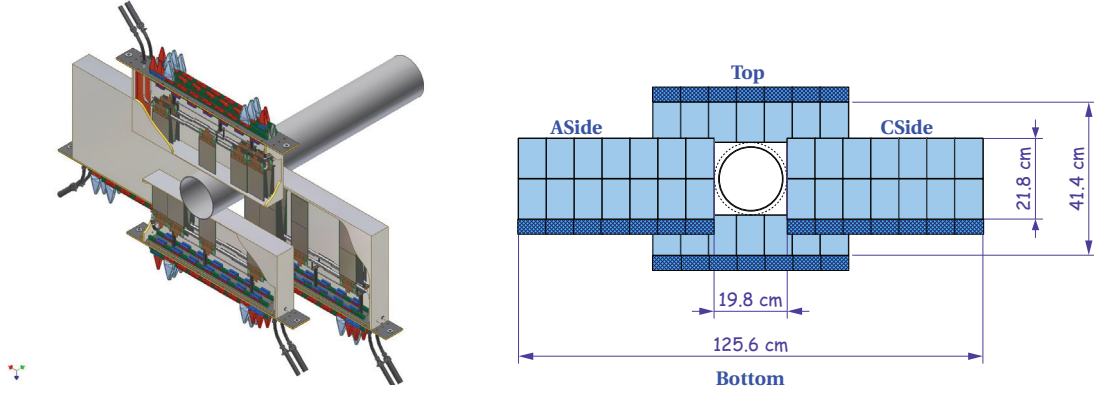


Figure 2.6: Schematic view of the IT boxes (left) and the geometry of an IT layer (right).

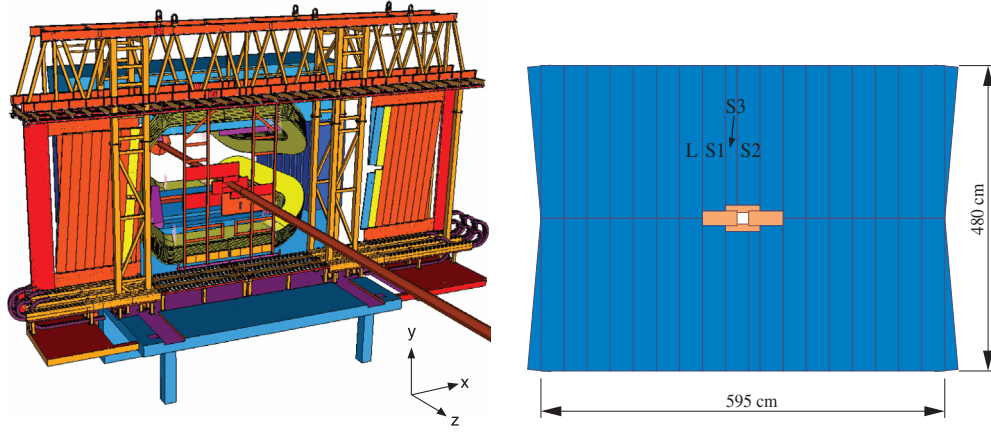


Figure 2.7: An isometric view of the first OT station (left) and its front view (right).

of one or two silicon sensors are mounted on a common cooling plate where the alignment holes on the plate are used to precisely position the ladders. Adjacent ladders overlap by a few millimetres in order to ensure full acceptance coverage and facilitate the relative alignment of the ladders using hits from shared tracks. The strip pitch is about $183\ \mu\text{m}$ for TT and $198\ \mu\text{m}$ for IT, which leads to a spatial resolution of the order of $50\ \mu\text{m}$.

The OT [41, 42, 48, 49] covers the LHCb acceptance that is not covered by the IT. It is a gas detector operating with a mixture of $\text{Ar}/\text{CO}_2/\text{O}_2$ (70% : 28.5% : 1.5% per volume) with a set-up similar to IT with three stations and four layers each station. Each individual layer is composed of a left and a right half, each containing nine modules as shown in Fig. 2.7. Modules of two successive half-layers are mounted in a “C-Frame”, which can be retracted from its position next to the beam pipe to do maintenance work. Each module contains two staggered monolayers of drift tubes with a diameter of 5 mm to allow a drift time of less than 50 ns and a sufficient drift-coordinate resolution of $200\ \mu\text{m}$.

Trajectories of charged particles traversing the tracking system are reconstructed from hits in the VELO, TT and the T stations (T1, T2 and T3). Depending on their paths through the

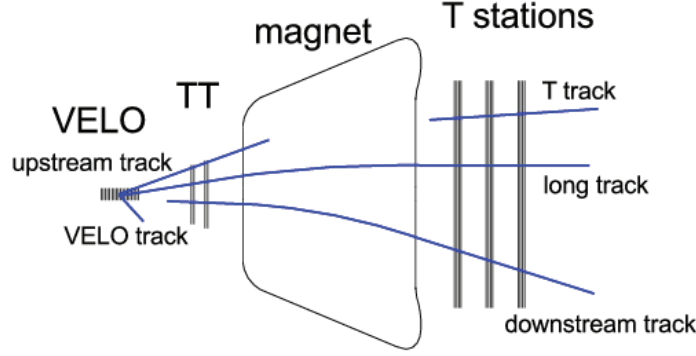


Figure 2.8: A schematic illustration of the defined track types: long, upstream, downstream, VELO and T tracks.

spectrometer, the following track types [42, 50, 51] are defined, as illustrated in Fig. 2.8:

- VELO tracks use measurements in the VELO only and are typically large-angle or backward tracks that are used for primary vertex reconstruction and long track searches.
- T tracks are tracks with measurements in the T stations. The T tracks can be used for long track reconstruction. If the T tracks only pass through the T stations, they are typically produced by secondary interactions but are useful for the studies of the RICH2 data.
- Long tracks traverse the full tracking system. They have hits in both the VELO and the T stations, and optionally in the TT. Long tracks offer the most precise momentum estimate.
- Upstream tracks are tracks with hits in the VELO and TT stations only. In general their momentum is too low to traverse the magnet and reach the T stations. They can be used for background studies for RICH1 if sufficient Cherenkov photons are generated.
- Downstream tracks are tracks with hits in the TT and T stations only. They are important for the reconstruction of long lived particles that decay outside the VELO acceptance.

Long tracks are the most important set of tracks for physics analysis. Searching for a long track starts either with determination of a trajectory by combining the VELO tracks with measurements in T stations to which further hits in the T stations are progressively added, or by combining VELO track segments with T station ones. Finally, hits in the TT consistent with the extrapolated trajectories of each track are added to improve their momentum determination. The momentum resolution $\delta p/p$ is about 0.5% at low momentum, rising to about 1.0% at 200 GeV/c.

Downstream tracks are important to reconstruct long-lived particles like K_S^0 and Λ which often do not decay before they leave the VELO, and converted photons occurred outside the VELO. Downstream tracks are found starting with T tracks, extrapolating them through the magnetic field and searching for the potential TT hits belonging to the tracks.

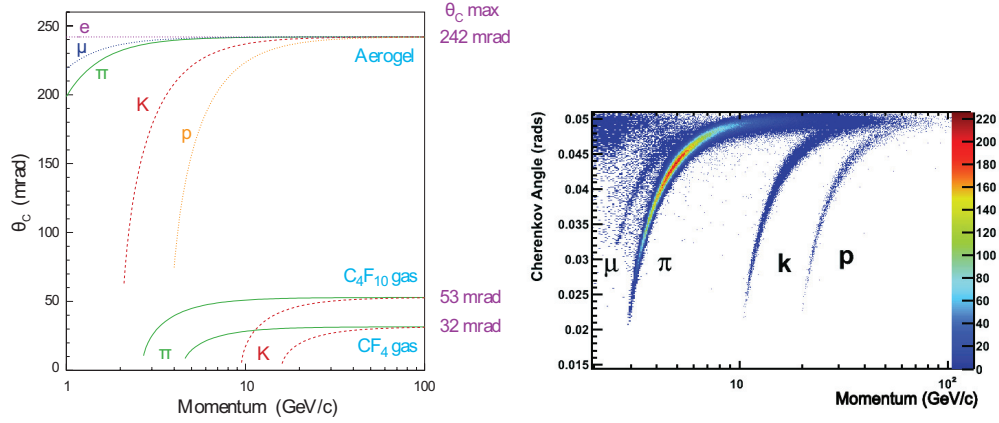


Figure 2.9: Cherenkov angle versus particle momentum for the RICH radiators (left) and the reconstructed Cherenkov angle as a function of track momentum in the C_4F_{10} radiator (right).

2.1.2 Particle identification of charged hadrons

Cherenkov detectors can identify particles of different masses, if their momenta are known, based on the properties of Cherenkov light. When charged particles traverse a medium at a velocity $\beta = v/c$ larger than the velocity of light in that medium, Cherenkov light is emitted along their trajectories. The photons are emitted in a cone with an opening angle θ_C given by $\cos\theta_C = \frac{1}{n\beta}$ around the particle trajectory, where n is the refractive index of the material. From the radius of the rings, it is possible to infer θ_C and thus mass of the particle, if its momentum is known from the tracking. Charged hadrons of pions, kaons and protons are identified using two ring-imaging Cherenkov (RICH) detectors [41, 42, 52, 53] that cover different momentum ranges.

RICH1 is designed to provide particle identification for low-momentum particles, placed between the VELO and the TT. It contains two radiators with 5 cm of silica aerogel ($n = 1.03$) as the first radiator and 85 cm of C_4F_{10} ($n = 1.0014$) as the second radiator, covering a momentum range up to 10 GeV/c and from 10 GeV/c to 60 GeV/c, respectively. Emitted photons are detected with Hybrid Photon Detectors (HPDs) which record an image of the resulting rings of Cherenkov light formed by the mirrors. A second Ring Imaging Cherenkov Counter (RICH2) provides particle identification for high momentum charged particles up to 100 GeV/c.

The RICH2 is situated between the T3 and the calorimeter system. It uses CF_4 gas with a refractive index of $n = 1.0005$. The usable momentum range starts around 15 GeV/c and extends well above 100 GeV/c.

The dependence of the Cherenkov angle on the particle momentum for different RICH radiators and the reconstructed Cherenkov angle in the C_4F_{10} radiator in RICH1 are shown in Fig. 2.9. The acceptance of RICH1 is from 25 mrad to 300 mrad in the x direction and from 25 mrad to 250 mrad in the y direction. For RICH2, the acceptances range between 25 mrad to 120 mrad in the x direction and up to 100 mrad in the y direction.

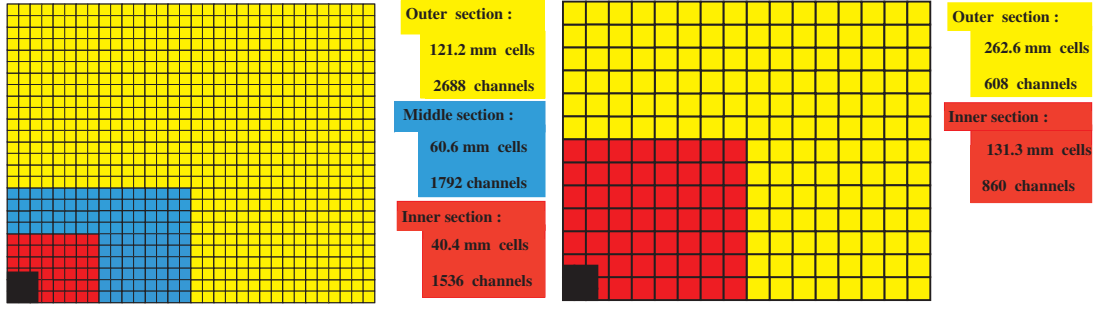


Figure 2.10: Layout of SPD/PS/ECAL (left) and HCAL (right).

2.1.3 The calorimeter system

The calorimeter system [41, 42, 54, 55] consists of scintillating-pad (SPD) and pre-shower (PS) detectors, an electromagnetic calorimeter (ECAL) and a hadronic calorimeter (HCAL). It is designed to identify photons, electrons and hadrons and measure their energies and positions, and also provide information for the hardware trigger. The SPD, PS, ECAL and HCAL are designed with higher granularity at the high density particle region near the beam pipe and lower granularity in the outward region as shown in Fig. 2.10, based on the dimensions of the electromagnetic showers for SPD/PS/ECAL and the hadronic showers for HCAL.

The SPD and PS are walls of scintillator pads with a wavelength shifting fibre (WLS) coil grooved inside for better light collection. A 1.5 cm lead converter with a 2.5 radiation lengths (X_0) is placed between the SPD and PS. The SPD delivers a single bit depending on whether the crossing particle is charged or neutral and completes the PS tagging of the electromagnetic shower.

The ECAL is made of a sampling scintillator/lead structure with a total thickness of $25X_0$ to ensure the full containment of high energy photon showers for optimal energy resolution. The HCAL is a sampling device made from iron and scintillating tiles as absorber and active material, respectively. The thickness of the HCAL is limited to 5.6 nuclear interaction lengths (λ_i) due to space constraints. The achievable energy resolution is $\frac{\sigma_E}{E} = \frac{10\%}{\sqrt{E}} \oplus 1\%$ for ECAL and $\frac{\sigma_E}{E} = \frac{80\%}{\sqrt{E}} \oplus 10\%$ for HCAL where the unit of the energy is in GeV.

Good reconstruction and identification of photons [42, 55, 56] is of crucial importance when performing the physics analyses presented in this thesis. To select neutral clusters with a high charged particle rejection efficiency, all reconstructed tracks in the event are extrapolated to the calorimeter reference plane to perform a matching with the reconstructed ECAL clusters. The energy of a photon is determined from the total cluster energy in the ECAL and the reconstructed energy deposited in the PS, and its direction is derived from an assumed origin for the photon at the primary vertex and the energy-weighted position of the cluster.

On average, 44% of the photons originating from the pp collisions are converted into electron-positron pairs when reaching the PS and half of the photon conversions occur before the

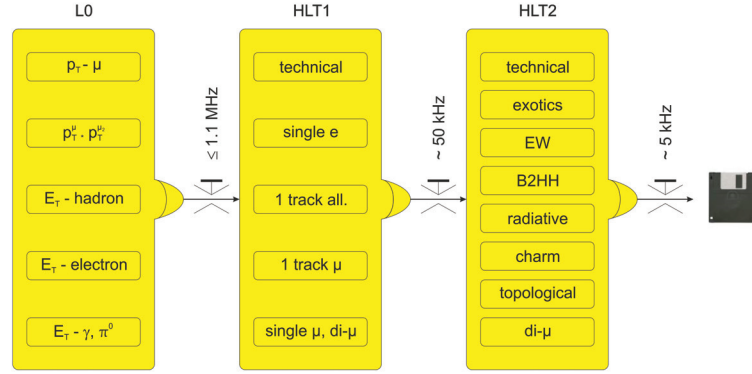


Figure 2.11: The schematic of the overall LHCb trigger scheme.

magnet. The photons converted before the magnet are reconstructed with dedicated software whilst the electron-positron pairs originated from photons converted after the magnet usually produce a single cluster in the ECAL and are identified by the SPD information on the charge of the incoming particle.

At higher energies, the distance between the two photons generated in the decay of neutral pions becomes of the order of the ECAL pad size and makes it impossible to distinguish π^0 s from real photon candidates, so they are reconstructed as a single neutral cluster. The separation between photons and this type of neutral pions (called merged π^0 s) is based on the shape of the cluster in the PS and ECAL.

2.1.4 The muon system

The muon system [41, 42, 57, 58, 59] consists of five stations M1, M2, M3, M4 and M5 for muon detection, identification and triggering. The M1 is in front of the SPD whilst the other four stations are behind the calorimeter system. Muon stations are composed of alternating layers of iron filter and multiwire proportional chambers (MWPCs) and only the innermost region uses triple-GEM detectors to cope with higher particle flux. Detailed information on the detector design and performance can be found in Refs. [41, 42, 57, 58, 59].

2.2 The LHCb trigger system

The trigger [41, 60, 61] as shown in Fig. 2.11 consists of a hardware stage (L0), based on information from the calorimeter and muon systems and the pile-up system located upstream of the VELO, followed by a software stage high level trigger (HLT) which uses the full event information. It is crucial in selecting amongst the collisions those of interest for c - and b -physics studies. The aim of the L0 trigger is to reduce the bunch crossing rate of 40 MHz down to 1 MHz, the maximum rate at which the detector can be read out, by selecting high

transverse energy (E_T) or high transverse momentum (p_T) particles. All the L0 accepted events are passed on to the HLT. The software stage trigger is divided into two steps HLT1 and HLT2. At HLT1, a partial event reconstruction is performed and a few tracks per stream are selected based on their transverse momentum and impact parameter (IP) with respect to the primary vertex. It is necessary to be able to quickly confirm or reject the L0 triggered events. The HLT2 performs a fast full event reconstruction, selecting either exclusive or inclusive decays by specific event topologies. The HLT uses reconstruction algorithms simplified comparing to the offline reconstruction to fulfil the timing requirement.

2.3 Event reconstruction and simulation framework

The LHCb software runs within the object-oriented GAUDI framework [62, 63]. Different GAUDI applications are responsible for different tasks such as event generation, detector simulation, event triggering and reconstruction, and physics analysis.

Simulated events are generated with GAUSS [64, 65]. In Monte Carlo (MC), pp collisions are simulated using PYTHIA [66, 67] with a specific LHCb configuration. Decays of hadronic particles are described by EVTGEN [68, 69], in which final state radiation is generated using the PHOTOS tool [70]. The interactions of generated particles with the detector material, the tracing of charged particles in the magnetic field and the decay of the remaining unstable particles are implemented using the GEANT4 toolkit [71]. The output of GAUSS is digitised into electrical signals using BOOLE [72] to simulate the response of the individual subdetector electronics in its sensitive area. The response simulation of the digitisation processes includes a physics process of signal collection and the specific behaviour of the electronics. Its calibration relies on the detector prototype R&D and testbeam data. The BOOLE output data has the same format as real data collected by the LHCb detector. The trigger, reconstruction and analysis of the simulated events are processed in the same way as on data using the same algorithms.

The L0 can be seen as part of the digitisation as it is fully implemented in electronics whilst the HLT triggers are executed on a dedicated processor farm and can be considered as part of the reconstruction. MOORE [73] runs the reconstruction for the software trigger in real time; this is known as the online reconstruction. The data selected by the trigger system are reconstructed offline using BRUNEL [74]. It reconstructs charged tracks by combining hits from the tracking system and links the particle identification information from the RICH detectors, calorimeter system and the muon system to the tracks. The analysis package DAVINCI [75] applies particle hypotheses to tracks and then combines them to form the decay chain of interest. MOORE shares most of the reconstruction and selection algorithms with BRUNEL and DAVINCI.

The LHCb detector description [62, 76] is used by all applications. It is designed to deal with all aspects of detector information, including geometry, materials, alignment, calibration and *etc.* The database which describes the detector information is written in Extensible Markup Language (XML) [77].

To reduce the storage of the reconstructed data further and provide easier access to data only relevant to decays of interest, a DAVINCI application called STRIPPING [78] is implemented to filter the data sample into different streams based on the topologies of the decay channels and the usage of the data sample. Each STRIPPING stream contains lines relevant to physics decays of interest. The principle of the STRIPPING is similar to the HLT trigger but with a full offline event reconstruction performed and looser timing constraints. All the physics analyses presented in this thesis are performed on the STRIPPING output.

3 The LHCb tracker alignment

The spatial alignment of the detector and the accurate calibration of its subcomponents are essential elements to achieve the best possible physics performance. As an illustration, the $\mu^+\mu^-$ invariant mass distributions of $\Upsilon \rightarrow \mu^+\mu^-$ decays are shown in Fig. 3.1, where a better alignment significantly improves the $\Upsilon(1S)$ mass resolution from $86\text{ MeV}/c^2$ to $44\text{ MeV}/c^2$. Track reconstruction relies on the known position of the tracking system. Misalignment of the tracking system leads to degradation of the momentum measurement and the flight distance and mass determination of the particles. The position of the LHCb subdetectors has to be better known than their intrinsic spatial resolutions stated in Ref. [46, 47, 48]. The TT, IT and OT are collectively referred to as the tracker in this chapter.

3.1 Tracker alignment in the vertical direction

A procedure to align the ST and OT for their positions in the vertical direction (*i.e.* the y -axis), based on a hit detection efficiency profile method, was developed in Ref. [80]. This method (hereafter named the “tracker vertical alignment”) uses the known positions of the insensitive

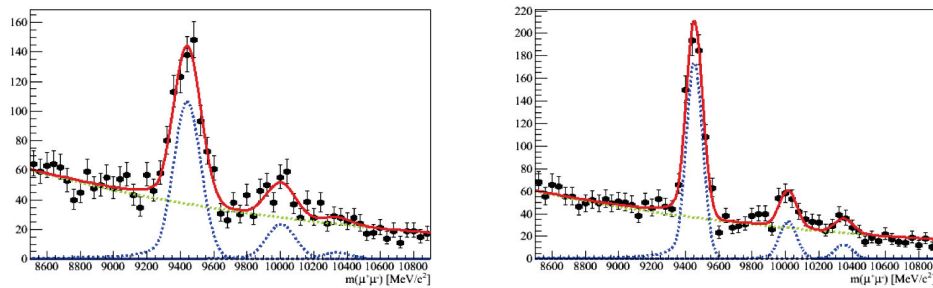


Figure 3.1: Invariant mass distributions for $\Upsilon(1S)$, $\Upsilon(2S)$ and $\Upsilon(3S)$ with preliminary 2010 alignment (left) and with the final 2012 alignment (right) during Run I. The mass resolution of the $\Upsilon(1S)$ is $86\text{ MeV}/c^2$ on the left plot and is $44\text{ MeV}/c^2$ on the right plot. Figures from Ref. [79].

Chapter 3. The LHCb tracker alignment

Table 3.1: Displacement in y -axis for IT boxes with respect to survey measurements before the 2015 data-taking.

IT Boxes	Bottom [mm]	Top [mm]	ASide [mm]	CSide [mm]
IT1	1.17 ± 0.06	0.49 ± 0.05	0.93 ± 0.03	1.47 ± 0.03
IT2	1.38 ± 0.08	0.20 ± 0.09	0.63 ± 0.05	0.91 ± 0.02
IT3	0.37 ± 0.09	0.92 ± 0.09	0.96 ± 0.05	1.10 ± 0.03

Table 3.2: Displacement in y -axis for IT boxes with respect to the 2015 database.

IT Boxes	Bottom [mm]	Top [mm]	ASide [mm]	CSide [mm]
IT1	0.03 ± 0.07	0.90 ± 0.05	0.26 ± 0.02	-0.18 ± 0.03
IT2	-0.09 ± 0.08	1.12 ± 0.08	-0.15 ± 0.03	0.55 ± 0.03
IT3	-0.16 ± 0.10	1.63 ± 0.09	-0.18 ± 0.04	-0.30 ± 0.03

regions of the detector and is based on the data collected without the spectrometer magnetic field. The hit efficiencies were obtained by extrapolating tracks reconstructed in the VELO by the FastVelo algorithm [81], to the tracker planes and searching for corresponding hits around the projected trajectory.

The measured displacements in y -axis for IT boxes with respect to survey measurements [82] before 2015 data-taking are summarised in Table 3.1 whilst the displacements with respect to the 2015 database before 2016 data-taking are listed in Table 3.2. The displacement in each sector is shown in Fig. 3.2 and Fig. 3.3 in 2015 and 2016, respectively. The corrections implemented in the database are the averages of all the sectors in each box. The trend of the misalignment is better shown in the Fig. 3.2 and Fig. 3.3.

The shift of Top y positions of IT1 and IT3 are visible in Fig. 3.3, whilst the CSide box which is mounted on the same frame as the Top box does not show any unexpected displacement. As seen in Fig. 2.6, Top boxes are mounted on the frames upside down compared to the other IT detector boxes. The vertical position displacement of the IT Top boxes implemented in the database during the 2015 data-taking period was mistakenly shifted in the opposite direction, which resulted in this unexpected displacement for Top boxes in 2016 data-taking especially for IT1 and IT3 since there are only displacement in Top boxes. The shift has been evaluated using $J/\psi \rightarrow \mu^+ \mu^-$ events in 2015 data for offline alignment and kinematics studies, and a simulated inclusive- b sample for the studies of tracking efficiencies. There is no obvious degradation in the measurement of the J/ψ mass and the properties of the tracks due to the mistake in the 2015 database for the IT Top boxes, and negligible effects on the tracking efficiency are observed. The same issue also applied to the IT2 Top boxes but the displacement in 2015 for IT2 was much smaller compared to IT1 and IT3. In addition, during the winter break of 2015, the Top box of the IT2 was moved up by about 1 mm, which is clearly shown in Fig. 3.3 and shifts are observed in both Top and CSide boxes.

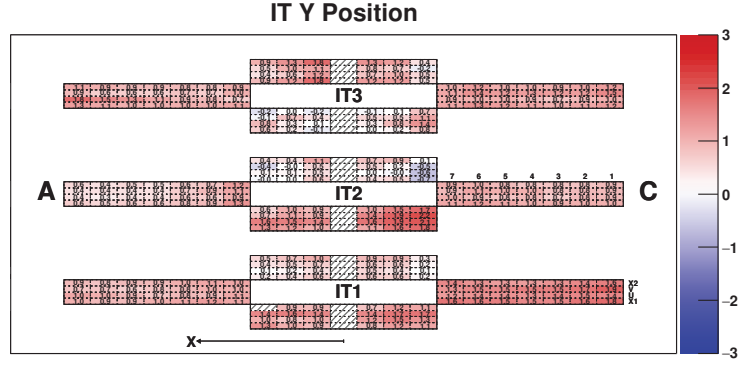


Figure 3.2: Displacement in y-axis for IT sectors with respect to the survey measurements in 2015 data. The shaded sectors are excluded from the vertical alignment procedure either because the sensors are excluded during the data-taking due to technical issues or because the efficiency profile in the sensor is too irregular to extract reliable information.

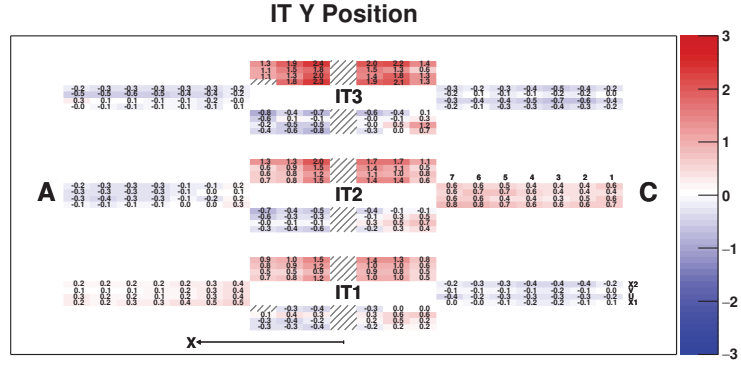


Figure 3.3: Displacement in y-axis for IT sectors with respect to the 2015 database. The shaded sectors are excluded from the vertical alignment procedure either because the sensors are excluded during the data-taking due to technical issues or because the efficiency profile in the sensor is too irregular to extract reliable information.

Chapter 3. The LHCb tracker alignment

The default tracker alignment procedure aligns the following degrees of freedom for each subdetector:

- IT boxes: translations in x - and z -axes (T_x and T_z) and rotation in z -axis (R_z);
- TT layers: translation in z -axis (T_z);
- TT modules: translation in x -axis (T_x);
- OT C-Frames: translation in x -axis (T_x);
- OT layers: translation in z -axis (T_z);
- OT modules: translation in x -axis (T_x).

A more complete alignment procedure which includes the translations and rotations of the following degrees of freedom for each subdetector is performed when a large misalignment is observed:

- IT boxes (T_x , T_z and R_z), layers (T_x and R_z) and ladders (T_x and R_z);
- TT layers (T_z) and modules (T_x and R_z);
- OT C-Frames (T_x and R_z), layers (T_z) and modules (T_x and R_z).

In Run II, based on the database with corrections from the tracker vertical alignment implemented, the default tracker alignment was performed first and a more complete alignment procedure follows afterwards. This full procedure is expected to be performed only once at the beginning of the data-taking. During data-taking, only the default tracker alignment is performed at the beginning of each fill ¹; the information on this procedure is detailed in Section 3.2.

The mean value of the unbiased residuals in each sector for 2016 data is shown in Fig. 3.4. The unbiased residual is calculated by removing the hit from the track fit and calculating the distance between the hit and the extrapolated track position. With a perfect detector alignment, the unbiased residual is expected to be centred at zero. The top plot in Fig. 3.4 shows the default tracker alignment and the complete alignment procedure performed whilst the bottom plot is in addition to the full procedure, the tracker vertical alignment is included. The alignment for the IT is clearly improved with the vertical alignment included in the full procedure.

3.2 Alignment and calibration framework

The LHCb trigger strategies for Run I and Run II data-taking are shown in Fig. 3.5. Compared to Run I, the LHC collides protons at an increased centre-of-mass energy of $\sqrt{s} = 13$ TeV and with 25 ns bunch spacing during Run II. The online event reconstruction in Run I was simpler and faster than that used in offline and did not have the latest alignment and calibration constants applied. In Run II, the selected events after the first stage of the software trigger are

¹A fill is one injection of the protons by the LHC. The fill duration is designed to be about 15 hours which follows an exponential decay distribution with average lifetime of a few hours.

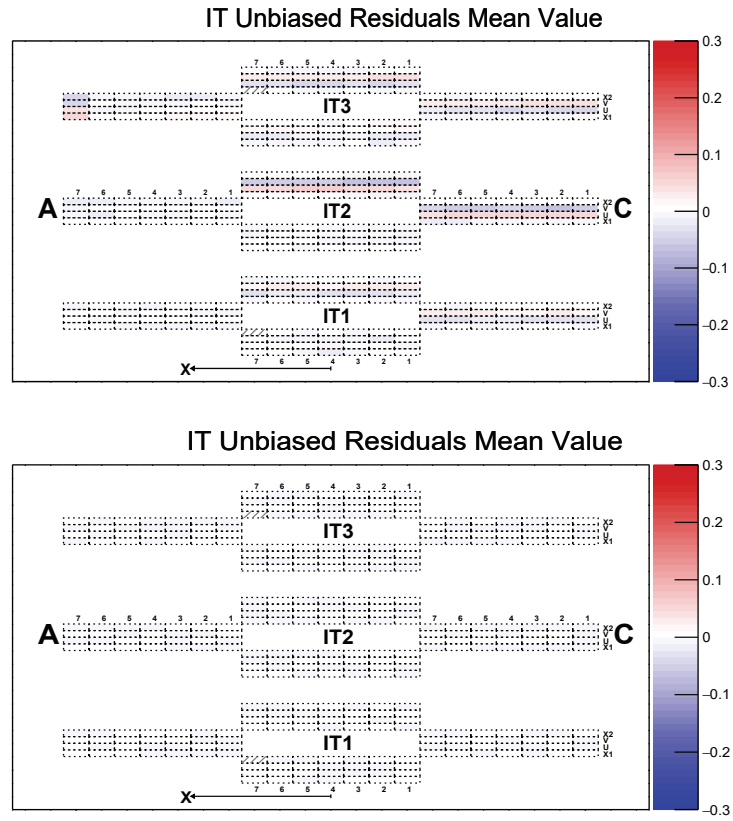


Figure 3.4: Mean values of the unbiased residuals of the tracks from the default procedure (top) and the full procedure (bottom) in 2016 data.

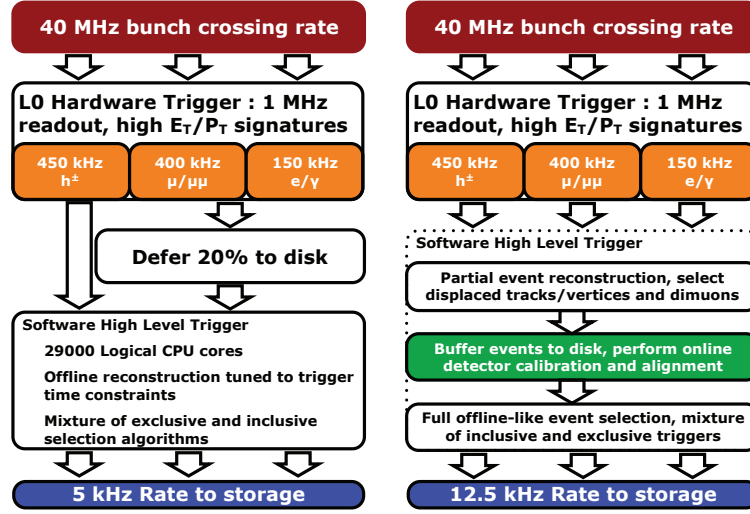


Figure 3.5: Schematic diagram of the LHCb trigger data-flow in Run I data-taking (left) compared to the data-flow in Run II (right). The selected events after L0 and HLT1 are buffered on disk while real-time alignment and calibration are performed during Run II.

buffered on local disks, and an automatic calibration and alignment is performed immediately. The alignment is evaluated using a dedicated event sample that is enriched of particle decays (e.g. $D^0 \rightarrow K^- \pi^+$, $J/\psi \rightarrow \mu^+ \mu^-$), and the calibration is run on several nodes of the farm used for the trigger within a few minutes. This online procedure enables the best possible calibration and alignment information to be used at the trigger level and, therefore, provides better event reconstruction performance in the trigger. It also minimises the differences between online and offline reconstruction performance, and allows some physics analyses to be done directly on the trigger output [83].

The alignment of the VELO, tracker and the muon system uses a Kalman filter and minimises the χ^2 calculated on residuals of reconstructed tracks [84, 85]. Multiple scattering and energy loss in the material together with magnetic field information are taken into account. The Kalman filter also allows mass and vertex constraints to be incorporated, and to align multiple sub-detectors at once.

A global alignment algorithm of the tracking system has been implemented in the LHCb software framework [85]. A track χ^2 is defined as

$$\chi^2 = [m - h(x, \alpha)]^T V^{-1} [m - h(x, \alpha)], \quad (3.1)$$

where m is a vector of measured coordinates, V is a covariance matrix, $h(x, \alpha)$ is the measurement model for a vector of track parameters x and a set of alignment parameters α . The parameters α are considered common to all tracks in data taken in the same condition. By minimising the sum of the χ^2 values of all the tracks simultaneously with respect to α and the

track parameters x_i of each track i ,

$$\frac{\partial \sum_i \chi_i^2}{\partial \alpha} = 0 \quad \text{and} \quad \forall_i \frac{\partial \chi_i^2}{\partial x_i} = 0, \quad (3.2)$$

we can estimate α . In practice, track parameters are estimated for an initial set of alignment parameters α_0 first and the total χ^2 is minimised subsequently with respect to α taking into account the dependence of x_i on α . Given an initial alignment parameter value α_0 , the solution for $\alpha = \alpha_0 + \Delta\alpha$ is obtained by solving a set of linear equations

$$\left. \frac{d^2 \chi^2}{d\alpha^2} \right|_{\alpha_0} \Delta\alpha = - \left. \frac{d\chi^2}{d\alpha} \right|_{\alpha_0}, \quad (3.3)$$

If the χ^2 for each track has been minimised with respect to the track parameters for the initial alignment parameter value α_0 , the first and second derivatives of the total χ^2 with respect to the alignment parameters can be obtained by summing the contributions from all the tracks:

$$\begin{aligned} \frac{d\chi^2}{d\alpha} &= 2 \sum_{\text{tracks } i} \frac{dr_i^T}{d\alpha} V_i^{-1} r_i, \\ \frac{d^2 \chi^2}{d\alpha^2} &= 2 \sum_{\text{tracks } i} \frac{dr_i^T}{d\alpha} V_i^{-1} R_i V_i^{-1} \frac{dr_i}{d\alpha}, \end{aligned} \quad (3.4)$$

where $r_i = m_i - h(x_i, \alpha)$ is the hit residual of the reconstructed track and R_i is the covariance matrix of the residuals after the track fit. Reconstructing tracks in a event and computing the χ^2 derivatives for these tracks can be done on a single node, independent of the other events. This step can then be parallelised by assign different events to different nodes and the χ^2 derivatives are summed over the events run on the same node. The partial sums of the events calculated on different nodes can then be added together and minimised on a single node. If the alignment is sufficiently constrained, the second derivative matrix can be inverted and the covariance matrix for the alignment parameters is given by

$$\text{Cov}(\alpha) = 2 \left(\frac{d^2 \chi^2}{d\alpha^2} \right)^{-1}. \quad (3.5)$$

The change in the total χ^2 as the result of a change $\Delta\alpha$ in the alignment parameters can be written as

$$\Delta\chi^2 = \frac{1}{2} \frac{d\chi^2}{d\alpha}^T \Delta\alpha = -\Delta\alpha^T \text{Cov}(\alpha)^{-1} \Delta\alpha, \quad (3.6)$$

by ignoring higher order derivatives in α . The change in the global χ^2 , $\Delta\chi^2$, is equivalent to the significance of the alignment correction. Therefore, the quantity $\Delta\chi^2$ is a useful measure for following the convergence of an alignment.

In the implementation of this procedure, to coordinate the different alignment and calibration activities, two kind of tasks are present: the analyser and the iterator. The analyser performs

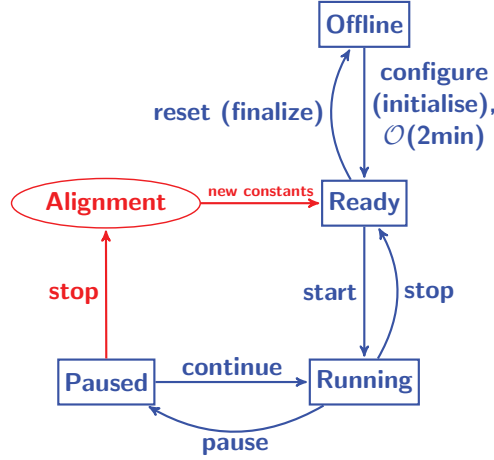


Figure 3.6: A finite state diagram defining the behaviour of the alignment tasks. Figure adapted from Ref. [86].

track reconstruction based on the alignment constants provided by the iterator and is parallelised on ~ 1700 nodes. A dedicated framework has been put in place to parallelise the alignment tasks on the multi-core farm infrastructure used for the trigger in order to meet the computing time constraints. The iterator collects the output of the analysers and minimises the χ^2 , computing the alignment constants that can be used for the next iteration.

The behaviour of both the analyser and the iterator for the detector alignment are determined by the finite state diagram in Fig. 3.6. After the initial configuration, a run controller issues a start to the analysers which read the initial alignment constants and run on the events assigned to them and then go to the paused state. When all the analysers are paused, the run controller issues them a stop during which the analysers write the partial sums that they computed on a fixed location of a shared file system and go back to the ready state. The run controller then starts the iterator to read the output of the analysers, combine them and compute a new set of alignment constants. A new iteration of the alignment procedure is issued by the run controller sending a start command to the analysers. The iterations continue until the difference of the $\Delta\chi^2$ between two successive iterations is smaller than a given value.

The automatic evaluation of changes in alignment constants computed to the previous values is performed at the beginning of each fill. A change of run ² is triggered when the new alignment and calibration constants are available if significant variations are observed. These new constants are updated for the next run, therefore, are used by the two stages of the software trigger, and for further reconstruction and selection offline.

The convergence of the automatic alignment procedure for tracker in case of large misalignment at the starting point is shown in Fig. 3.7. The starting point used in this plot is the final

²A run is one cycle of data collection by the detector. A typical run usually lasts around 1 hour and then a run change is forced to limit the file sizes. A run change can also be triggered by any change of the conditions during the data-taking.

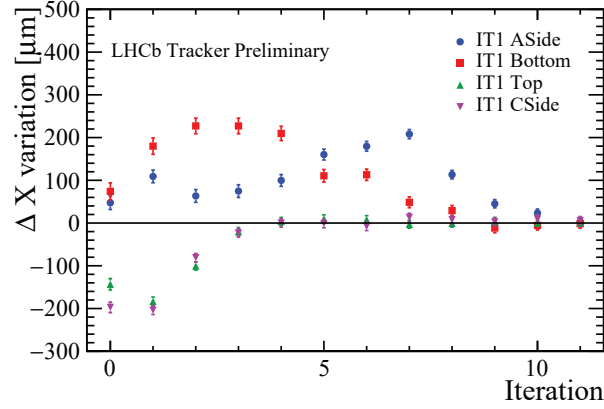


Figure 3.7: The convergence of the tracker alignment in case of large misalignment. Each point shows the change of the alignment parameter in the legend with respect to the previous iteration. The start point is the last updated database for the 2012 data.

2012 database. Due to the mechanical intervention during the LS1, movements of $1 \sim 2$ mm for IT boxes are expected.

The VELO halves are moved every fill in order to be at a safe distance from the beam during LHC injection, thus the alignment may change for each fill. A maximum variation of the real sensor positions due to this movement is of an order of $\mathcal{O}(10 \mu\text{m})$ over time which can be measured with a precision better than $\mathcal{O}(2 \mu\text{m})$ with the alignment procedure. The detector conditions for tracker may change mainly due to the magnet polarity switch or technical stops. Small fluctuations of about $100 \mu\text{m}$ and 1 mrad for the tracker are observed in Run I over time for the translational and rotational degrees of freedom (T_x and R_z), respectively.

The VELO, tracker and muon system alignment are performed in a defined subsequence for each fill. The VELO alignment runs at the beginning of each fill and the alignment constants are updated immediately if required. Alignment of the tracker is run after the VELO and an update is expected every few weeks. Finally, the muon system alignment is run after the tracker. Variations are not expected [53] and the alignment is used for monitoring purposes.

3.3 Tracker alignment monitoring

At the beginning of every fill a new alignment is evaluated for the tracker stations (ST and OT) if enough D^0 candidates (more than $50k$) are reconstructed. In case the new alignment is being significantly different with respect to the old one, the alignment is updated in the database to be used for the reconstruction of the following runs. A new entry in the LHCb logbooks (Alignment and Calibration) [87] is created after each new alignment task. In case of the new alignment is significantly different from the old one, a list of selected quality plots are produced by the alignment task. Four categories of the information are chosen:

- Track quality:
 - the probability of the track χ^2 versus its momentum (p), pseudorapidity (η) and polar angle (ϕ) for all reconstructed tracks;
 - the probability of the track χ^2 versus its momentum for different track segments: VELO and T for long tracks reconstruction, downstream and VELO;
 - the curvature ratio of the T and the VeloTT segments with respect to the full track.
- D^0 candidates: tracker alignment has significant impact on mass distributions and effects observed there could hint at possible misalignment.
 - mass distributions of the D^0 candidates used for the alignment;
 - the D^0 mass versus its momentum, angle between D^0 decay plane and y -axis (ϕ_{matt}), transverse momentum (p_T) and pseudorapidity (η).
- TT and IT alignment quality: the overlap residuals show the distribution of the difference of track residuals in two consecutive nodes related to the same layer.
 - the residuals in the IT boxes integrating over the 3 stations and the 4 layers of each station;
 - the residuals in the TT layers.
- Tracker alignment convergence:
 - the track χ^2 per degree of freedom (χ^2/ndf) versus the iteration number;
 - the variation of the global χ^2/ndf per iteration;
 - the difference between one iteration and the previous one for the chosen degrees of freedom for alignment (alignment constants): translations in TT layers, IT1 boxes, IT2 boxes, IT3 boxes and OT layers along z -axis.

The automatic update of the alignment constants in the database has been switched on since 03/11/2015 for the tracker. The top and bottom plots in Fig. 3.8 show the corrections of the IT1 positions in x - and z -axes obtained by the real time procedure with respect to the initial alignment constants for each alignment job run automatically every fill, respectively. The alignment constants evaluated for two different fills may vary due to statistical fluctuations even without real movement as different input data samples are used. The alignment procedure precision for IT1 is $\mathcal{O}(50\ \mu\text{m})$ in x -axis and $\mathcal{O}(200\ \mu\text{m})$ in z -axis, mainly due to the spatial resolutions of the subdetector. When a large deviation of the position of a tracker element is observed, the alignment is updated.

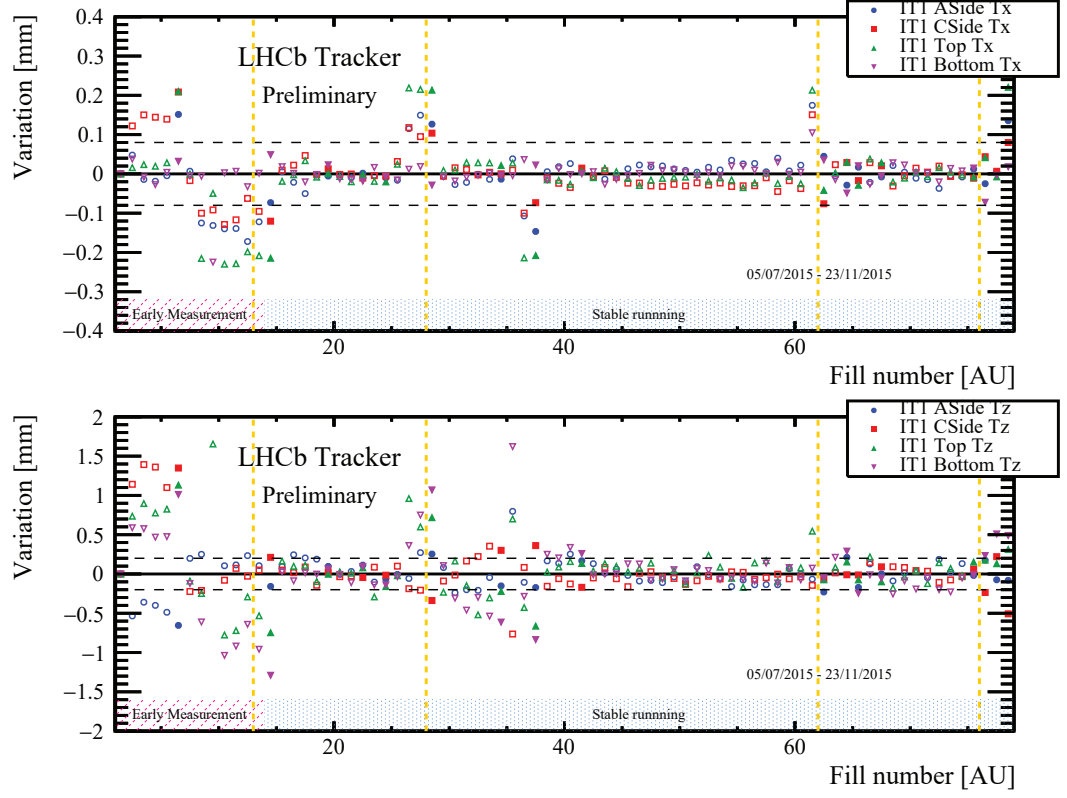


Figure 3.8: Tracker alignment variations in x -axis (top) and z -axis (bottom) respect to the start value for IT1 in each fill. The full markers are the alignments updated in the database and used as start value for the next fill; the open markers are the alignments performed but not updated in the database, thus not used by the following fill. The dashed vertical lines indicate the change of magnet polarity. If the variation is out of the range between the dashed horizontal lines, a warning is triggered and further quality checks are required.

4 Study of the photon polarisation in $B_s^0 \rightarrow \phi\gamma$ decays

This chapter describes the detailed information on the measurement of the parameter A^Δ in $B_s^0 \rightarrow \phi\gamma$ decays at LHCb, by performing a time-dependent analysis. The parameter A^Δ is sensitive to the polarisation of the emitted photons in $B_s^0 \rightarrow \phi\gamma$ decays. The sum of the time-dependent decay rates of B_s^0 and \bar{B}_s^0 decaying into $\phi\gamma$ (Eq. 1.8) is proportional to

$$e^{-\Gamma_s t} \left(\cosh \frac{\Delta\Gamma_s t}{2} - A^\Delta \sinh \frac{\Delta\Gamma_s t}{2} \right), \quad (4.1)$$

for an approximately equal mixture of B_s^0 and \bar{B}_s^0 mesons. The measurement of the amplitude of $\sinh \frac{\Delta\Gamma_s t}{2}$ term, *i.e.* A^Δ , is very sensitive to the reconstruction and selection efficiency of the decay time, which is referred to as the acceptance in the following text. Thus, the key element to measure the A^Δ value in the decay of $B_s^0 \rightarrow \phi\gamma$ is to understand the decay time acceptance for the trigger, the selection and the reconstruction requirements. The acceptance is controlled based on a data-driven method with a kinematically similar control channel, the $B^0 \rightarrow K^{*0}\gamma$ decay¹. The selection of $B_s^0 \rightarrow \phi\gamma$ and $B^0 \rightarrow K^{*0}\gamma$ candidates is designed to maximise the signal significance and to minimise the acceptance difference in the two channels, based on the studies of simulated samples.

4.1 Event reconstruction and selection

The full dataset corresponding to an integrated luminosity of 3 fb^{-1} , collected with the LHCb detector during Run I, is used in this analysis. The $B_s^0 \rightarrow \phi\gamma$ and $B^0 \rightarrow K^{*0}\gamma$ simulated samples of about 9 million events each are generated with Run I conditions. The simulated events are reconstructed and selected using the same methods as their data counterparts. A momentum scaling and smearing is applied to the charged tracks and the photon in the simulated samples to better describe data.

¹The $B^0 \rightarrow K^{*0}\gamma$ decay is called signal decay throughout the text, except for the decay time fits where it served as the control channel.

4.1.1 Photon energy post-calibration

The photon is the dominant contributor to the momentum resolution of the reconstructed B candidates due to the calorimeter resolution. The importance of the ECAL calibration is studied in simulation [12]: a 3% miscalibration results in an approximate 20% increase of the reconstructed B_s^0 mass resolution in $B_s^0 \rightarrow \phi\gamma$ decays. The intercalibration [12, 42, 88] of the absolute photon energy scale in the ECAL channels is performed using the LED system and the energy flow method, as well as large samples of reconstructed π^0 s and electrons. The final precision of the channel-to-channel intercalibration is estimated to be about 1%. The photon momentum is evaluated from the ECAL deposits taking into account geometrical and material effects as well as energy loss in the PS sampler and extra pile-up energy in the ECAL cluster area. Inaccuracy in the balance of the various contributions to the calorimetric energy, mostly tuned on low energy photons, induces non-linear effects resulting in a small bias, at the percent level, on the high-momentum photon from radiative decays. The position of the reconstructed signal B mass peak in principle could allow to estimate the global miscalibration factor for photons of very high energy. A dedicated post-calibration [89], designed to align the reconstructed B^0 mass of $B^0 \rightarrow K^{*0}\gamma$ candidates with the expected B^0 mass [39], is applied on the photon energy to correct the observed bias. The correction factors, depending on the photon type (converted/unconverted) and on the ECAL granularity area, are applied to the photon momentum and propagated to all relevant kinematical variables, including the reconstructed decay time and mass.

4.1.2 Trigger requirements

Candidate radiative decay events are required to pass a high- E_T photon trigger to reduce the photon combinatorial background, where there are about 10 calorimetric photons per event on average. To build the signal $B_s^0 \rightarrow \phi\gamma$ and $B^0 \rightarrow K^{*0}\gamma$ candidates, the trigger lines select two charged tracks and a high energy photon. Detailed trigger criteria applied in each line are documented in Ref. [90] for years 2011 and 2012.

At the hardware stage, the photon candidate must be triggered by one of the electromagnetic lines. The L0Photon line requires that the photon candidate passes the following criteria: E_T thresholds between 2.5 and 2.96 GeV and an SPD multiplicity below 600. The L0Electron line is incorporated to increase the efficiency due to photon conversions, where around $\sim 20\%$ photons are converted into electron-position pairs downstream the dipole magnet and before the SPD detector and has similar E_T thresholds. Two extra L0 lines, L0PhotonHi and L0ElectronHi, are used to select even higher p_T photons with a threshold of $E_T > 4.2$ GeV.

At the first software trigger stage, events are selected if a high- p_T track is reconstructed. In the case of either L0Photon or L0Electron line being fired, the Hlt1TrackAllL0 line imposes standard track requirements with $p > 10.0(3.0)$ GeV/ c and $p_T > 1.6(1.7)$ GeV/ c in year 2011 (2012) in order to access regions of the phase space with a softer photon and harder tracks. Otherwise, with either the L0PhotonHi or L0ElectronHi line fired, the Hlt1TrackPhoton line is

required, to select candidates with a harder photon and softer tracks with $p > 6.0(3.0) \text{ GeV}/c$ in year 2011 (2012) and $p_T > 1.2 \text{ GeV}/c$.

At the second software trigger stage, the exclusive radiative HLT2 lines, H1t2Bs2PhiGamma and H1t2Bd2KstGamma, are applied to select $B^0 \rightarrow K^{*0}\gamma$ and $B_s^0 \rightarrow \phi\gamma$ candidates, respectively. The track selected by HLT1 lines must form a K^{*0} or ϕ candidate when combined with an additional track. The invariant mass of the combination of the K^{*0} (ϕ) candidate and the photon candidate is required to be within a $\pm 1 \text{ GeV}/c^2$ mass window of the B^0 (B_s^0) mass.

4.1.3 STRIPPING and offline selections

Selections of $B_s^0 \rightarrow \phi\gamma$ and $B^0 \rightarrow K^{*0}\gamma$ candidates [89] are mainly driven by acceptance studies to achieve a close decay time acceptance between the two channels whilst maximising the signal significance and keeping a rather low background contribution (especially for those backgrounds contributing in the signal region). The $B_s^0 \rightarrow \phi\gamma$ and $B^0 \rightarrow K^{*0}\gamma$ candidates are reconstructed from two oppositely charged particles and a photon. Detailed information of the STRIPPING lines is documented in Table A.1 and Table A.2.

A requirement on the impact parameter (IP) of $\chi_{\text{IP}}^2 > 25$ on charged tracks is used to select tracks that are incompatible with any primary vertices (PVs). The χ_{IP}^2 is defined as the difference in the χ^2 of the PV fit reconstructed with and without the considered track. The maximum of the transverse momentum p_T of the two tracks is required to be larger than $1700 \text{ MeV}/c$ if the H1t1TrackA11L0 line is fired, and larger than $1200 \text{ MeV}/c$ in the H1t1TrackPhoton case. The particle identification (PID) information, obtained separately from the muon, RICH, and the calorimeter system, and the tracking information are combined using multivariate techniques to provide a single set of ProbNNX variables based on the particle hypotheses, where X stands for e , μ , π , K and p [42, 91]. The charged particles are identified as kaons if $\text{ProbNNK} > 0.2$ and as pions if $\text{ProbNN}\pi > 0.2$ and $\text{ProbNNK} < 0.2$. The efficiencies of the particle (mis)identifications are computed using the PIDCalib package [91, 92] based on the pure calibration samples for different types of charged particles.

The γ/π^0 separation [93] is performed by means of a multivariate discriminator that combines ECAL and PS cluster shape information. It effectively rejects the background from merged π^0 s. The value of the γ/π^0 separation variable is requested to be greater than 0.6. Since the performance of the γ/π^0 separation variable is not well reproduced by the simulation, the variable in simulated samples is weighted to reproduce its performance in data with a γ/π^0 separation tool [93] based on pure calibration samples for photons and merged π^0 s.

Additional requirements on the tracks and photons are introduced to reduce the difference between data and simulated events due to the online/offline momentum resolution differences: events that pass H1t1TrackA11L0 must have at least one track that fires the trigger and has a $p_T > 1.7 \text{ GeV}/c$, and also have a photon with $p_T > 3 \text{ GeV}/c$; events that pass H1t1TrackPhoton must have at least one track that fires the trigger and has a $p_T > 1.2 \text{ GeV}/c$, and also have a

photon with $p_T > 4.2 \text{ GeV}/c$.

Two oppositely charged particles are used to build the vector mesons K^{*0} and ϕ from a kaon-pion combination for K^{*0} , and a kaon-kaon combination for the ϕ candidate. The K^{*0} (ϕ) candidates are accepted if they form a good quality vertex and have an invariant mass within $\pm 100 \text{ MeV}/c^2$ ($\pm 15 \text{ MeV}/c^2$) of the K^{*0} (ϕ) mass [39].

The selected vector meson candidate is combined with the photon candidate to build a B candidate. The reconstructed invariant mass of the B candidate is required to be between $4 \text{ GeV}/c^2$ and $7 \text{ GeV}/c^2$ and the reconstructed p_T must be greater than $3 \text{ GeV}/c$. The DIRA, defined as the angle between the momentum of the B and the vector going from the PV to the decay vertex (DV), is nonzero due to reconstruction effects and missing particles. The B^0 (B_s^0) candidates must point to a PV with $\chi_{\text{IP}}^2 < 9$ and $\text{DIRA} < 40(60) \text{ mrad}$. The distribution of the helicity angle θ_H , defined as the angle between the momentum of any of the daughters of the vector meson (V) and the momentum of the B candidate in the rest frame of the vector mesons, is expected to follow a $\sin^2 \theta_H$ function for $B \rightarrow V\gamma$, and a $\cos^2 \theta_H$ for $B \rightarrow V\pi^0$ background. A requirement of $|\cos \theta_H| < 0.8$ is applied to further reduce the $B \rightarrow V\pi^0$ background.

The decay time of the B candidates is calculated from the information of their reconstructed mass, reconstructed momentum and the flight distance with respect to their production vertex. The decay time reconstruction efficiency depends on the location and phase space of the particles, especially at the edges of the detector where a homogeneous reconstruction cannot be guaranteed [94, 95, 96]. A fiducial cut requiring tracks to be within the acceptance $2 < \eta < 4.5$ and the z position of the PV within $\pm 100 \text{ mm}$ window around zero is applied to remove these regions. To reduce the contribution originating from a wrongly associated PV, the event is required to have either only 1 PV or that the χ_{IP}^2 of the B candidate with respect to the second nearest PV in the event to be larger than 50.

The reconstructed B invariant mass distributions for $B^0 \rightarrow K^{*0}\gamma$ and $B_s^0 \rightarrow \phi\gamma$ decays are shown in Fig. 4.1. At the trigger level, the reconstruction is different from the offline, especially the ECAL calibration is different [97], which is the dominant contribution to the resolution difference between online and offline in radiative decays. The $\pm 1 \text{ GeV}/c^2$ mass window on the reconstructed B invariant masses imposed in both the trigger and the STRIPPING results in an acceptance bias in the vicinity of the mass window borders. Due to border effects, we restrict the mass range to be between $4600 \text{ MeV}/c^2$ and $6000 \text{ MeV}/c^2$.

4.2 Signal lineshapes

Lineshapes of the signal mass distributions are determined by the detector resolution and the radiative characteristics of B meson decays [98]. In the low mass region, the contribution is mainly from possible losses in the photon energy due to the fiducial volume of the calorimeter. The tail at high masses can be partially explained by the spread in the error of the reconstructed B meson mass. Large pile-up deposit in the ECAL cluster can also contribute to the photon

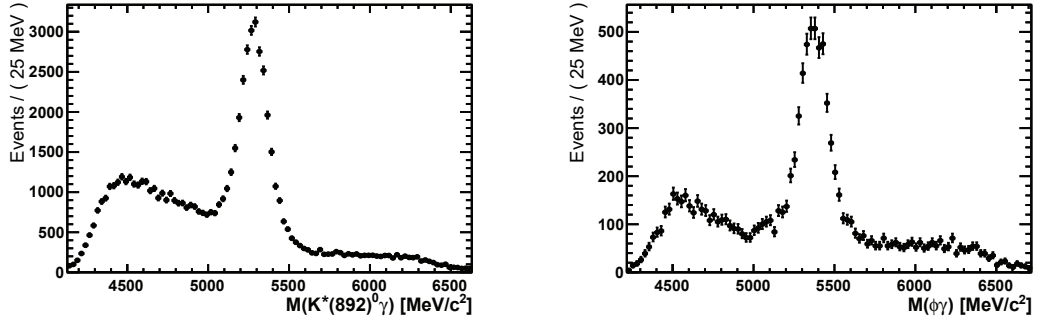


Figure 4.1: The reconstructed B invariant mass distributions of the $B^0 \rightarrow K^{*0}\gamma$ (left) and $B_s^0 \rightarrow \phi\gamma$ (right) candidates in data.

Table 4.1: Fit results on the B invariant mass distributions from the simulated samples of $B^0 \rightarrow K^{*0}\gamma$ and $B_s^0 \rightarrow \phi\gamma$ decays.

Parameter	Unit	$B^0 \rightarrow K^{*0}\gamma$	$B_s^0 \rightarrow \phi\gamma$
μ	MeV/c^2	5282.0 ± 0.4	5367.9 ± 0.4
σ	MeV/c^2	89.4 ± 0.4	89.2 ± 0.4
α_L		2.35 ± 0.03	2.38 ± 0.03
α_R		-1.53 ± 0.03	-1.49 ± 0.03
n_L		0.67 ± 0.05	0.58 ± 0.05
n_R		7.1 ± 0.6	7.6 ± 0.6

candidate reconstruction.

A double-sided Crystal Ball function [99] is used to describe the invariant mass distribution of the reconstructed B candidates:

$$\text{CB}(m; \mu, \sigma, \alpha_L, n_L, \alpha_R, n_R) = \begin{cases} A_L \left(B_L - \frac{m - \mu}{\sigma} \right)^{-n_L} & \text{for } \frac{m - \mu}{\sigma} \leq -\alpha_L \\ \exp \left\{ -\frac{(m - \mu)^2}{2\sigma^2} \right\} & \text{for } -\alpha_L < \frac{m - \mu}{\sigma} < \alpha_R, \\ A_R \left(B_R + \frac{m - \mu}{\sigma} \right)^{-n_R} & \text{for } \frac{m - \mu}{\sigma} \geq \alpha_R \end{cases}, \quad (4.2)$$

where $\alpha_{L(R)} > 0$ and

$$A_i = \left(\frac{n_i}{|\alpha_i|} \right)^{n_i} \exp \left\{ -\frac{|\alpha_i|^2}{2} \right\}, \quad B_i = \frac{n_i}{|\alpha_i|} - |\alpha_i|, \quad \text{with } i \in \{L, R\}. \quad (4.3)$$

Simulated samples of $B_s^0 \rightarrow \phi\gamma$ and $B^0 \rightarrow K^{*0}\gamma$ decays are used to study the signal shapes of the signal channels. Results of the mass fits on the simulated signal samples are shown in Fig. 4.2 and Table 4.1. To fit the data, the parameters $n_{L(R)}$ and $\alpha_{L(R)}$ are fixed to the values in simulation whilst the μ and σ are left unconstrained.

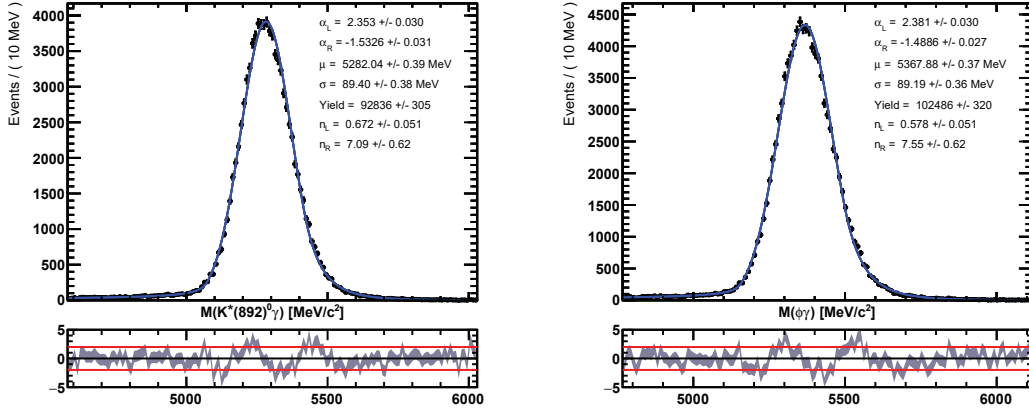


Figure 4.2: Fits on the reconstructed invariant mass distributions of the $B^0 \rightarrow K^{*0}\gamma$ decay (left) and the $B_s^0 \rightarrow \phi\gamma$ decay (right) using the simulated signal samples.

4.3 Background contributions

The number of expected events for a given B decay, $N(B_q \rightarrow X)$, is

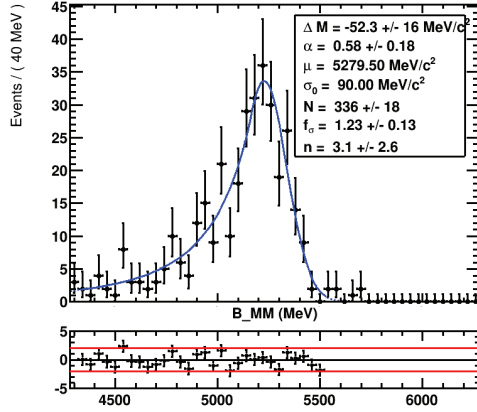
$$N(B_q \rightarrow X) = \mathcal{L} \cdot 2 \cdot \sigma(pp \rightarrow b\bar{b}X) \cdot f_q \cdot \mathcal{B}(B_q \rightarrow X) \cdot \epsilon_{\text{total}}, \quad (4.4)$$

where \mathcal{L} is the integrated luminosity, $\sigma(pp \rightarrow b\bar{b}X)$ is the cross-section of b -hadron production in a pp collision with a factor 2 for a pair of b quarks, f_q is the hadronisation probability for a b quark to form a b -hadron containing a q quark, $\mathcal{B}(B_q \rightarrow X)$ is the total branching fraction of the decay into the final states, and ϵ_{total} is the total reconstruction and selection efficiency including the detector acceptance, material interactions, tracking efficiencies, trigger and stripping efficiencies and the offline selection efficiencies. Based on Eq. 4.4, the relative contamination from any B decay to signal channel, $C_{B_q \rightarrow X}$, can be written as

$$C_{B_q \rightarrow X} = \frac{N(B_q \rightarrow X)}{N(\text{signal decay})} = \frac{f_q}{f_{b\text{-flavor}}^{\text{signal}}} \cdot \frac{\mathcal{B}(B_q \rightarrow X)}{\mathcal{B}(\text{signal decay})} \cdot \frac{\epsilon_{\text{total}}^{B_q \rightarrow X}}{\epsilon_{\text{total}}^{\text{signal}}}. \quad (4.5)$$

The total efficiency, ϵ_{total} , is evaluated with the MC simulated samples. For the uncertainties, the uncertainty on generator level cut efficiency is taken as 0.5% and the PID efficiency uncertainty is assumed to be 0.1% per track.

Any B decay with at least two tracks and a high- E_T neutral particle (γ or π^0) in the final state is a potential candidate to be reconstructed as signal. Detailed studies have been performed in order to understand the shape and the level of contribution of each background by means of reconstructing various simulated background processes as signal decay.



Parameter	Value
ΔM	$-52 \pm 16 \text{ MeV}/c^2$
f_σ	1.2 ± 0.1
α	0.6 ± 0.2
n	3.1 ± 2.6

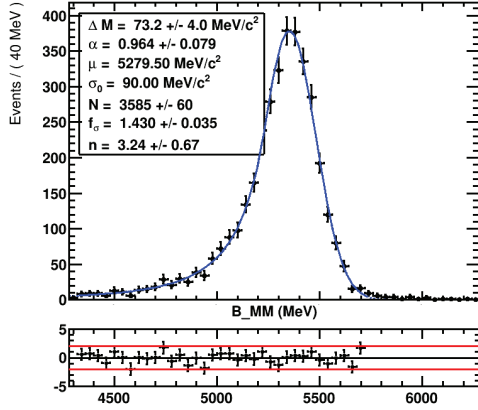
Figure 4.3: The $K^{*0}\gamma$ invariant mass reconstructed in the simulated $B^0 \rightarrow K^{*0}\pi^0$ sample (black points) with the fit model (solid blue line) overlaid. The parameters of the model from the fit are reported in the table on the right.

4.3.1 Merged π^0 backgrounds

A simulated sample of $B^0 \rightarrow K^{*0}\pi^0$ decays is used to compute the contamination factor $C_{B^0 \rightarrow K^{*0}\pi^0}$ for the $B^0 \rightarrow K^{*0}\gamma$ candidates. The discrepancy between the data and simulation for the γ/π^0 separation variable is handled by re-weighting the variable as a function of the neutral's transverse momentum and pseudorapidity with pure selected $B^0 \rightarrow K^{*0}\gamma$ and $D^0 \rightarrow K^-\pi^+\pi^0$ data samples. The decays of B^0 into $K^+\pi^-\pi^0$ final state via other decay paths are found to be negligible. The contamination fraction of merged π^0 background for $B^0 \rightarrow K^{*0}\gamma$ decays ($C_{B^0 \rightarrow K^{*0}\pi^0}$) is found to be $(2.05 \pm 0.39)\%$.

A fit on the $K^{*0}\gamma$ invariant mass reconstructed in the simulated $B^0 \rightarrow K^{*0}\pi^0$ sample is modelled with a Crystal Ball function as shown in Fig. 4.3. The mean and resolution of the reconstructed mass in the fit function are defined with respect to the signal model parameters such that $m_0 = \mu + \Delta M$ and the $\sigma = f_\sigma \cdot \sigma_0$, where μ and σ_0 are fixed to the B^0 (B_s^0) mass and $90 \text{ MeV}/c^2$ which is from the fits on the simulated signal samples, respectively.

A potential contamination to the $B_s^0 \rightarrow \phi\gamma$ decay by merged π^0 s could be $B_s^0 \rightarrow \phi\pi^0$ decays. The branching fraction of the $B_s^0 \rightarrow \phi\pi^0$ decay is predicted to be 1.6×10^{-7} [100] which results in a negligible contamination factor. However, to be conservative, the ratio of the branching ratios of $B_s^0 \rightarrow \phi\gamma$ and $B_s^0 \rightarrow \phi\pi^0$ is assumed to be the same as the K^{*0} modes. The contamination of the $B_s^0 \rightarrow \phi\gamma$ decays due to $B_s^0 \rightarrow \phi\pi^0$ decays is calculated under the assumption that the ratio of the selection efficiencies of the photon and π^0 are the same for the B^0 and B_s^0 modes, since no simulated sample for $B_s^0 \rightarrow \phi\pi^0$ is available. Another source of the main difference between the two decay modes is the B helicity cut. The distribution of the helicity angle, θ_H , is asymmetric for $B^0 \rightarrow K^{*0}\gamma$ decays because of the mass difference between the kaon and pion in a K^{*0} decay, whilst it is symmetric for $B_s^0 \rightarrow \phi\gamma$ decays. Then the contamination $C_{B_s^0 \rightarrow \phi\pi^0}$ to $B_s^0 \rightarrow \phi\gamma$ is computed by multiplying $C_{B^0 \rightarrow K^{*0}\pi^0}$ without the helicity cut by the ratio of the



Parameter	Value
ΔM	$73.2 \pm 4.0 \text{ MeV}/c^2$
f_σ	1.43 ± 0.04
α	0.96 ± 0.08
n	3.2 ± 0.7

Figure 4.4: Distribution of the reconstructed $K^{*0}\gamma$ invariant mass in the simulated $\Lambda_b^0 \rightarrow \Lambda^*\gamma$ sample with parameters from the fit reported in the table on the right.

efficiency of the helicity angle cut, $R_{\cos\theta_H}$, between $B_s^0 \rightarrow \phi\pi^0$ and $B_s^0 \rightarrow \phi\gamma$. The ratio $R_{\cos\theta_H}$ is computed directly from the expected shapes, which are $1 - \cos^2\theta_H$ for $B_s^0 \rightarrow \phi\gamma$ decays and $\cos^2\theta_H$ for $B_s^0 \rightarrow \phi\pi^0$ decays. The contamination of merged π^0 background for the $B_s^0 \rightarrow \phi\gamma$ decay, $C_{B_s^0 \rightarrow \phi\pi^0}$, is found to be $(1.60 \pm 1.60)\%$ with a 100% uncertainty assigned.

4.3.2 Baryonic radiative decays

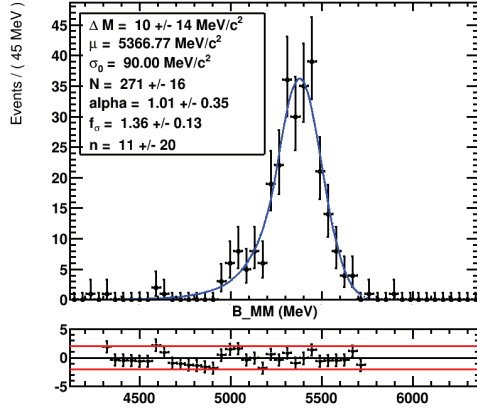
Baryonic radiative decays to the final state $pK\gamma$ could contaminate the signal via the misidentification of the proton as a pion for $B^0 \rightarrow K^{*0}\gamma$ decays, or a kaon for $B_s^0 \rightarrow \phi\gamma$ decays. The branching ratio of $\Lambda_b^0 \rightarrow \Lambda^*(pK)\gamma$ with pK invariant mass below $2.5 \text{ GeV}/c^2$ is estimated in Ref. [98] as

$$\mathcal{B}(\Lambda_b^0 \rightarrow \Lambda^*(pK^-)\gamma) \times \frac{f_{\Lambda_b^0}}{f_d} = (4.2 \pm 0.7) \times 10^{-6}, \quad (4.6)$$

where the uncertainty is purely statistical and Λ^* stands for the $\Lambda(1520)$ and further massive baryon resonances promptly decaying into a pK final state. The contamination from $\Lambda_b^0 \rightarrow \Lambda^*(pK)\gamma$ decays is found to be $(1.77 \pm 0.39)\%$ to $B_s^0 \rightarrow \phi\gamma$ and $(1.38 \pm 0.23)\%$ to $B^0 \rightarrow K^{*0}\gamma$. The reconstructed $K^{*0}\gamma$ and $\phi\gamma$ invariant mass distributions in the simulated $\Lambda_b^0 \rightarrow \Lambda(1520)(pK)\gamma$ sample are shown in Fig. 4.4 and Fig. 4.5, respectively. The Crystal Ball functions are used to fit the samples.

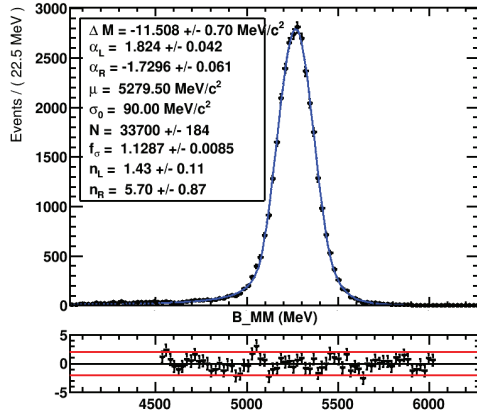
4.3.3 Backgrounds with particle misidentifications

Radiative B decays from $B^0 \rightarrow \rho\gamma$ and the cross-feed between $B^0 \rightarrow K^{*0}\gamma$ and $B_s^0 \rightarrow \phi\gamma$ can contribute to the signal region. The contaminations of $B^0 \rightarrow \rho\gamma$ and $B_s^0 \rightarrow \phi\gamma$ to $B^0 \rightarrow K^{*0}\gamma$ are found to be $(0.15 \pm 0.03)\%$ and $(0.24 \pm 0.03)\%$, respectively. The contamination of $B^0 \rightarrow K^{*0}\gamma$ to



Parameter	Value
ΔM	$10 \pm 14 \text{ MeV}/c^2$
f_σ	1.4 ± 0.1
α	1.0 ± 0.4
n	11 ± 20

Figure 4.5: Distribution of the reconstructed $\phi\gamma$ invariant mass in the simulated $\Lambda_b^0 \rightarrow \Lambda^*\gamma$ sample with parameters from the fit reported in the table on the right.



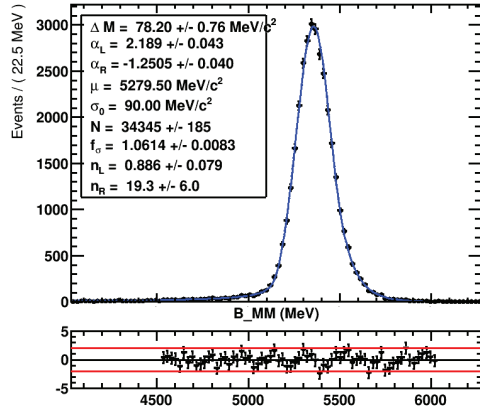
Parameter	Value
ΔM	$-11.5 \pm 0.7 \text{ MeV}/c^2$
f_σ	1.13 ± 0.01
α_L	1.82 ± 0.04
α_R	-1.73 ± 0.06
n_L	1.4 ± 0.1
n_R	5.7 ± 0.9

Figure 4.6: The $K^{*0}\gamma$ invariant mass distribution reconstructed in the simulated $B_s^0 \rightarrow \phi\gamma$ sample with parameters from the fit reported in the table on the right.

$B_s^0 \rightarrow \phi\gamma$ is $(0.10 \pm 0.02)\%$. The double misidentifications of $B^0 \rightarrow K^{*0}\gamma$ with the pion identified as a kaon and the kaon identified as a pion in $B^0 \rightarrow K^{*0}\gamma$ candidates with correct particle hypotheses assigned is below the level of 0.05%, which is negligible.

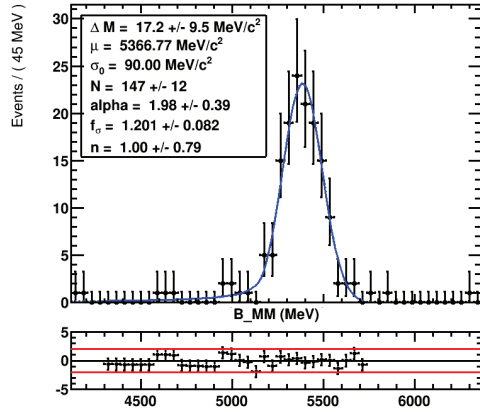
The reconstructed $K^{*0}\gamma$ invariant masses in the simulated $B_s^0 \rightarrow \phi\gamma$ sample and $B^0 \rightarrow \rho\gamma$ sample fitted with double-sided Crystal Ball functions are shown in Fig. 4.6 and Fig. 4.7, respectively. The reconstructed $\phi\gamma$ invariant mass distribution in the simulated $B^0 \rightarrow K^{*0}\gamma$ sample is shown in Fig. 4.8 with the Crystal Ball function used to fit the mass distribution.

Chapter 4. Study of the photon polarisation in $B_s^0 \rightarrow \phi\gamma$ decays



Parameter	Value
ΔM	$78.2 \pm 0.8 \text{ MeV}/c^2$
f_σ	1.06 ± 0.01
α_L	2.19 ± 0.04
α_R	-1.25 ± 0.04
n_L	0.9 ± 0.1
n_R	19.3 ± 6.0

Figure 4.7: The $K^{*0}\gamma$ invariant mass distribution reconstructed in the simulated $B^0 \rightarrow \rho\gamma$ sample with parameters from the fit reported in the table on the right.



Parameter	Value
ΔM	$17.2 \pm 9.5 \text{ MeV}/c^2$
f_σ	1.2 ± 0.1
α	2.0 ± 0.4
n	1.0 ± 0.8

Figure 4.8: The $\phi\gamma$ invariant mass distribution reconstructed in the simulated $B^0 \rightarrow K^{*0}\gamma$ sample with parameters from the fit reported in the table on the right.

4.3.4 Backgrounds from partially reconstructed B decays

Backgrounds from partially reconstructed B decays consist of events with the same final state as the signal decay when one or more particles are not reconstructed, with and without γ/π^0 and particle misidentifications. These backgrounds dominate in the low-mass region and their main sources are different for $B_s^0 \rightarrow \phi\gamma$ and $B^0 \rightarrow K^{*0}\gamma$ decays. The vertex isolation criteria which is powerful in reducing backgrounds from partially reconstructed B decays [101, 97] cannot be used in this analysis because it generates an intrinsic difference in the acceptances between $B^0 \rightarrow K^{*0}\gamma$ and $B_s^0 \rightarrow \phi\gamma$ channels.

Partially reconstructed background is modelled with an ARGUS function [102], convolved with a Gaussian resolution function:

$$\mathcal{P}(m; m_0, c, p) = \frac{2^{-p} c^{2(p+1)}}{\Gamma(p+1) - \Gamma(p+1, \frac{1}{2}c^2)} \cdot \frac{m^2}{m_0^2} \left(1 - \frac{m^2}{m_0^2}\right)^p \exp \left\{ \frac{1}{2} c^2 \left(1 - \frac{m^2}{m_0^2}\right) \right\}, \quad (4.7)$$

for $0 \leq m \leq m_0$, where c , m_0 , and p are the curvature, endpoint and power, respectively. $\Gamma(p+1)$ is the gamma function and $\Gamma(p+1, \frac{1}{2}c^2)$ is the upper incomplete gamma function. For $m > m_0$ the function returns zero.

4.3.4.1 Contributions to $B^0 \rightarrow K^{*0}\gamma$ decays

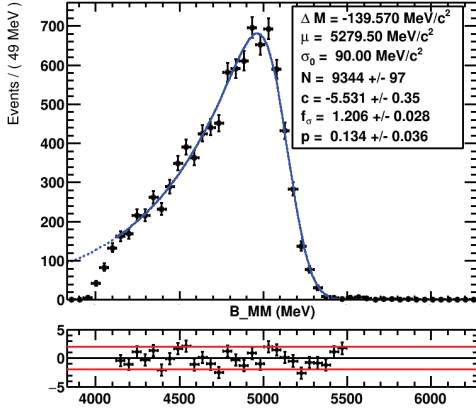
These backgrounds are subdivided into three main categories as listed below:

- decays of $B \rightarrow K\pi\pi\gamma$ with a pion missing in the final state;
- B decays containing $K\pi\eta$ in the final state with $\eta \rightarrow \gamma\gamma$ and a photon and/or one or more particles are not reconstructed;
- B decays containing $K\pi\pi^0$ in the final state where one or more particles in the decay are not reconstructed.

There are various B decays via different paths into a $K\pi\pi\gamma$ final state:

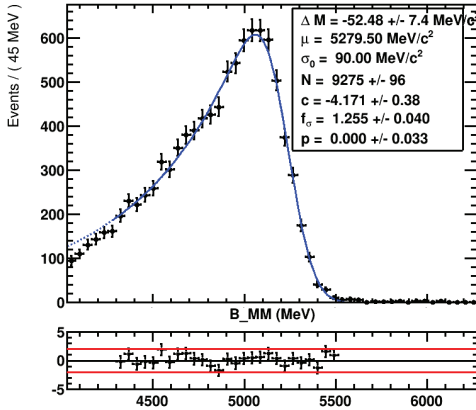
- $B^{0,+} \rightarrow K^+\pi^-\pi^{0,+}\gamma$ nonresonant;
- $B^{0,+} \rightarrow K^{*0}\pi^{0,+}\gamma$ nonresonant;
- $B^{0,+} \rightarrow K_{\text{res}}^{0,+}\gamma$ where K_{res} is a kaonic resonance as $K_1(1270)$, $K_1(1400)$, $K_2^*(1430)$, *etc.*

With a pion missing during reconstruction, these decays can contribute to the selected $K^{*0}\gamma$ candidates but at the lower mass region. The reconstructed $K^{*0}\gamma$ invariant mass distribution in the simulated $B \rightarrow K_1(1270)(K^{*0}\pi)\gamma$ samples is shown in Fig. 4.9 along with the results from the fit. Since the trigger introduces an acceptance effect around $1 \text{ GeV}/c^2$ below B^0 (B_s^0) mass [39], without affecting the overall shape, the sample without trigger selection applied is used in these studies to increase the available statistics and also allow a wider fit range to better estimate the c and p parameters.



Parameter	Value
ΔM	m_π
f_σ	1.21 ± 0.03
c	-5.5 ± 0.4
p	0.13 ± 0.04

Figure 4.9: The $K^{*0}\gamma$ invariant mass distribution reconstructed in the simulated $B \rightarrow K_1(1270)(K^{*0}\pi)\gamma$ sample with parameters from the fit reported in the table on the right.



Parameter	Value
ΔM	$-52.5 \pm 7.4 \text{ MeV}/c^2$
f_σ	1.26 ± 0.04
c	-4.2 ± 0.4
p	0.00 ± 0.03

Figure 4.10: The $K^{*0}\gamma$ invariant mass distribution reconstructed in the simulated $B^0 \rightarrow K^{*0}\eta$ sample with parameters from the fit reported in the table on the right.

The B decays to the $K\pi\pi\eta$ final state are mainly via $B \rightarrow K_{\text{res}}\eta$ where K_{res} stands for a higher kaonic resonances. Depending on whether the K_{res} decays into $K^{*0}\pi$, the reconstructed $K^{*0}\gamma$ invariant mass distributions have different shapes. In the case of the K_{res} not decaying into $K^{*0}\pi$, the shape of the $K^{*0}\gamma$ invariant mass distributions are quite close to the γ counterparts with the final state of $K\pi\pi\gamma$; otherwise, the decays of $B \rightarrow K_{\text{res}}(K^{*0}\pi)\eta$ are studied together with the backgrounds identified as the third category later on.

The background from $B^0 \rightarrow K^{*0}\eta$ decays contributes mainly to the signal region with only a photon missing, which introduces a long tail at the lower mass region. The contamination from $B^0 \rightarrow K^{*0}\eta$ decays is found to be $(2.04 \pm 0.14)\%$ and is a fixed contribution in the fit of the B^0 invariant mass, with both the shape and normalisation obtained from the simulated sample study. The reconstructed $K^{*0}\gamma$ invariant mass distribution is shown in Fig. 4.10.

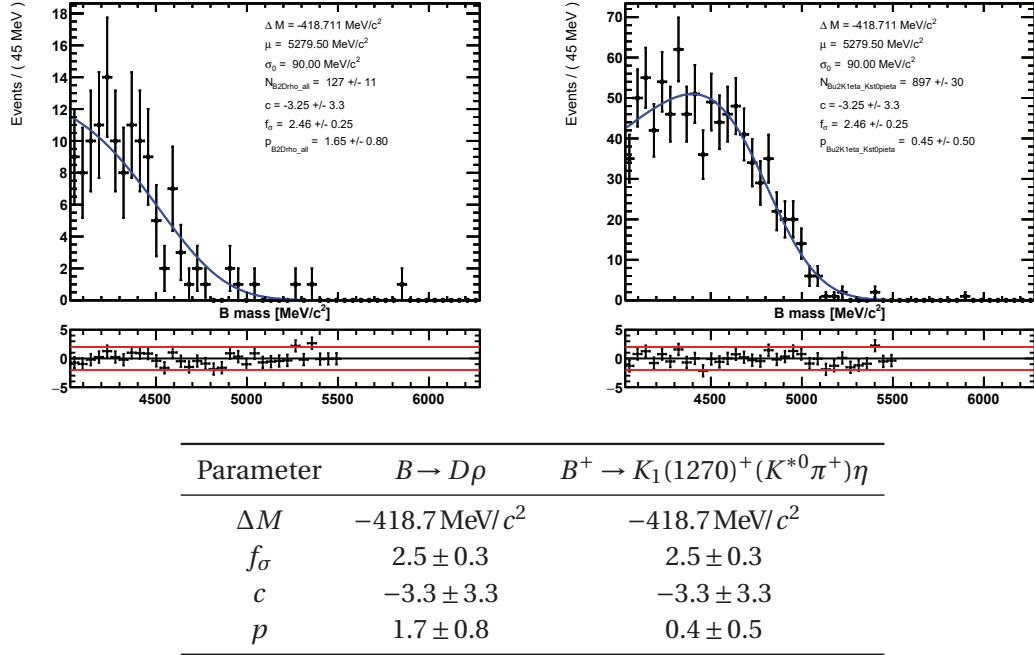


Figure 4.11: The $K^{*0} \gamma$ invariant mass reconstructed in (the sum of) $B \rightarrow D\rho$ simulated samples (top left) and $B^+ \rightarrow K_1(1270)^+(K^{*0}\pi^+)\eta$ simulated sample (top right) with parameters from the fits reported in the table (bottom).

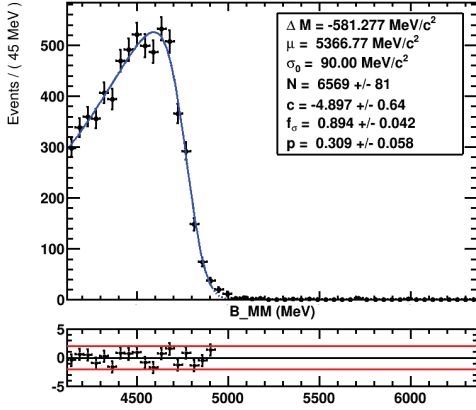
B decays containing $K\pi\pi^0$ in the final state with one or more particles in the decay not reconstructed will be noted as $B \rightarrow K\pi\pi^0 X$ hereafter. The background from $B \rightarrow K\pi\pi^0 X$ can include any decay with two oppositely charged particles combining with a neutral particle such as:

- $B^0 \rightarrow D^-(K^+\pi^-\pi^-)\rho^+(\pi^+\pi^0)$
- $B^+ \rightarrow D^0\rho^+(\pi^+\pi^0), D^0 \rightarrow K^+K^-, K^+\pi^-\pi^0, K^+\pi^-\pi^+\pi^-, \dots$

Due to the limited statistics for the simulated samples of $B \rightarrow D\rho$ decays, we perform a simultaneous fit between $B \rightarrow D\rho$ decays and $B^+ \rightarrow K_1(1270)^+(K^{*0}\pi^+)\eta$ decays by assuming the same resolution as shown in Fig. 4.11. The shape from the simulated $B \rightarrow D\rho$ samples will be used in the nominal mass fit and the one from $B \rightarrow K_1(1270)^+(K^{*0}\pi^+)\eta$ sample for the systematic uncertainty evaluation.

4.3.4.2 Contributions to $B_s^0 \rightarrow \phi\gamma$ decays

Due to the narrow mass window requirement on the ϕ mass and PID criteria on the kaons, the B decays with a kaon missing are found to be the dominant partially reconstructed background contributing to $B_s^0 \rightarrow \phi\gamma$ decays. The reconstructed $\phi\gamma$ invariant mass distribution in simulated $B^+ \rightarrow \phi K^+\gamma$ sample is shown in Fig. 4.12.



Parameter	Value
ΔM	m_{K^+}
f_σ	0.89 ± 0.04
c	-4.9 ± 0.6
p	0.3 ± 0.1

Figure 4.12: The $\phi\gamma$ invariant mass reconstructed in the simulated $B^+ \rightarrow \phi K^+ \gamma$ sample with parameters from the fit reported in the table on the right.

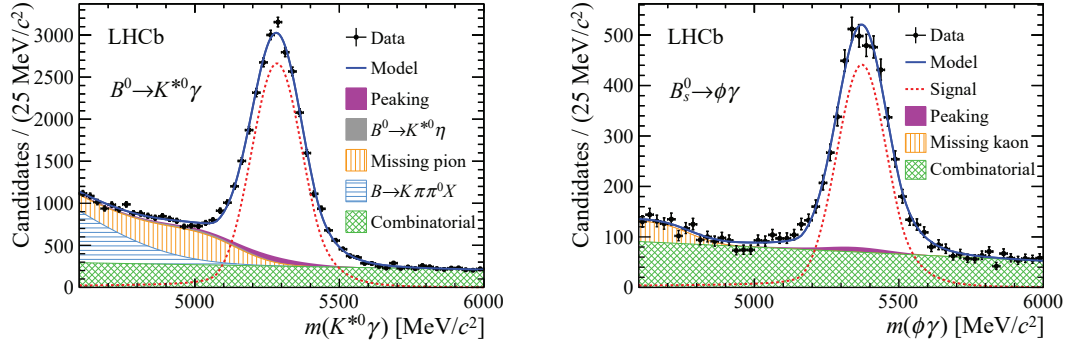
4.4 Fit on the reconstructed B mass spectra

4.4.1 Fit procedure

An unbinned extended maximum likelihood fit is performed on the selected B^0 (B_s^0) sample to fit the reconstructed B candidate mass spectra. The probability density function (PDF) is defined as

$$\mathcal{P}(m) = N_{\text{Signal}} \cdot [S(m) + \sum_k f_k \cdot P_k(m)] + \sum_i N_i \cdot B_i(m), \quad (4.8)$$

where $S(m)$ is the signal PDF, $P_k(m)$ are the peaking background PDFs with k representing different species of peaking backgrounds, and $B_i(m)$ is the partially reconstructed or combinatorial background PDF where i refers to different contributions to the background. N_{Signal} is the number of signal events with peaking backgrounds included, where f_k is the fraction of the peaking background k defined as $f_k = C_k / (1 + \sum_j C_j)$. N_i is the number of events from either the combinatorial background or one of the partially reconstructed backgrounds. The signal lineshape for B candidates is described by means of a double-tail Crystal Ball function with tail shape parameters determined from fits to the simulated signal samples, as discussed in Section 4.2. The shape parameters of the backgrounds are determined from fits to the simulated background samples and the normalisations of all the components are left unconstrained, with the exception of irreducible backgrounds in the signal region. Detailed information of all the background models except the combinatorial background can be found in Section 4.3. A first-order polynomial function is used to describe the combinatorial background distribution.


 Figure 4.13: Invariant mass fits of the $B^0 \rightarrow K^{*0}\gamma$ (left) and $B_s^0 \rightarrow \phi\gamma$ (right) candidates in data.

4.4.2 Fit to data

The fits of the reconstructed $K^{*0}\gamma$ and $\phi\gamma$ invariant mass distributions for the selected data samples are shown in Fig. 4.13, with the fit parameters detailed in Table 4.2. The number of signal candidates determined from the fits are 25760 ± 301 and 4214 ± 90 for the $B^0 \rightarrow K^{*0}\gamma$ and $B_s^0 \rightarrow \phi\gamma$ data samples, respectively. The uncertainties are purely statistical and the contribution from peaking backgrounds are included. The contribution from the peaking backgrounds are estimated to be 952 ± 114 and 142 ± 67 for the $B^0 \rightarrow K^{*0}\gamma$ and $B_s^0 \rightarrow \phi\gamma$ decays, respectively.

4.4.3 Validation of the mass fit model

In order to test the stability of the B^0 and B_s^0 invariant mass fits, a thousand pseudoexperiment [103] samples each have been generated using the parameters extracted from the fits shown in Fig. 4.13. The same fit models as used in Fig. 4.13 are performed on each pseudoexperiment sample. For each pseudoexperiment, the number of events for each component is sampled from a Poisson distribution with the mean given in Table 4.2. The pull distribution $\mathcal{P}(x)$ of a given parameter x is defined as

$$\mathcal{P}(x) = \frac{x_{\text{Fit}} - x_{\text{Gen}}}{\sigma_x}, \quad (4.9)$$

where the distribution of $\mathcal{P}(x)$ follows a Normal distribution in case of well behaved fits.

The pull distributions for the mean μ and resolution σ of the signal PDFs and the number of signal events N_{Signal} from these pseudoexperiments are shown in Fig. 4.14. Gaussian fits are performed on the pull distributions and the results are reported in Table 4.3. No significant inconsistency with a Normal distribution is observed in any of the pull distributions. Here the number of signal events includes peaking backgrounds as these backgrounds are considered as signal candidates in the decay time fits described later in this chapter.

Chapter 4. Study of the photon polarisation in $B_s^0 \rightarrow \phi\gamma$ decays

Table 4.2: Fit parameters for selected $B^0 \rightarrow K^{*0}\gamma$ (second column) and $B_s^0 \rightarrow \phi\gamma$ (third column) data samples. The sign “–” indicates that the contribution from the component is negligible.

Parameter	$B^0 \rightarrow K^{*0}\gamma$	$B_s^0 \rightarrow \phi\gamma$
N_{Signal}	25760 ± 301	4214 ± 90
μ (MeV/ c^2)	5284.1 ± 0.8	5371.9 ± 1.9
σ (MeV/ c^2)	87.8 ± 1.0	86.3 ± 2.0
$C_{B \rightarrow K^{*0}/\phi\pi^0}$	2.1%	1.6%
$C_{\Lambda_b^0 \rightarrow \Lambda^*(pK)\gamma}$	1.4%	1.8%
$C_{B^0 \rightarrow \rho\gamma}$	0.2%	–
$C_{B_s^0 \rightarrow \phi\gamma}$	0.2%	
$C_{B^0 \rightarrow K^{*0}\gamma}$		0.1%
$N_{\text{Combinatorial}}$	14088 ± 865	4004 ± 113
p_0 ($\frac{1}{\text{MeV}/c^2}$)	-0.16 ± 0.07	-0.27 ± 0.04
$C_{B \rightarrow \phi K\gamma}$	–	$(7.0 \pm 1.2)\%$
$C_{B \rightarrow K\pi\pi^0 X}$	$(19.2 \pm 1.0)\%$	–
$C_{B \rightarrow K^{*0}\pi\gamma}$	$(25.5 \pm 1.6)\%$	–
$C_{B^0 \rightarrow K^{*0}\eta}$	2.0%	–

Table 4.3: The mean μ and sigma σ of Gaussian fits to the pull distributions from the pseudo-experiments.

	$B^0 \rightarrow K^{*0}\gamma$		$B_s^0 \rightarrow \phi\gamma$	
	μ	σ	μ	σ
pull μ	-0.04 ± 0.03	0.99 ± 0.02	-0.00 ± 0.03	0.93 ± 0.02
pull σ	$+0.03 \pm 0.03$	1.00 ± 0.02	-0.02 ± 0.03	0.99 ± 0.02
pull N_{Signal}	-0.02 ± 0.03	0.98 ± 0.02	$+0.03 \pm 0.03$	1.01 ± 0.02

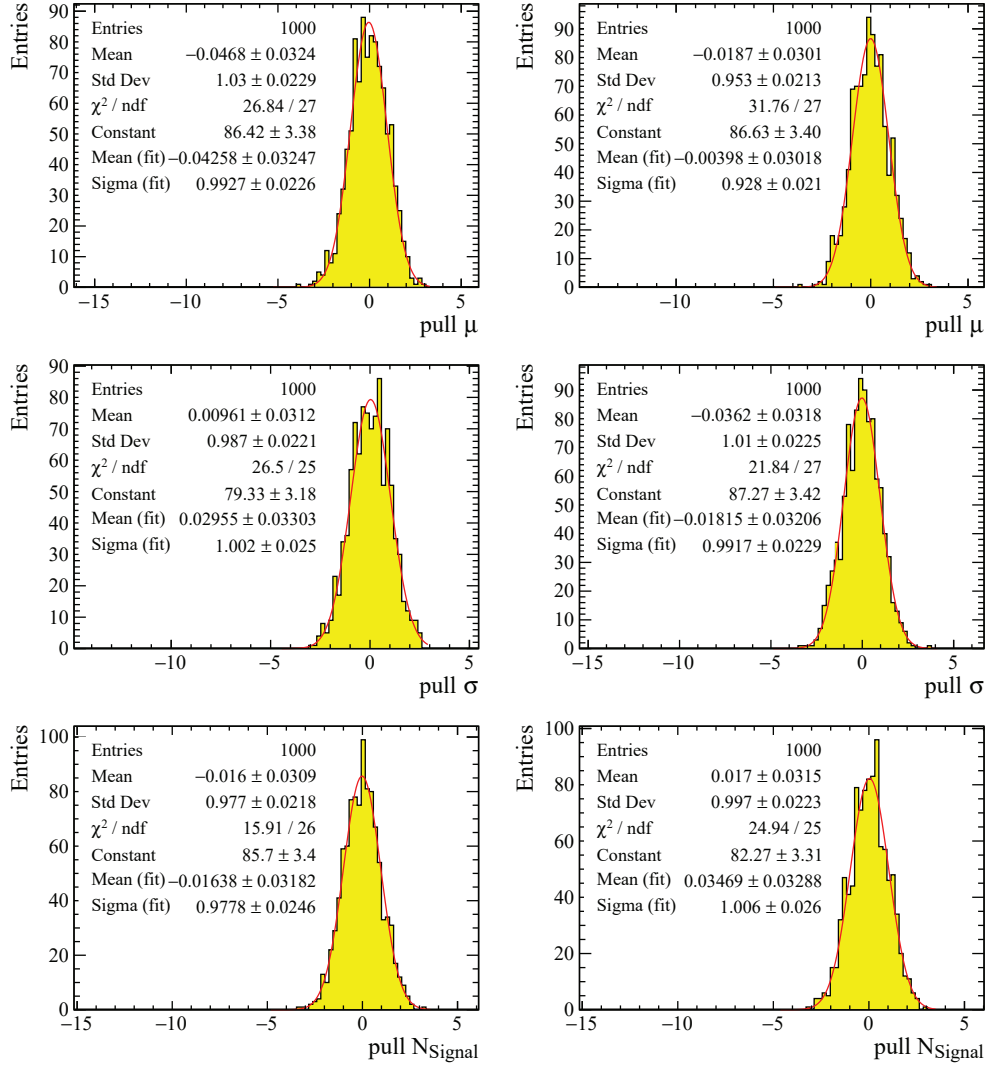


Figure 4.14: The pull distributions of the mean μ and resolution σ of the signal PDFs and the number of signal events N_{Signal} from the generated pseudoeperiment $B^0 \rightarrow K^{*0}\gamma$ (left) and $B_s^0 \rightarrow \phi\gamma$ (right) samples.

Table 4.4: Input values for the decay time fit, from HFAG 2016.

Parameter	Average
$\Delta\Gamma_s$	$0.083 \pm 0.006 \text{ ps}^{-1}$
Γ_s	$0.6643 \pm 0.0020 \text{ ps}^{-1}$
Γ_d	$0.6579 \pm 0.0017 \text{ ps}^{-1}$
$\rho(\Gamma_s, \Delta\Gamma_s)$	-0.239

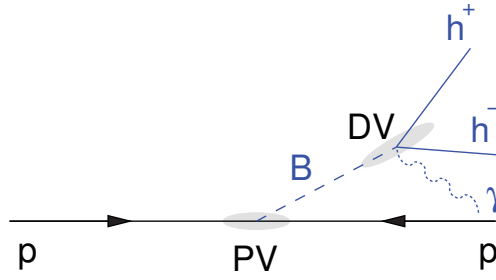


Figure 4.15: Schematic diagram of a $B \rightarrow h^+ h^- \gamma$ decay. The B is produced at the pp collision point (PV) and decays at the vertex (DV) after flying a distance L .

4.5 Determination of A^Δ

The physical decay rate for the untagged $B_s^0 \rightarrow \phi\gamma$ decays can be written as shown in Eq. 4.10a whilst the physical decay rate for $B^0 \rightarrow K^{*0}\gamma$ decays follows a simple exponential function due to the negligible $\Delta\Gamma_d$ value (Eq. 4.10b).

$$\Gamma(B_s^0 \rightarrow \phi\gamma) \propto e^{-\Gamma_s t} \left\{ \cosh \frac{\Delta\Gamma_s t}{2} - A^\Delta \sinh \frac{\Delta\Gamma_s t}{2} \right\}, \quad (4.10a)$$

$$\Gamma(B^0 \rightarrow K^{*0}\gamma) \propto e^{-\Gamma_d t}. \quad (4.10b)$$

The physical parameters used in the simulated signal samples are $\tau_{B_d} = 1.519 \text{ ps}$, $\tau_{B_s} = 1.503 \text{ ps}$, $\Delta\Gamma_s = 0.0917 \text{ ps}^{-1}$ and $A^\Delta = 0$. The latest values from HFAG (Spring 2016) [28] are shown in Table 4.4.

4.5.1 Decay time fitter

The decay time t of a particle is reconstructed using its measured flight distance in the lab frame, L ,

$$t = \frac{L}{\beta\gamma} = L \frac{m}{|\vec{p}|}, \quad (4.11)$$

where \vec{p} is the reconstructed three-momentum of the b -hadron and m is its reconstructed invariant mass. The schematic diagram of a $B \rightarrow h^+ h^- \gamma$ decay is shown in Fig. 4.15. The B meson is produced at the pp collision point (PV) and then decays into two charged hadrons

and a photon at a vertex (DV) after flying a certain distance of L . The particle's flight distance L is measured as the spatial separation of its production point (\vec{x}_{PV}) and its decay vertex (\vec{x}_{DV}) in the laboratory frame.

A kinematical fitter named `PropertimeFitter` is used to directly determine the decay time and its error for a single particle decay, using the information from the reconstructed B candidate and the primary vertex. The fitter takes the decay vertex position \vec{x}_{DV} and the four-momentum $p^\mu = (p_x, p_y, p_z, E)$ of the reconstructed B candidates and the primary vertex position \vec{x}_{PV} as well as their covariance matrices as inputs. The parameters in the fit are defined as $\alpha = (\vec{x}_{\text{PV}}, \vec{x}_{\text{DV}}, \vec{p}, m)$ and their covariance matrix V_α is a 10×10 matrix. The constraints can be written generally as $H(\alpha) = 0$ and expanding around α_0 yields the linearised constraint equation

$$\frac{\partial H(\vec{\alpha})}{\partial \alpha}(\alpha - \alpha_0) + H(\vec{\alpha}_0) = D\delta\alpha + d = 0, \quad (4.12)$$

where D is the derivative of H with respect to α . The constraint condition in the `PropertimeFitter` is $(\vec{x}_{\text{DV}} - \vec{x}_{\text{PV}}) \times \vec{p} = 0$ in the x - y plane which requires the momentum and the B flight distance in the same direction. Using the method of Lagrange multipliers, the constraints can be incorporated in the equation for χ^2 to determine the decay time; the χ^2 is written as

$$\chi^2 = (\alpha - \alpha_0)^T V_{\alpha_0}^{-1} (\alpha - \alpha_0) + 2\lambda^T (D\delta\alpha + d), \quad (4.13)$$

where λ is the Lagrange multiplier, a vector of 3 unknowns. Minimising the χ^2 with respect to α and λ yields two vector equations that can be solved for the parameter α and their covariance matrix. The solution can be written as

$$\lambda = V_D (D\delta\alpha + d), \quad (4.14)$$

$$\alpha = \alpha_0 - V_\alpha D^T \lambda, \quad (4.15)$$

where V_D is defined as $(DV_{\alpha_0} D^T)^{-1}$. Once the fit converges or the maximal iteration is reached, the related observables (\vec{p} , x_{PV} and x_{DV}) and their covariance matrices are updated by introducing another constraint on the reconstructed invariant mass of the B candidate $m = m_{\text{PDG}}$. This fitter is chosen for this analysis due to the straightforwardness in propagating the photon post-calibration into the decay time.

Only charged tracks are used to build the B meson decay vertex \vec{x}_{DV} , where they are constrained to originate at a common vertex. Then, the photon is assumed to be produced at \vec{x}_{DV} and is added to the vertex with its recalculated energy-momentum. Finally, the covariance matrix between the vertex position and the momentum of the mother particle (the B meson) is updated. Thus the contribution from the photon measurement is propagated to the decay time through the B meson energy-momentum and its position-momentum covariance matrix.

The decay time fitter relies on the position-momentum covariance of the B meson. To reduce the size of the data storage, the LHCb data is packed and stored into the $(\mu)\text{DST}$ format [104]

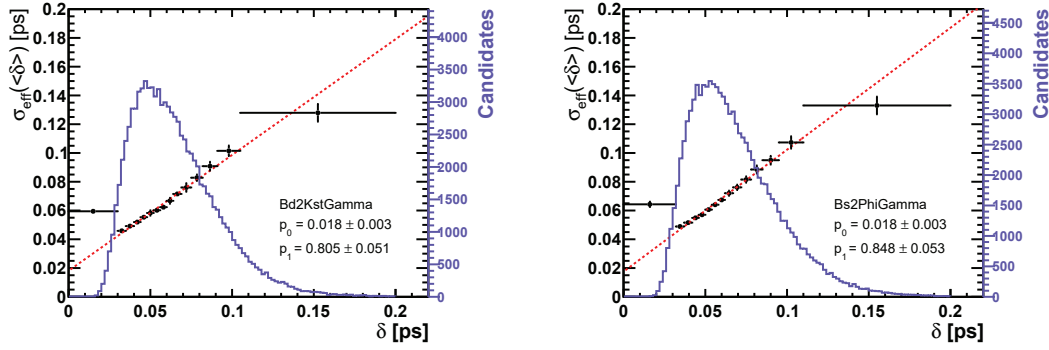


Figure 4.16: The effective B decay time resolution as a function of the per-event resolution in the simulated $B^0 \rightarrow K^{*0}\gamma$ (left) and $B_s^0 \rightarrow \phi\gamma$ (right) samples. The violet histogram is the per-event decay time resolution distribution. The red dotted line is a fit on the data points with a linear function $\sigma_{\text{eff}}(<\delta>) = p_0 + p_1 \cdot <\delta>$.

but due to the rounding in the packing procedure, the positive-definiteness of the position-momentum covariant matrix of the B meson is not preserved correctly at a few percent level [89]. These non-positive-definite covariance matrices result in a failure rate at the 3% level in the decay time fitter and thus affect the reconstructed decay time. To reduce this effect, the position-momentum covariance of the B meson is re-evaluated using the vector meson (ϕ or K^{*0}) covariance and the photon-cluster covariance which are less affected by the packing procedure. This procedure reduces the failure rate of the decay time fit to the level of 0.15%.

4.5.2 Decay time resolution

The uncertainty on the reconstructed decay time is influenced by the resolution of the production and decay vertices, the reconstructed invariant mass and the momentum resolution. The decay time fitter can in principle derive the best estimate of the decay time resolution from the estimated uncertainties of the vertices and the reconstructed momentum. It gives the covariance matrix of the parameters, and thus the error of the decay time, which in this chapter is called the per-event decay time resolution δ . In reality, the reconstructed momentum resolution depends crucially on a good knowledge of hit resolution, material budget, detector alignment and the magnetic field. As a consequence of an imperfect estimation of these quantities, the estimated per-event decay time resolution δ obtained from the fit incorrectly estimates the true decay time resolution σ_t by a factor [105, 106].

The true decay time resolution σ_t is the width of the residual between the reconstructed decay time and the true decay time $\Delta t = t_{\text{rec}} - t_{\text{true}}$. The decay time resolution in each δ bin is fitted with a Double-Gaussian function, where the two gaussians share the same mean *i.e.* the calibration offset. We define an effective decay time resolution $\sigma_{\text{eff}}(<\delta>)$ as the weighted mean of the Gaussian widths² in each δ bin, with a bin centre of $<\delta>$. As shown in Fig. 4.16,

²The decay time resolution in each bin of δ is fitted with a Double-Gaussian function $\sigma_{\text{eff}}(<\delta>) = f \cdot$

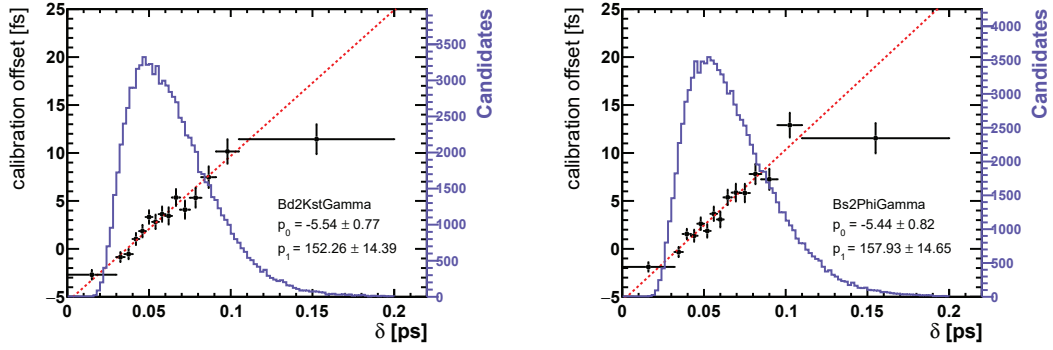


Figure 4.17: The B decay time calibration offset as a function of the per-event resolution in the simulated $B^0 \rightarrow K^{*0}\gamma$ (left) and $B_s^0 \rightarrow \phi\gamma$ (right) samples. The violet histogram is the per-event decay time resolution distribution with the number of candidates shown on the right axis. The red dotted line is a fit on the data points with a linear function $\text{bias}(\langle \delta \rangle) = p_0 + p_1 \cdot \langle \delta \rangle$.

$\sigma_{\text{eff}}(\langle \delta \rangle)$ can be modelled as a linear function of $\langle \delta \rangle$. The decay time fitter overestimates the decay time resolution by about 20% mainly due to the photon momentum reconstruction. The linear dependence of the calibration offset on the per-event decay time resolution is shown in Fig. 4.17.

The decay time resolution is manifested in the measurement of the time-dependent CP violation observables in the B_s^0 decays due to the fast $B_s^0 - \bar{B}_s^0$ oscillations. The decay time resolution affects the measurement of the oscillation amplitude, ϕ_s , where the dilution of the amplitude can be expressed as $\mathcal{D} = \exp(-\sigma_t^2 \Delta m_s^2 / 2)$ [107]. In this analysis, the effect of the resolution on the A^Δ measurement is found to be negligibly small (two orders of magnitude smaller than the statistical uncertainty of the measured A^Δ value).

A modified Apollonios function $\mathcal{R}(\Delta t)$ is used to parametrise the decay time resolution

$$\mathcal{R}(\Delta t; b, \mu, \sigma) = e^{-b\sqrt{1 + \frac{1}{b}\left(\frac{\Delta t - \mu}{\sigma}\right)^2}}, \quad (4.16)$$

where μ is the averaged bias in the decay time range of interest and b and σ are used to describe the width of the distribution. The parameter σ can be interpreted as the Gaussian resolution in the vicinity of the maximum density ($\frac{1}{b}\left(\frac{\Delta t - \mu}{\sigma}\right)^2 \ll 1$). Controlling the calibration offset is an important point in this analysis and it is highly related with the photon momentum evaluation. The introduced post-calibration on the photon momentum can effectively reduce the bias as well as the inhomogeneity in different calorimeter regions. The results of the fit to simulation are shown in Table 4.5, where a small average offset of the order of 3 fs is observed in both channels.

With the selection applied, the decay time resolution is correlated with the decay time accep-

$G(\tau; \mu, \sigma_1) + (1 - f) \cdot G(\tau; \mu, \sigma_2)$ where we define an effective decay time resolution $\sigma_{\text{eff}}(\langle \delta \rangle)$ as $\sigma_{\text{eff}}(\langle \delta \rangle) = \sqrt{f \cdot \sigma_1^2 + (1 - f) \cdot \sigma_2^2}$ in each δ bin and $\langle \delta \rangle$ is the bin centre.

Chapter 4. Study of the photon polarisation in $B_s^0 \rightarrow \phi\gamma$ decays

Table 4.5: Fitted parameters on the events in the decay time range $[0,10]$ ps where μ and σ are the averaged values in this range. Values from Ref. [89].

Parameter	$B^0 \rightarrow K^{*0}\gamma$	$B_s^0 \rightarrow \phi\gamma$
μ (fs)	2.9 ± 0.2	3.3 ± 0.2
σ (fs)	52.6 ± 0.5	45.2 ± 0.6
b	0.90 ± 0.04	0.91 ± 0.04

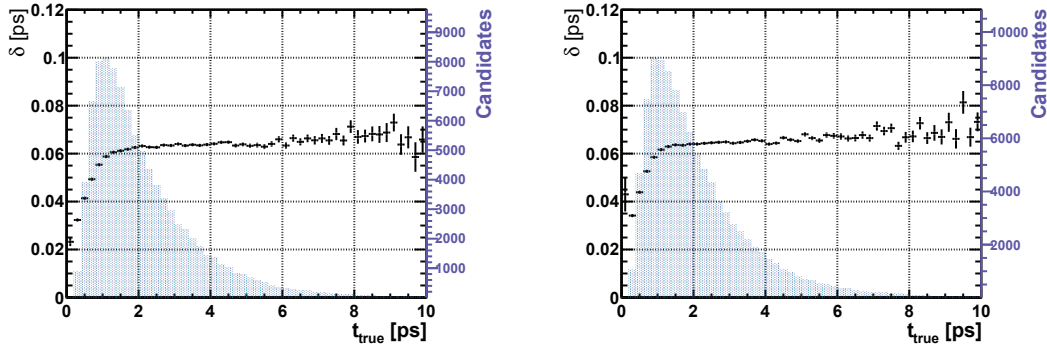


Figure 4.18: The dependence of the B decay time per-event resolution on the decay time in the simulated samples. The violet histogram is the per-event decay time resolution distribution with the number of candidates shown on the right axis.

tance, thus the decay time. In particular, the χ_{IP}^2 cut applied on the vector meson daughters favours the decays with a small uncertainty in the low decay time region. The dependence of the B decay time per-event resolution on the decay time is shown in Fig. 4.18 for both channels in the simulated samples. The evolution of the calibration offset and the resolution parameters, μ and σ , as a function of the decay time is considered. The parameter σ is parametrised with an ad-hoc function

$$\sigma(t; \sigma_0, \tau_0, \beta, n) = \sigma_0 \cdot \frac{(t - \tau_0)^n}{1 + (t - \tau_0)^n} \cdot (1 + \beta t), \quad (4.17)$$

whilst the calibration offset μ can be approximately described with a linear function $\mu(t; \mu_0, k) = \mu_0 + k \cdot t$. The values of the parameters fitted in the simulated samples are reported in Table 4.6.

4.5.3 Decay time acceptance

Decay time inefficiencies come from detector geometry, reconstruction, and the trigger, stripping and offline selections. An excellent understanding of the decay time acceptance is key in measuring A^Δ value in this analysis. The acceptance distributions in simulated samples of $B^0 \rightarrow K^{*0}\gamma$ and $B_s^0 \rightarrow \phi\gamma$ decays shown in Fig. 4.19 as a function of the true decay time are obtained by dividing the distributions of the offline selected from simulation by the true

Table 4.6: The parameters of the functions of both σ and μ fitted in the simulated samples. Values from Ref. [89].

Parameter	$B^0 \rightarrow K^{*0}\gamma$	$B_s^0 \rightarrow \phi\gamma$
σ_0 (fs)	80.0 ± 1.2	85.3 ± 1.0
τ_0 (ps)	0.418 ± 0.001	0.417 ± 0.003
β (ps ⁻¹)	0.02 ± 0.01	0.02 ± 0.01
n	0.22 ± 0.03	0.20 ± 0.03
μ_0 (fs)	-0.4 ± 0.4	0.2 ± 0.4
k (fs/ps)	1.7 ± 0.2	1.6 ± 0.2

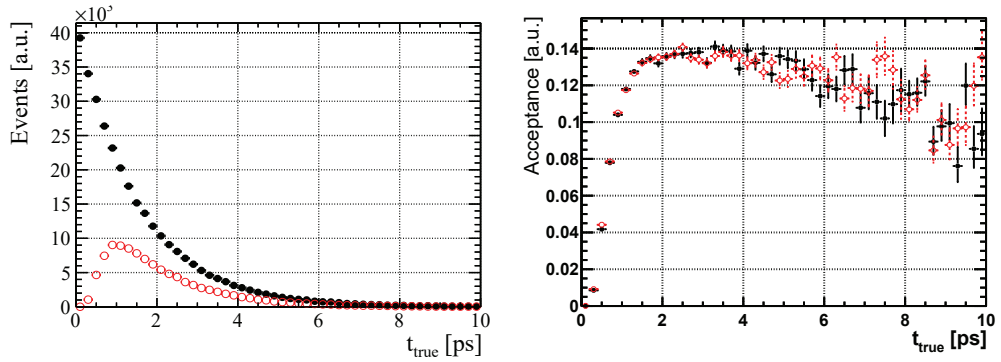


Figure 4.19: The left plot shows the decay time distributions of the true physical decay rate (black full dots) and the offline selected (red open circles) in the simulated $B_s^0 \rightarrow \phi\gamma$ sample whilst the right plot show the decay time acceptances (right) for $B^0 \rightarrow K^{*0}\gamma$ (black full dots) and $B_s^0 \rightarrow \phi\gamma$ (red open circles).

Chapter 4. Study of the photon polarisation in $B_s^0 \rightarrow \phi\gamma$ decays

Table 4.7: Decay time acceptance parameters as fitted on the simulated samples. The parameters t_0 and $\delta\Gamma$ are for the $B^0 \rightarrow K^{*0}\gamma$ channel. The differences between the $B_s^0 \rightarrow \phi\gamma$ channel and the $B^0 \rightarrow K^{*0}\gamma$ channel are defined as $\Delta t_0 \equiv t_0(B_s^0 \rightarrow \phi\gamma) - t_0(B^0 \rightarrow K^{*0}\gamma)$; $\Delta\delta\Gamma \equiv \delta\Gamma(B_s^0 \rightarrow \phi\gamma) - \delta\Gamma(B^0 \rightarrow K^{*0}\gamma)$. Values from Ref. [89].

Parameter	Fitted value	Unit
a	1.87 ± 0.04	ps^{-1}
n	2.23 ± 0.10	
t_0	184 ± 14	fs
$\delta\Gamma$	39.5 ± 3.6	ns^{-1}
Δt_0	-11.7 ± 3.4	fs
$\Delta\delta\Gamma$	-2.3 ± 3.5	ns^{-1}

physical decay time distributions. The function used to model the acceptance is defined as

$$\mathcal{A}(t) = \begin{cases} \frac{[a(t-t_0)]^n}{1+[a(t-t_0)]^n} e^{-\delta\Gamma t} & \text{if } t > t_0 \\ 0 & \text{else} \end{cases}, \quad (4.18)$$

with a , n and t_0 parametrising the lower decay time acceptance and $\delta\Gamma$ describing the upper decay time acceptance.

An unbinned maximum likelihood fit is performed simultaneously on the $B_s^0 \rightarrow \phi\gamma$ and $B^0 \rightarrow K^{*0}\gamma$ decay time distributions from the simulated samples to extract the acceptance parameters. The parameters t_0 and $\delta\Gamma$ are allowed to be different between the two channels. The results of the fitted acceptance parameters are reported in Table 4.7, where Δt_0 and $\Delta\delta\Gamma$ are the difference of the parameters t_0 and $\delta\Gamma$ in the $B_s^0 \rightarrow \phi\gamma$ channel from the $B^0 \rightarrow K^{*0}\gamma$ channel, respectively.

The $\delta\Gamma$ introduced by different reconstruction or selection steps for both $B^0 \rightarrow K^{*0}\gamma$ and $B_s^0 \rightarrow \phi\gamma$ decays are evaluated from the signal simulated samples as shown in Fig. 4.20. The main origins of the upper decay time acceptance are the L0 and the HLT1 trigger requirements. A small difference in the upper decay time acceptance between the signal channel and the control channel is observed. In this analysis, the relative difference in the high decay time acceptances between the two decay channels is controlled using simulated samples.

As the simulated samples do not always reproduce the data perfectly, the absolute size of the estimated $\delta\Gamma$ in simulation can be different from the value in data. To evaluate the effect of using the wrong $\delta\Gamma$ on the measured B^0 lifetime and A^Δ value, decay time fits are performed on the pseudoexperiment samples³ by using the same lower decay time acceptance as for generated samples whilst fixing the $\delta\Gamma$ value to a different value from the generation. The

³Detailed information on the generation of the pseudoexperiment samples is discussed in Section 4.5.7.

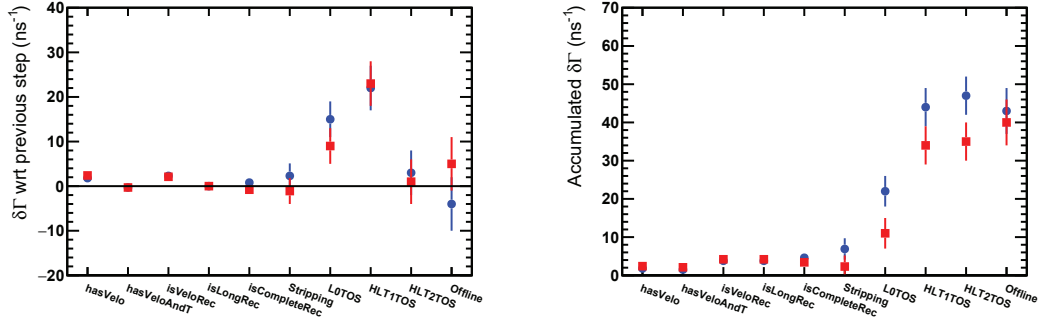


Figure 4.20: High decay time acceptance parameter, $\delta\Gamma$, introduced at each reconstruction or selection step for $B_s^0 \rightarrow \phi\gamma$ (blue circles) and $B^0 \rightarrow K^{*0}\gamma$ (red squares) decays. The bias introduced with respect to the previous step is shown on the left, while the right figure corresponds to the total bias up to a given step. Figures from Ref. [89].

acceptance in the pseudoexperiment samples is introduced as shown in Eq. 4.18 and the input parameters are taken from Table 4.7. Each pseudoexperiment sample is generated with about 100k signal-only events. The measured B^0 lifetime can be written as

$$\tau^{\text{fit}} = \frac{1}{\Gamma_d - \Delta} = \tau^{\text{true}} \cdot \sum_{n=0}^{\infty} \left(\frac{\Delta}{\Gamma_d} \right)^n, \quad (4.19)$$

where Δ is the $\delta\Gamma$ value difference between the value fixed in the fit and the input value in the sample generation $\Delta \equiv \delta\Gamma^{\text{fix}} - \delta\Gamma^{\text{true}}$ and the true B^0 lifetime $\tau^{\text{true}} = 1/\Gamma_d$. Then, the bias on the measured B^0 lifetime is approximately Δ/Γ_d^2 because of $\Delta/\Gamma_d \ll 1$. Figure 4.21 shows the bias of the fitted B^0 lifetime and A^Δ value as a function of the Δ . The results show that the effect of a misestimated $\delta\Gamma$ value is more significant on the A^Δ measurement than the B^0 lifetime and it depends on the true A^Δ value, where the bias on the measured A^Δ value decreases as the true value of A^Δ increases. No change to this conclusion is observed in the absence of the decay time resolution. The same procedure can be performed on simulated signal $B^0 \rightarrow K^{*0}\gamma$ and $B_s^0 \rightarrow \phi\gamma$ decays, and the results are shown in Fig. 4.21 for a comparison with the pseudoexperiment results.

4.5.4 Decay time fit procedure

In this analysis, the PDF used to fit the decay time is defined as

$$\mathcal{P}(t_{\text{rec}}) = \int_{-\infty}^{+\infty} \Gamma(t_{\text{true}}) \times \mathcal{A}(t_{\text{true}}) \times \mathcal{R}(t_{\text{rec}} - t_{\text{true}}; \mu, \sigma) dt_{\text{true}}, \quad (4.20)$$

where $\Gamma(t_{\text{true}})$ represents the physical decay rate, $\mathcal{A}(t_{\text{true}})$ the acceptance on the true decay time and $\mathcal{R}(t_{\text{rec}} - t_{\text{true}}; \mu, \sigma)$ is the time-dependent resolution with μ and σ as a function of t_{true} .

Each event in the data samples is given a signal weight, W_i , using the *sPlot* method [108] with

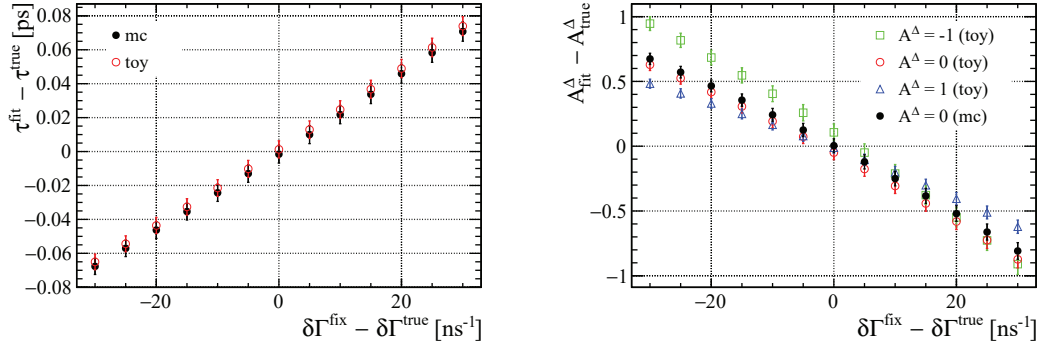


Figure 4.21: The fitted B^0 lifetime (left) and A^Δ value (right) as a function of the $\delta\Gamma$ value misestimation $\delta\Gamma_{\text{fix}} - \delta\Gamma_{\text{true}}$. The pseudoexperiment samples used on the right plot are with different input A^Δ values: -1 (green squares), 0 (red circles) and 1 (blue triangles). The black dots represent the simulated signal $B^0 \rightarrow K^{*0}\gamma$ (left) and $B_s^0 \rightarrow \phi\gamma$ (right) samples.

the reconstructed B invariant mass used as a discriminating variable. A weighted fit [109] is performed using a signal-only PDF, denoted by \mathcal{S} , on the data samples with signal weight assigned by the *sPlot* method which will henceforth be referred to as the background subtracted data sample. To better estimate the uncertainties on the fitted parameters in the presence of the weights, the log-likelihood functions are scaled by $\alpha = \sum_{i=1}^N W_i / \sum_{i=1}^N W_i^2$ where N is the number of events in the sample⁴. The joint negative log-likelihood, \mathcal{L} , constructed as

$$-\ln\mathcal{L} = -\alpha \sum_i W_i \ln\mathcal{S}, \quad (4.21)$$

is minimised in the fit. To determine the A^Δ value, a simultaneous unbinned maximum likelihood fit is performed on the decay time distributions of the data samples and the simulated signal samples. The $B_s^0 \rightarrow \phi\gamma$ decay time acceptance is constrained by the control channel $B^0 \rightarrow K^{*0}\gamma$, which is six times larger in statistics and with a physics decay rate as a simple exponential function. The simulated $B_s^0 \rightarrow \phi\gamma$ and $B^0 \rightarrow K^{*0}\gamma$ signal samples are used to account for potential differences between the signal and control channels in the decay time acceptance.

An alternative strategy to extract the A^Δ parameter is to perform a binned minimum χ^2 fit on the ratio of the decay time distributions between $B_s^0 \rightarrow \phi\gamma$ and $B^0 \rightarrow K^{*0}\gamma$ in the data samples, with signal weights considered when calculating the ratio in each bin and an event-by-event correction of the calibration offset applied. Furthermore, an adaptive binning scheme is adopted by maximising the sensitivity of the fitted A^Δ value using signal-only pseudoexperiment samples. Due to the negligible impact of the resolution on the B^0 lifetime and A^Δ value measurement, the resolution is not considered in this procedure. This alternative approach is found to have the same sensitivity as the nominal time fit procedure by the pseudoexperiment studies.

⁴The scaling only happens for the determination of the uncertainties of the fit parameters whilst the minimisation of the negative log-likelihood $-2\ln\mathcal{L}$ is still determined without the scale factor.

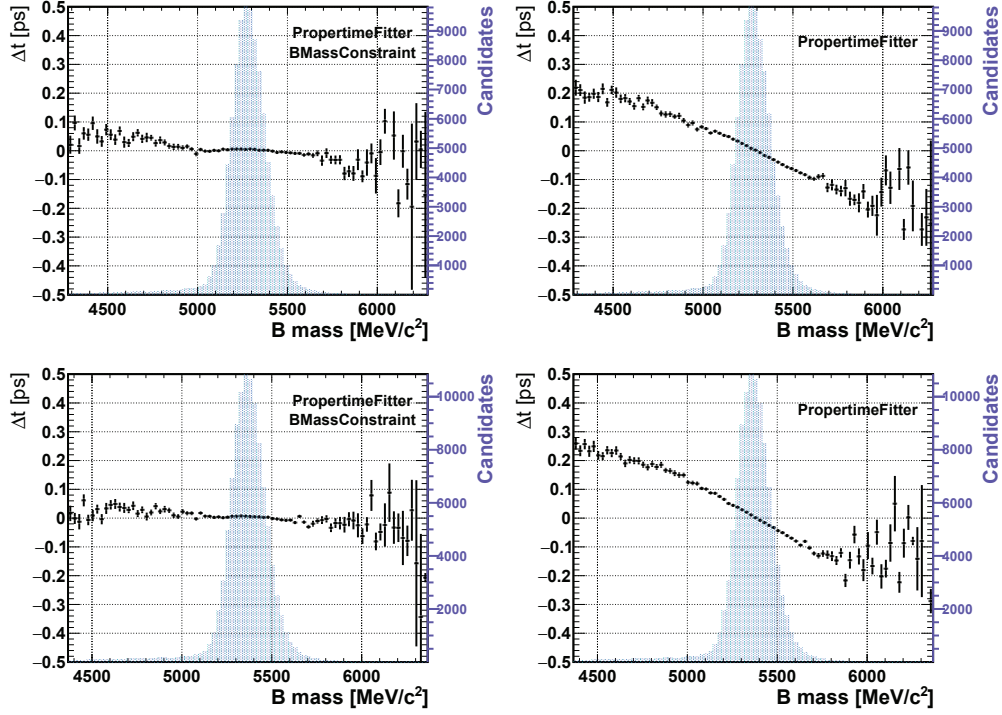


Figure 4.22: Dependence of the reconstructed B decay time on its reconstructed mass in the simulated signal samples $B^0 \rightarrow K^{*0}\gamma$ (top) and $B_s^0 \rightarrow \phi\gamma$ (bottom). The decay time reconstructed with the constraint on the B invariant mass is shown on the left whilst the one without the constraint is on the right. The violet shaded histogram represents the reconstructed B mass distribution with the number of candidates shown on the right axis.

4.5.5 The dependence of the B decay time on its mass

An essential assumption built into the $sPlot$ technique is that the control variables are uncorrelated with the discriminating variables. The decay time obtained with the constraint on the B mass is chosen because of a negligible dependence on the reconstructed B mass; compared to the distributions without the B mass constraint, shown in Fig. 4.22 for the simulated signal samples. The figures show the dependence of the reconstructed decay time subtracted by the true decay time $\Delta t = t_{\text{rec}} - t_{\text{true}}$ on the reconstructed B mass. The decay time without a constraint on the B mass is shown to be highly correlated with the reconstructed B invariant mass.

4.5.6 The B^0 lifetime measurement

A simultaneous unbinned maximum likelihood fit on the background subtracted data sample of $B^0 \rightarrow K^{*0}\gamma$ and the corresponding simulated sample is performed to extract the B^0 lifetime by assuming that the simulation reproduces the acceptance in data. The fitted B^0 lifetime value is 1.524 ± 0.013 ps [89], where the uncertainty is purely statistical. This result is consistent

with the latest HFAG value (Spring 2016) of 1.520 ± 0.004 ps.

Assuming that the acceptance function is well controlled at lower decay times, the maximum misestimation of the acceptance at high decay times should be below 5 ns^{-1} , according to the pseudoexperiment study shown in Fig. 4.21. The 5 ns^{-1} misestimation of the higher decay time acceptance could result in a bias in the measured A^Δ value in the range of -0.2 and $+0.3$, which is smaller than the statistical and systematic uncertainties.

4.5.7 Validation of the fit procedure

Large samples of pseudoexperiment events are generated to validate the full procedure of the A^Δ determination, including the B invariant mass fits, the *sPlot* method and the decay time fits. The procedure as discussed in Section 4.4.3 is used to generate the B mass distributions and perform the mass fits. The procedure to generate the decay time distributions for the signal and control channels is described below:

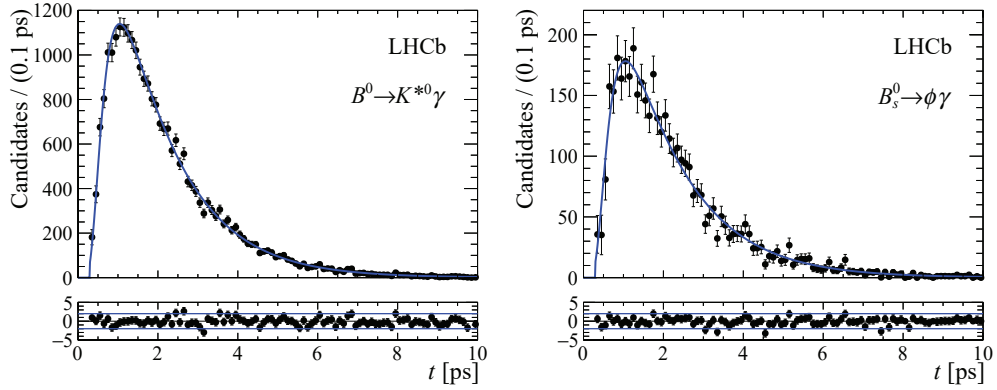
1. The true decay time t_{true} distribution is generated according to the defined PDF $\Gamma(t_{\text{true}}) \cdot \mathcal{A}(t_{\text{true}})$ with the number of events sampled from a Poisson distribution;
2. The resolution $\Delta t = t_{\text{rec}} - t_{\text{true}}$ of each event is generated from the conditional model $\mathcal{R}(\Delta t | t_{\text{true}})$ with t_{true} value taken from previous step;
3. The decay time t_{rec} of the event then equals $t_{\text{true}} + \Delta t$.

The parameters for the physical decay rate $\Gamma(t_{\text{true}})$ are fixed to the HFAG values in Table 4.4. The acceptance parameters of $\mathcal{A}(t_{\text{true}})$ and the resolution parameters of $\mathcal{R}(\Delta t | t_{\text{true}})$ are from the fits in simulated samples as shown in Table 4.6 and Table 4.7, respectively. For the background components (apart from the combinatorial backgrounds), model parameters of each decay time distribution are extracted from the corresponding simulated background samples without considering the resolution. The model parameters for the combinatorial background are extracted from fits on the combinatorial background samples extracted using *sPlot* from the data samples. A thousand pseudoexperiment samples for each A^Δ value amongst -1.0 , -0.5 , 0.0 , 0.5 and 1.0 are generated.

The decay time fit procedure designed to determine the A^Δ value in Section 4.5.4 is performed on the pseudoexperiment samples. The mean and sigma of the pull distributions on fitted A^Δ values for the five sets of signal-only pseudoexperiment samples and the samples with the full procedure applied are shown in Table 4.8. There is no offset of the fitted A^Δ values observed, but a small underestimation of the uncertainties at a few percent level is observed which is corrected for the final result using ten thousand pseudoexperiments generated at the central value of the fitted A^Δ .

Table 4.8: The mean μ of Gaussian fits to the distributions of the fitted A^Δ values and sigma σ of Gaussian fits to the pull distributions for the 5 sets of pseudoexperiment samples.

A_{true}^Δ	Signal-only		Full procedure	
	$\mu(A_{\text{fit}}^\Delta - A_{\text{true}}^\Delta)$	$\sigma(\text{Pull})$	$\mu(A_{\text{fit}}^\Delta - A_{\text{true}}^\Delta)$	$\sigma(\text{Pull})$
-1	0.01 ± 0.01	1.04 ± 0.03	0.02 ± 0.02	1.09 ± 0.03
-0.5	0.02 ± 0.01	1.00 ± 0.02	0.01 ± 0.01	1.04 ± 0.02
0	0.00 ± 0.01	0.99 ± 0.02	0.00 ± 0.01	1.01 ± 0.03
0.5	0.00 ± 0.01	0.98 ± 0.02	-0.01 ± 0.01	1.04 ± 0.03
1	0.01 ± 0.01	1.04 ± 0.03	-0.01 ± 0.01	1.07 ± 0.03


 Figure 4.23: The decay time distributions in the background subtracted data samples for $B^0 \rightarrow K^{*0}\gamma$ (left) and $B_s^0 \rightarrow \phi\gamma$ (right) decays with the fit overlaid. Figures from Ref. [110].

4.5.8 Measurement of the A^Δ value

The $B^0 \rightarrow K^{*0}\gamma$ and $B_s^0 \rightarrow \phi\gamma$ decay time distributions from data samples are presented in Fig. 4.23. The fitted value of the A^Δ parameter is $-0.98^{+0.46}_{-0.52}$ where the uncertainty includes the statistical effects and the contribution coming from the physics parameters τ_{B^0} , Γ_s and $\Delta\Gamma_s$. Fixing the latter to their central values, their contribution is estimated to account for $^{+0.10}_{-0.17}$.

The measured decay time ratio of the two decay channels is presented in Fig. 4.24 with the fit result overlaid to the data points. The expectation for the SM value of A^Δ is shown on the plot for comparison. The result on A^Δ from the fit on the ratios is $-0.85^{+0.41}_{-0.44}$. A event-by-event comparison between the two fitting procedures using the pseudoexperiment samples shows that the statistical difference between the two procedures and the statistical uncertainty are true A^Δ value dependent. The RMS values of the distributions of the difference in fitted A^Δ values between the baseline fit and the fit on ratios are ranging from 0.08 at true A^Δ value 1.0 up to 0.14 at true A^Δ value -1.0 . As a consequence, the difference of the result obtained from the fit of the ratios with respect to the baseline fit, which accounts to 0.13, is compatible with expectation.

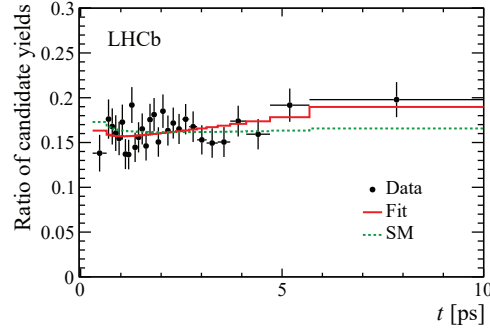


Figure 4.24: The decay time ratio between $B_s^0 \rightarrow \phi\gamma$ and $B^0 \rightarrow K^{*0}\gamma$ (data points) with the fit (solid red line) and the expectation for the SM value of A^Δ (green dashed line) overlaid. Figure from Ref. [110].

Table 4.9: List of systematic uncertainties on A^Δ .

Source	Uncertainty
Decay time acceptance	+0.13 -0.05
External parameters	+0.10 -0.17
Decay time resolution	± 0.009
Signal mass shape	± 0.032
Combinatorial background shape	± 0.074
Peaking background contributions	+0.02 -0.05
Partially reconstructed background shape	± 0.096
Correlation between mass and decay time	± 0.15
Quadratic sum	+0.23 -0.20

4.6 Systematic uncertainties

The major contributions to the systematic uncertainty from the external parameters, the decay time acceptance, the modelling of the B invariant mass distributions and the correlation between the B mass and decay time are evaluated in the following sections and summarised in the Table 4.9. Accounting for the decay time acceptance uncertainty in the systematic uncertainty budget and keeping the uncertainty on the external parameters in the statistical uncertainty budget, one gets an overall systematic uncertainty of $^{+0.23}_{-0.20}$.

Few percent-level asymmetry in the relative magnitudes of the B_s^0 and \bar{B}_s^0 production rates [111] is found to have a negligible effect on the A^Δ measurement based on a pseudoexperiment study.

To evaluate the systematic uncertainty related to the decay time resolution, the parameters of the decay time resolution PDF are varied according to the statistical uncertainties. The systematic uncertainty related to the decay time resolution is found to be ± 0.009 .

No systematic uncertainty is assigned for the photon momentum calibration because the photon momentum calibration is directly translated into the decay time resolution, where the reconstructed B momentum is dominated by the photon momentum.

4.6.1 External parameters

The physics parameters τ_{B^0} , Γ_s , and $\Delta\Gamma_s$ are constrained to the averages listed in Table 4.4. The correlation between the uncertainties on Γ_s and $\Delta\Gamma_s$ is accounted for. The contribution coming from the uncertainty on the physics parameters τ_{B^0} , Γ_s and $\Delta\Gamma_s$ is estimated to be $^{+0.10}_{-0.17}$, which is included in the statistical uncertainty in the final reported result.

4.6.2 Decay time acceptance

Systematic uncertainties from the decay time acceptance could originate from two sources. The main uncertainty related to the decay time acceptance is associated to the simulated sample statistics and is found to be $^{+0.13}_{-0.05}$. The decay time acceptance parametrisation is another possible source of uncertainty. An alternative upper decay time acceptance parametrised as $1/\cosh(\delta\Gamma t)$ instead of the $\exp(-\delta\Gamma t)$ is tested with no effect on the result. Its contribution is thus ignored.

4.6.3 Models of the B mass distributions

The systematic uncertainty related to the signal lineshape is evaluated by using an alternative parametrisation of a double-tail asymmetric Apollonios function [112]; a shift of -0.032 in the fitted A^Δ value from the nominal value is observed.

The systematic uncertainties related to the partially reconstructed background mass shapes are evaluated using alternative parametrisations on simulated samples of decays via different decay paths but with the same final state. The missing pion background in $B^0 \rightarrow K^{*0}\gamma$ decay is modelled using the model obtained by fitting the simulated $B \rightarrow K_1(1270)(K^{*0}\pi)\gamma$ sample in the nominal mass fit. As an alternative, the simulated $B \rightarrow K^*(1410)(K^{*0}\pi)\gamma$ sample is used to estimate the systematic uncertainty. This leads to a shift of the fitted A^Δ value of -0.036 . A simulated $B^+ \rightarrow K_1(1270)^+(K^{*0}\pi^+)\eta$ sample is used to estimate the systematic contribution due to the modelling of the very low mass background of $B \rightarrow K\pi\pi^0 X$; the resulting shift for the fitted A^Δ value from the nominal fit is -0.055 . For the missing kaon background for $B_s^0 \rightarrow \phi\gamma$ decays, simulated $B_s^0 \rightarrow \phi K_s^0\gamma$ decays are used. The shift of the fitted A^Δ value is $+0.069$, comparing to the nominal fitted value using the simulated $B^+ \rightarrow \phi K^+\gamma$ sample. The background $B^0 \rightarrow K^{*0}\eta$ contributes to the signal region of the $B^0 \rightarrow K^{*0}\gamma$ decay. Both the shape and normalisation are fixed in the nominal mass fit and the $sPlot$ technique is modified to deal with this contribution. To evaluate the related systematic uncertainty, the $B^0 \rightarrow K^{*0}\gamma$ mass fit is performed without this component and the standard $sPlot$ technique is used for background subtraction. The fitted A^Δ value is found to be shifted by -0.008 from the

nominal fitted value. The four contributions are summed in quadrature leading to a systematic uncertainty of ± 0.096 .

As an alternative procedure, the parameters of the signal and all the partially reconstructed background models are varied within the uncertainties from the simulated samples those used to extract these parameters. The mass fits are repeated a thousand times for each component to evaluate the shifts from the nominal value. The results from this procedure are all smaller than the nominal procedure.

The contribution from the combinatorial background modelling is estimated using an exponential function instead of the first order polynomial function in the mass fits performed on the data samples. A shift of the A^Δ value by $+0.074$ is observed.

4.6.4 Peaking background contribution

To evaluate the systematic uncertainty related to the peaking backgrounds, pseudoexperiment samples are generated using the same procedure as in Section 4.5.7 for different contributions of the peaking backgrounds:

- no contribution of the peaking backgrounds generated;
- the contribution of the peaking backgrounds increased by 1 standard deviation respect to the uncertainties on their contributions;
- the contribution of the peaking backgrounds increased by 3 standard deviations respect to the uncertainties on their contributions.

Different A^Δ values of -1.0 , 0.0 and 1.0 are used in the pseudoexperiment samples and a dependence of the systematic contribution on the A^Δ value is observed. The systematic uncertainty is found to be at maximal $^{+0.02}_{-0.05}$ for $A^\Delta = -1$.

4.6.5 Correlation between B mass and decay time

Since the $sPlot$ technique is used to subtract the partially reconstructed and combinatorial backgrounds, the effect due to the correlation between the B mass and the decay time in these backgrounds needs to be considered in the systematic uncertainty evaluation for the determination of A^Δ .

The dependences of the decay time on the reconstructed B mass in two simulated background samples of the $B \rightarrow K^{*0}\pi\gamma$ and $B^+ \rightarrow \phi K^+\gamma$ decays are shown in Fig. 4.25, with the former reconstructed as $K^{*0}\gamma$ and the later as $\phi\gamma$.

To evaluate the systematic uncertainty contribution from potential correlations between the reconstructed mass and decay time in backgrounds from partially reconstructed B decays, pseudoexperiment samples are generated with the correlation included. Kernel estimation [113] is used to provide the PDF estimation from the two-dimensional (2D) datasets containing the

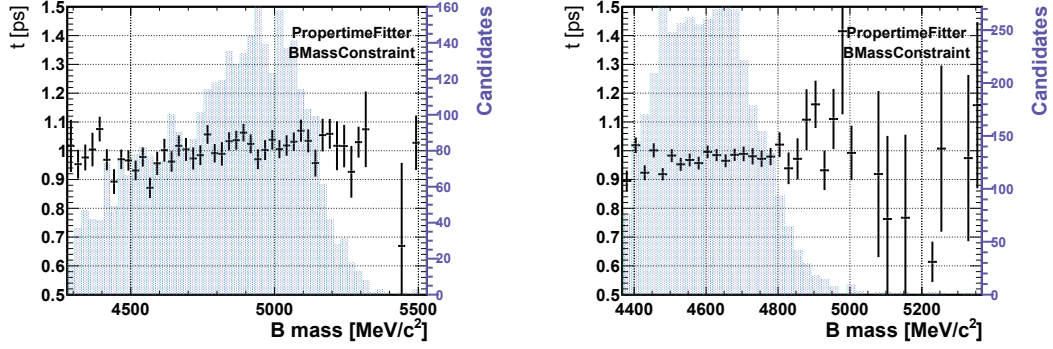


Figure 4.25: Dependence of the B decay time on its mass in the simulated background samples of $B \rightarrow K^{*0}\pi\gamma$ reconstructed as $K^{*0}\gamma$ (left) and $B^+ \rightarrow \phi K^+\gamma$ reconstructed as $\phi\gamma$ (right). The violet shaded histogram represents the reconstructed B mass distribution.

mass and decay time from the simulated samples. The pseudoexperiments are generated with the two-dimensional PDF $\mathcal{P}(m, t)$ and the projection of this PDF on mass is used to fit the mass distribution and perform $sPlot$ for background subtraction. Pseudo-experiments with different configurations at A^Δ values of -1.0 , 0.0 and 1.00 are generated:

- correlation only introduced in the missing pion background of $B^0 \rightarrow K^{*0}\gamma$ decay channel;
- correlation only introduced in the missing kaon background of $B_s^0 \rightarrow \phi\gamma$ decay channel;
- correlation introduced in all the partially reconstructed background of $B^0 \rightarrow K^{*0}\gamma$ and $B_s^0 \rightarrow \phi\gamma$ decay channels.

The dependence of the estimated shifts in the fitted A^Δ values is observed and the effect is largest at $A^\Delta = -1$. The dominant contribution is from the correlation introduced in the missing pion background of $B^0 \rightarrow K^{*0}\gamma$ decay channel, which results in a non-negligible contribution to the signal region. The systematic uncertainty is estimated to be ± 0.15 .

Figure 4.26 show the dependence of the decay time on its mass of the combinatorial backgrounds in the upper sideband of $[m_B + 500, m_B + 1000] \text{ MeV}/c^2$ where m_B is the B^0 or B_s^0 mass. No correlation between the decay time and the B mass is expected and observed for the combinatorics, thus, no correlation systematics need to be assigned for the combinatorial background.

4.7 Conclusion

The photon polarisation parameter A^Δ in the $B_s^0 \rightarrow \phi\gamma$ decay is measured with 3 fb^{-1} data collected at the LHCb experiment by performing an untagged time-dependent analysis. The number of signal candidates determined from the B invariant mass fit is 4214 ± 90 , where the uncertainty is purely statistical, with the contribution from peaking backgrounds (142 ± 67 events) included. The decay time acceptance function is controlled using a $B^0 \rightarrow K^{*0}\gamma$ sample

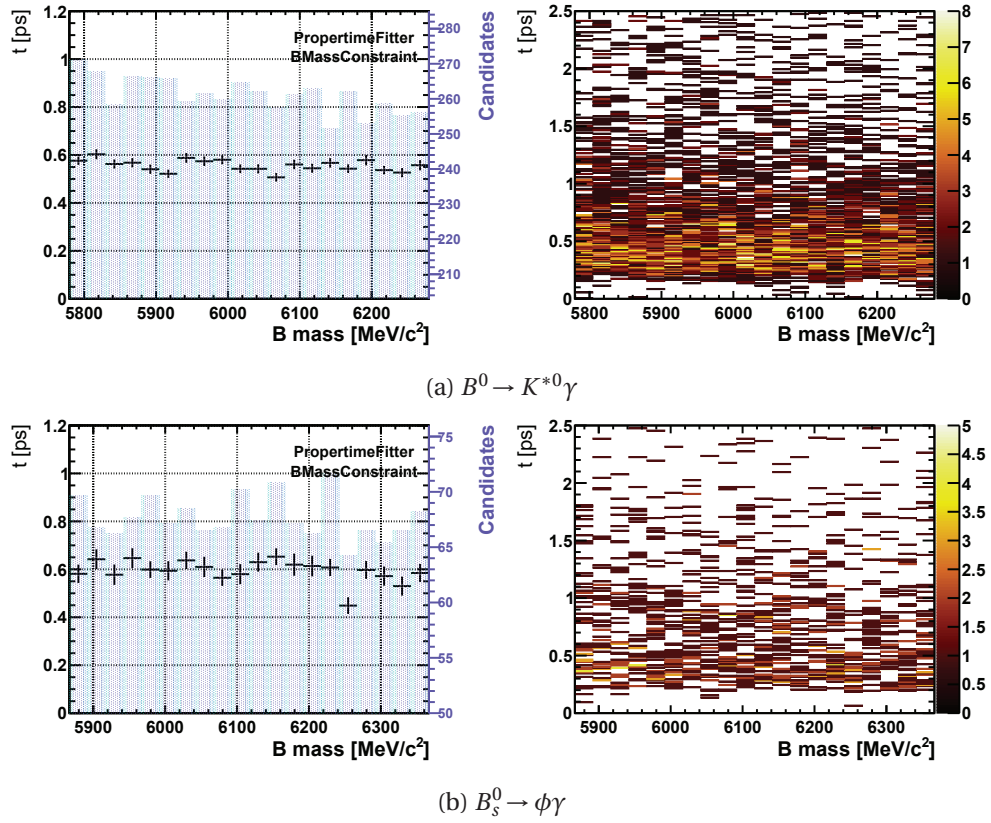


Figure 4.26: Dependence of the B decay time on its mass in the upper sideband of the B invariant mass region. The violet shaded histogram represents the reconstructed B mass distribution.

with statistics six times larger than the signal channel. An unbinned simultaneous fit to the $B_s^0 \rightarrow \phi\gamma$ and $B^0 \rightarrow K^{*0}\gamma$ data samples is performed. The A^Δ value, which is sensitive to the anomalous polarisation of the photon, is measured to be:

$$A^\Delta = -0.98^{+0.46}_{-0.52}(\text{stat.})^{+0.23}_{-0.20}(\text{syst.}). \quad (4.22)$$

This result is compatible with the SM expectation, $A^\Delta_{\text{SM}} = 0.047^{+0.029}_{-0.025}$ [35], within two standard deviations.

5 CP violation in $B^+ \rightarrow \phi K^+ \gamma$ decays

The photon polarisation parameter λ_γ can be extracted from the angular distribution of the hadronic final state particles in $B^+ \rightarrow \phi K^+ \gamma$ decays, as discussed in Chapter 1. This work is a feasibility study of measuring the photon polarisation in the decay of $B^+ \rightarrow \phi K^+ \gamma$, using the large statistics of the LHCb data sample. Theoretical studies in Ref. [22] pointed out that the photon polarisation can be measured in the $B^+ \rightarrow \phi K^+ \gamma$ decay from the final state angular distributions only in the presence of the strong interference between the partial waves in the ϕK^+ -system, with the later as a vector state. But so far, there are no studies confirming the existence of the vector states in the ϕK^+ -system. Thus, the first step of this work is to perform a detailed study of the hadronic structure of the ϕK^+ -system, which would ultimately led to a photon polarisation measurement in this decay mode if vector states are observed in the ϕK^+ -system. Afterwards, the detailed strategy on extraction of the parameter λ_γ from the angular distributions both theoretically and experimentally is discussed. In addition, the direct CP asymmetry is measured with a better precision than the previous measurements performed by the Belle [40] and BaBar [114] collaborations due to the larger statistics at LHCb.

5.1 Event reconstruction and selection

This analysis uses the full dataset corresponding to an integrated luminosity of 3 fb^{-1} collected with the LHCb detector during Run I. Simulated samples are used to optimise the selections, estimate the efficiencies and perform background studies. A simulated sample of about 3 million events $B^+ \rightarrow \phi K^+ \gamma$ decays is generated with the ϕK^+ -system as a vector state with the spin-parity $J^P = 1^-$, a mass of $1.8 \text{ GeV}/c^2$ and a width of $496.89 \text{ MeV}/c^2$. A simulated sample of about 6 million events $B^+ \rightarrow K^+ K^+ K^- \gamma$ decays is generated with $K^+ K^+ K^-$ -system of the invariant mass uniformly distributed between $1.45 \text{ GeV}/c^2$ and $5.0 \text{ GeV}/c^2$, with spin-parity of $J^P = 1^-$ and decaying using a PHSP model [68]. Simulated samples of $B^+ \rightarrow \phi K^{*+}$, $B^+ \rightarrow \phi K_2^*(1430)^+$ and $B^+ \rightarrow \phi K^*(1680)^+$ decays are generated with the kaonic resonances decaying into $K^+ \pi^0$ final state for studies of the background contributions from merged π^0 s.

The trigger and selections discussed in the following sections are optimised for B^+ mesons

decaying into the $K^+ K^+ K^- \gamma$ final state.

5.1.1 Trigger

The L0 and HLT1 trigger selections for this decay are identical to that for the $B_s^0 \rightarrow \phi \gamma$ decays described in Chapter 4. The following HLT2 trigger lines [90] are combined to maximise the selection efficiency of the signal $B^+ \rightarrow K^+ K^+ K^- \gamma$ candidates:

- the regular multivariate-based (BBDT) topological lines `Hlt2Topo[2,3,4]BodyBBDT`, which are designed to trigger efficiently on any B decays with two or more charged particles in the decay;
- the radiative multivariate-based topological lines `Hlt2TopoRad[2,2plus1]BodyBBDT`, which combine the charged tracks with photon candidates;
- and the radiative cut-based topological lines `Hlt2RadiativeTopo[Track,Photon]`, which select candidates of 2 charged particles and a high- E_T photon candidate combinations.

5.1.2 STRIPPING and offline selection

The STRIPPING line used for the selection of $B^+ \rightarrow K^+ K^+ K^- \gamma$ candidates selects all possible decays of a B meson to three charged tracks and a high- E_T photon. Selections applied in the STRIPPING line are documented in Table A.3. All the charged tracks are assigned the pion mass hypothesis (without PID requirements) which need to be substituted with kaon mass hypothesis to reconstruct $B^+ \rightarrow K^+ K^+ K^- \gamma$ candidates.

The candidate events are further refined by imposing a set of tighter cuts at the offline stage. The maximum transverse momentum of the charged tracks is required to be larger than $1.2 \text{ GeV}/c$ whilst the minimum is greater than $0.5 \text{ GeV}/c$. The photons are selected with E_T greater than 3 GeV and $CL > 0.25$, where CL is the confidence level of a photon candidate to be a true photon, built from combining information from the calorimetric and tracking systems, thus rejecting hadrons and electrons. The reconstructed B candidates are required to have $p_T > 5 \text{ GeV}/c$.

Vertex isolation is used to remove partially reconstructed B^+ candidates in which at least one charged particle in the event is not associated to this decay. The idea is to add the extra tracks other than the selected tracks to build the B^+ candidate in the event, one by one, and then compute the $\Delta\chi_{\text{one track}}^2$ which is the difference between the original B^+ candidate vertex χ^2 and the new vertex χ^2 when adding one extra track. The smallest $\Delta\chi_{\text{one track}}^2$ is used as the isolation variable. In the case of the existence of extra tracks, a criterion of $\Delta\chi_{\text{one track}}^2 > 2$ is required.

The left-right symmetry of the LHCb detector is broken by the magnetic field [115], which bends positive and negative particle in opposite directions. A model of the magnetic field

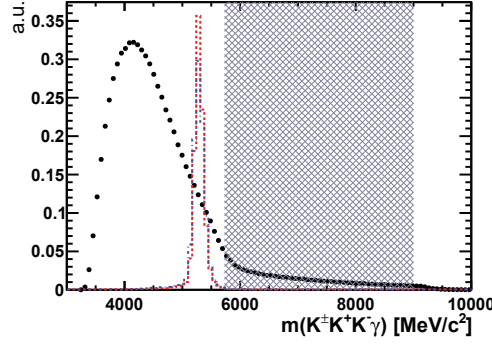


Figure 5.1: The $K^+ K^+ K^- \gamma$ invariant mass distributions of the real data (black dots) and of the simulated $B^+ \rightarrow \phi K^+ \gamma$ (blue dashed line) and $B^+ \rightarrow K^+ K^+ K^- \gamma$ (red dashed line) samples. The grey shaded box indicates the upper sideband range for background study.

used to calculate the acceptance boundary introduces the fiducial cut $|p_X| \leq 0.317(p_Z - 2400) \text{ MeV}/c$. These fiducial requirements are imposed to exclude kinematic regions having a large asymmetry in the soft track reconstruction efficiency.

5.1.3 Boosted decision tree

A boosted decision tree (BDT) [116] is implemented to separate the signal decays from the combinatorial background. Adaptive boosting (AdaBoost) is employed for the BDT based on the Scikit-learn algorithm [117]. The classifier is trained and tested using the simulated $B^+ \rightarrow K^+ K^+ K^- \gamma$ sample to represent the signal and the upper sideband of the B^+ mass distribution in data for the combinatorial background candidates. The upper sideband of the B^+ mass is defined in the range of $[m_{B^+} + 450, 9000] \text{ MeV}/c^2$ which is indicated by the grey shaded box in Fig. 5.1, where m_{B^+} is the B^+ mass [39]. A total of 39910 signal candidates is selected in the simulated $B^+ \rightarrow K^+ K^+ K^- \gamma$ sample and a sample of 50000 background events is randomly selected in the defined upper sideband region of the real data. The full sample is split into three sub-samples for training, optimisation and performance test of the classifier.

Two categories of properties associated with the charged tracks for the B^+ decays and the B^+ candidates are used as discriminating variables:

- Charged tracks:
 - χ^2 per degree of freedom in the track fit ($\chi^2_{\text{track}}/\text{ndf}$),
 - the significance of the impact parameter of the track respect to the primary vertex (χ^2_{IP});
- B candidates:
 - transverse momentum (p_T),
 - flight distance from the primary vertex (FD),
 - the χ^2 separation of a vertex from its associated primary vertex (χ^2_{FD}),
 - χ^2 per degree of freedom in the B^+ vertex fit ($\chi^2_{\text{vtx}}/\text{ndf}$),

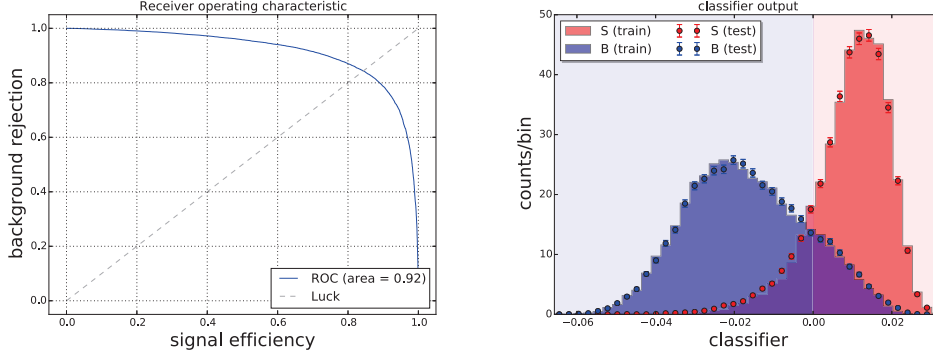


Figure 5.2: The BDT performance is plotted as a function of the signal selection efficiency and the background rejection (left); A comparison of the BDT response on the training and test samples is shown on the right.

- the significance of the impact parameter of the reconstructed B^+ respect to the primary vertex (χ_{IP}^2),
- and the angle between the reconstructed B^+ momentum vector and a line connecting the PV to the B^+ decay vertex (DIRA).

The BDT performance described as a function of the background rejection and the signal selection efficiency from different cuts and its response distributions for signal and background separation are shown in Fig. 5.2. The test samples and training samples are overlaid on the BDT response distributions to check for overtraining. The results are satisfactory and no clear overtraining is observed.

5.1.4 Particle identification

The samples can be further purified by PID requirements on the charged tracks. To select the $B^+ \rightarrow K^+ K^+ K^- \gamma$ decays, the same kaon identification criteria are applied to all the charged tracks. The BDT output and the kaon identification criteria are optimised with the figure of merit $\frac{S}{\sqrt{S+B}}$ in two dimensions (2D), where S is the number of signal events estimated from simulation and B stands for number of background events extrapolated from data sideband region to the signal region. The signal region is defined to be within the mass window $\pm 250 \text{ MeV}/c^2$ of the B^+ mass. The simulated $B^+ \rightarrow \phi K^+ \gamma$ sample is used as the signal sample for the optimisation using its known branching fraction. The PID efficiencies for charged tracks in simulation are determined using PIDCaLib package [92].

The requirements that maximise the figure of merit are $\text{ProbNNK} > 0.25$ (see Chapter 4 for ProbNNK definition) for all the charged tracks and $\text{BDT} > -0.01$. The figure of merit as a function of these two quantities is shown in Fig. 5.3. The curves of the figure of merit and signal efficiency and purity as a function of the BDT cut and PID cut at the optimal point are shown in Fig. 5.4 as an example.

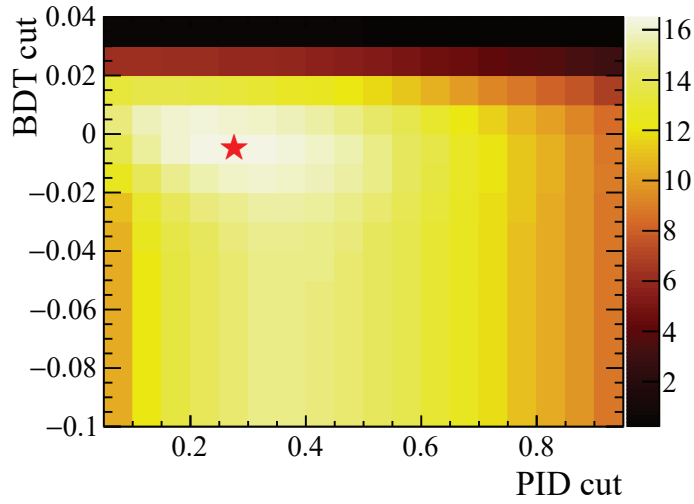


Figure 5.3: Figure of merit in bins of the BDT output and the kaon PID cut. The symbol ★ indicates the maximal figure of merit.

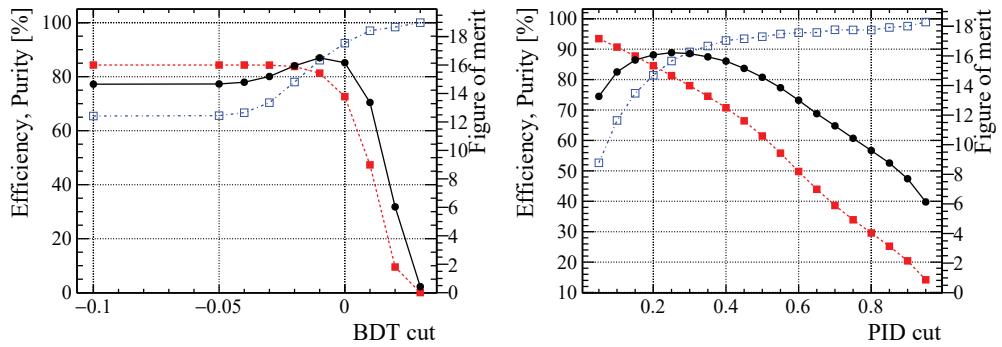


Figure 5.4: Figure of merit (black dots, right axis), signal efficiency (red full squares, left axis) and purity (blue open squares, left axis) as a function of the BDT cut with ProbNNK > 0.25 applied (left) and as a function of the PID cut with BDT > -0.01 applied (right).

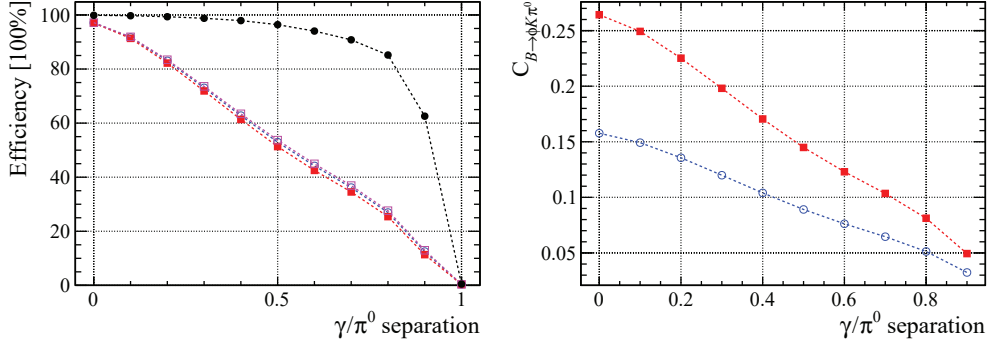


Figure 5.5: The calculated selection efficiencies (left) and the background contaminations $C_{B \rightarrow \phi K \pi^0}$ to the signal $B^+ \rightarrow \phi K^+ \gamma$ decay (right) as a function of the γ/π^0 separation variable cut in $B^+ \rightarrow \phi K^+ \gamma$ (black dots), $B^+ \rightarrow \phi K^{*+}$ (red full squares), $B^+ \rightarrow \phi K_2^*(1430)^+$ (blue open circles) and $B^+ \rightarrow \phi K^*(1680)^+$ (pink open squares) simulated samples. Uncertainties on these values range from 1% to 10% depending on the cut.

5.1.5 Merged π^0 background suppression

A dominant background source in the reconstructed $B^+ \rightarrow K^+ K^+ K^- \gamma$ decays is coming from $B^+ \rightarrow K^+ K^+ K^- \pi^0$ decays, where the two photons from the π^0 decays are reconstructed as a single photon candidate in the calorimeter (merged π^0 s). Separation of a single photon and two overlapped photons is achieved by the shape analysis of the calorimeter cluster as discussed in Chapter 2. A γ/π^0 separation variable (discussed in Chapter 4) is used to suppress the background from merged π^0 s. The selection efficiencies are studied using the simulated samples of $B^+ \rightarrow \phi K^+ \gamma$, $B^+ \rightarrow \phi K^{*+}$, $B^+ \rightarrow \phi K_2^*(1430)^+$ and $B^+ \rightarrow \phi K^*(1680)^+$ decays. Figure 5.5 shows the calculated selection efficiencies and the contaminations for the signal $B^+ \rightarrow \phi K^+ \gamma$ decay from various backgrounds, $C_{B \rightarrow \phi K \pi^0}$ (see Eq. 4.5 for definition). These are defined in the full B^+ invariant mass range $[m_{B^+} - 1150, m_{B^+} + 1750] \text{ MeV}/c^2$, as a function the γ/π^0 separation variable. At the selection level, a cut at 0.6 in γ/π^0 separation variable is applied to the selected candidates, which reduces the merged π^0 background by more than a factor 2. The results also show that the selection efficiencies for the simulated merged π^0 background samples are similar, though the kinematics are different for these decays. Their contaminations to the signal decays are different mainly due to the differences in branching fractions.

5.1.6 Background from partially reconstructed B decays

Backgrounds from partially reconstructed B decays are dominant in the low invariant mass region of the reconstructed and selected B^+ candidates. Suppression of these backgrounds can improve the signal significance and simplify the B^+ mass fit. The HOP method introduced for decays involving electrons [118] is used here to further reject the background from partially reconstructed B decays. In the HOP method, one considers the decays of type $B \rightarrow Y_h X_e$, where Y_h indicates all the particles in the final state excluding the electrons and X_e all the

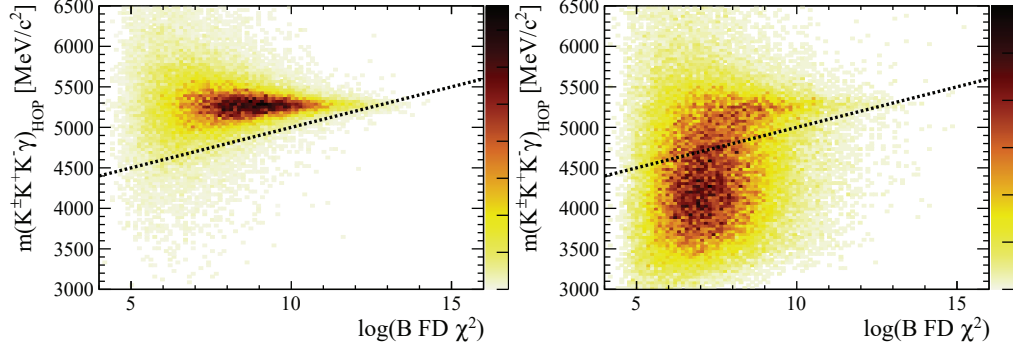


Figure 5.6: The HOP mass versus the B flight distance χ^2 in the simulated $B^+ \rightarrow K^+ K^+ K^- \gamma$ sample (left) and in data (right). The black dotted line on the plot indicates the HOP cut.

electrons. In order to compensate the momentum loss due to the final state radiations of the electrons, one uses the p_T balance relative to the direction of flight of the B meson to calculate a compensation factor α_{HOP} ,

$$\alpha_{\text{HOP}} = \frac{p_T(Y_h)}{p_T(X_e)}, \quad (5.1)$$

which can be used to correct the momentum of the X_e system to $\vec{p}^{\text{corr}} = \alpha_{\text{HOP}} \times \vec{p}_{X_e}$. The corrected momentum can then be used to calculate a corrected B mass, M_{HOP}^B , which serves to provide further background suppression by imposing

$$M_{\text{HOP}}^B > a_{\text{HOP}} + b_{\text{HOP}} \cdot \log(\chi_{\text{B FD}}^2), \quad (5.2)$$

where a_{HOP} and b_{HOP} are the parameters. The method can be generalised to the radiative B decays by replacing X_e with a photon. In this analysis, the HOP cut is chosen to be $a_{\text{HOP}} = 4000 \text{ MeV}/c^2$ and $b_{\text{HOP}} = 100$ with a signal selection efficiency of about 95% without affecting the B invariant mass distribution based on studies from simulated samples. The cut is indicated using the black dotted line on the 2D plot of the M_{HOP}^B versus χ_{FD}^2 of the reconstructed B^+ in Fig. 5.6. A comparison of the $K^+ K^+ K^- \gamma$ invariant mass distributions with and without the HOP cut imposed in the selected candidates shown in Fig. 5.7 suggests that the method is powerful at rejecting the background with particles missing in the reconstruction whilst in the mean time introduces no distortion in the signal invariant mass distribution.

5.1.7 Invariant mass distributions of the selected events

The $K^+ K^-$ and $K^+ \gamma$ invariant mass distributions can be used to study the main contributions in the selected data sample. The same sign kaons in the decay $B^+ \rightarrow K_{\text{slow}}^+ K_{\text{fast}}^+ K^- \gamma$ is sorted by track p_T where fast indicates the kaon with higher p_T and slow is the one with lower p_T . The invariant mass distributions of $K^+ \gamma$ and $K^+ K^-$ in the B^+ signal region are shown in Fig. 5.8. Clear structures of ϕ and D resonances in the $K^+ K^-$ 2D histogram are observed. The

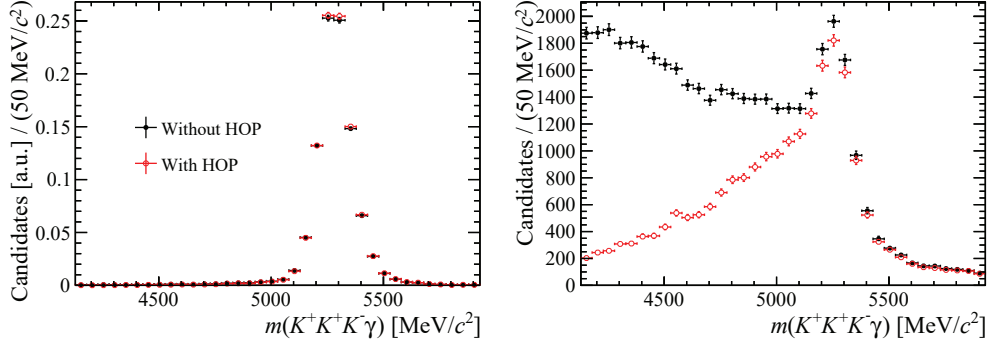


Figure 5.7: The $K^+ K^+ K^- \gamma$ invariant mass distributions reconstructed in the simulated $B^+ \rightarrow K^+ K^+ K^- \gamma$ sample (left) and in data (right), with (red circles) and without (black dots) the HOP cut applied.

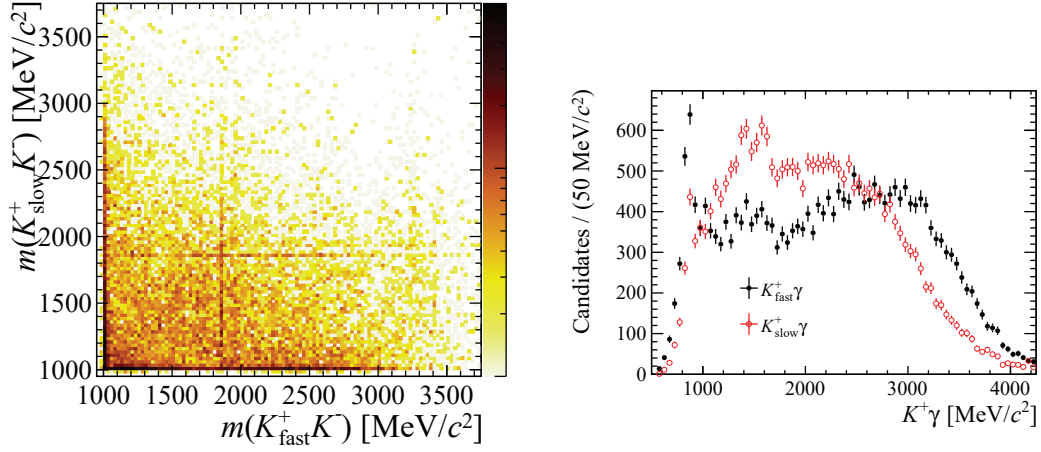


Figure 5.8: The left plot is the 2D histogram of the $K^+_{\text{slow}} K^-$ mass versus the $K^+_{\text{fast}} K^-$ mass and the right plot shows the invariant mass distributions of $K^+_{\text{slow}} \gamma$ and $K^+_{\text{fast}} \gamma$ in data.

contributions from K^{*+} and $K_2^{*+}(1430)$ are observed in the distributions of $K^+ \gamma$ invariant masses.

5.2 Selection of $B^+ \rightarrow \phi K^+ \gamma$ decays

At this stage, the selected candidates include all the possible decays of a B^+ meson decaying into a $K^+ K^+ K^- \gamma$ final state. To evaluate the feasibility of measuring the photon polarisation in the $B^+ \rightarrow \phi K^+ \gamma$ decay, further cuts are imposed to select this decay and subtract backgrounds.

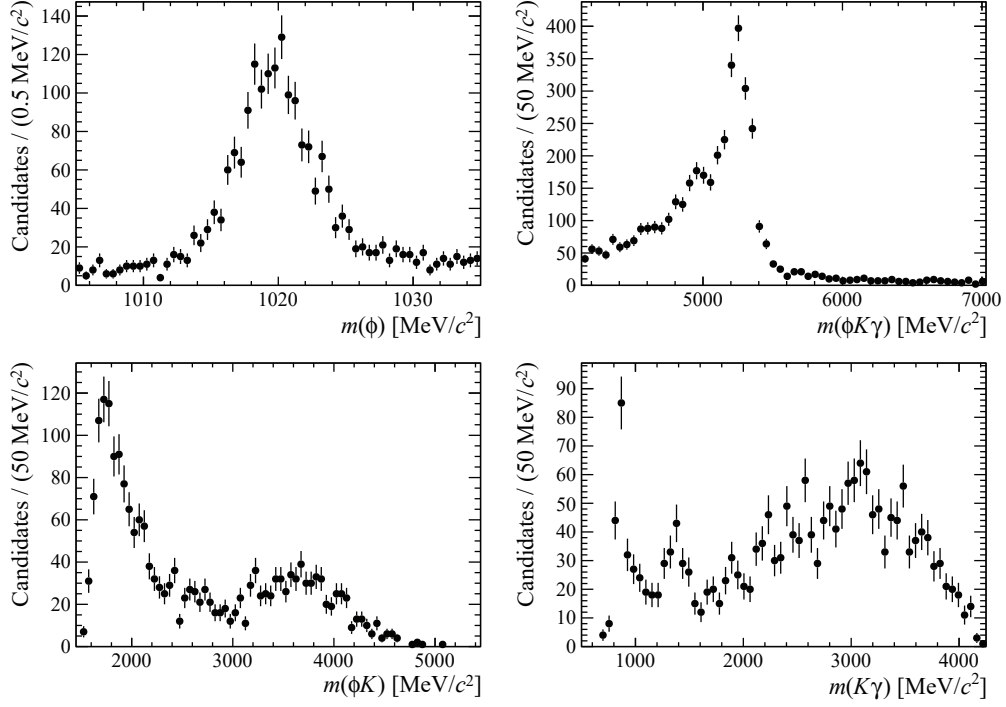


Figure 5.9: Distributions of the invariant mass of ϕ candidates (top left), $\phi K^+ \gamma$ (top right), ϕK^+ (bottom left) and $K^+ \gamma$ (bottom right) in data. The ϕK^+ and $K^+ \gamma$ invariant mass distributions are restricted in the B^+ signal region.

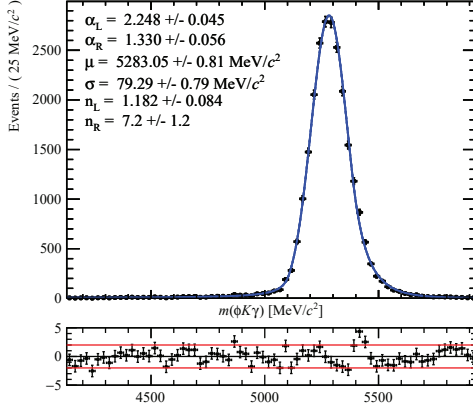
5.2.1 Selection of the ϕ state

A mass window of $\pm 15 \text{ MeV}/c^2$ around the ϕ mass is applied on $K^+ K^-$ invariant mass distributions to select the events decaying through $B^+ \rightarrow \phi K^+ \gamma$ channel. A simulated sample of $B^+ \rightarrow \phi K^+ \gamma$ decays is used to estimate the fraction of the candidates falling in the overlap region of the two $K^+ K^-$ combinations. The candidates in this region are excluded to simplify the selection as the contribution from this region is less than 1% based on studies of simulated samples.

The relevant mass distributions of the selected candidates are shown in Fig. 5.9, where the ϕK^+ and $K^+ \gamma$ invariant mass distributions are restricted to the B^+ signal region. The selected candidates populate the low mass region in the ϕK^+ invariant mass distribution. The K^{*+} and $K_2^*(1430)^+$ resonances can be seen clearly in the $K^+ \gamma$ invariant mass distributions, and thus the $B^+ \rightarrow \phi K^{*+}$ and $B^+ \rightarrow \phi K_2^*(1430)^+$ decays are sources of the background contributions to the selected $B^+ \rightarrow \phi K^+ \gamma$ candidates to be considered.

5.2.2 Fit to the $\phi K^+ \gamma$ invariant mass distribution

To perform the mass fit on the $\phi K^+ \gamma$ invariant mass distribution, an unbinned extended maximum likelihood fit is used. The signal and background models are studied using the



Parameter	Value
μ	$5283.1 \pm 0.1 \text{ MeV}/c^2$
σ	$79.3 \pm 0.8 \text{ MeV}/c^2$
α_L	2.25 ± 0.05
α_R	1.33 ± 0.06
n_L	1.18 ± 0.08
n_R	7.2 ± 1.2

Figure 5.10: Fit of the invariant mass distribution of $\phi K^+ \gamma$ in simulated $B^+ \rightarrow \phi K^+ \gamma$ sample. The parameters of the model from the fit are reported in the table on the right.

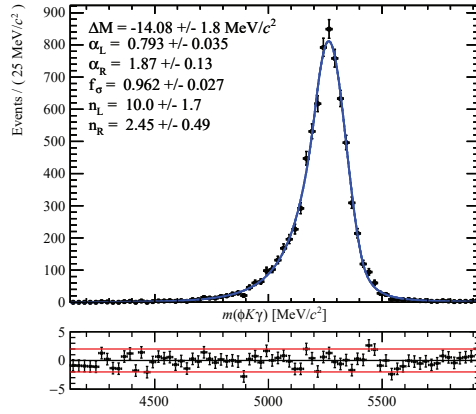
simulated samples discussed in detail in the following text.

The signal lineshape is extracted from the simulated sample with trigger, stripping and offline selection applied. A double-sided Crystal Ball function is used to describe the signal invariant mass distribution. The fit results on the simulated sample of $B^+ \rightarrow \phi K^+ \gamma$ decay are shown in Fig. 5.10.

The background shape for the merged π^0 background $B^+ \rightarrow \phi K^+ \pi^0$ is determined from a fit to the simulated $B^+ \rightarrow \phi K^{*0}$ sample as shown in Fig. 5.11. A double-sided Crystal Ball function is used to model this background. Due to the similarity of the merged π^0 background with the signal in the $\phi K^+ \gamma$ invariant mass distributions, the merged π^0 background shape and normalisation in the fit model are both required to be fixed. The contamination of the decays $B^+ \rightarrow \phi K^+ \pi^0$ is estimated to be $\sim 20\%$ using simulated $B^+ \rightarrow \phi K^{*+}$ and $B^+ \rightarrow \phi K_2^*(1430)^+$ samples, as shown in Fig. 5.5. Studies in Section 5.1.5 also show no clear dependence of the selection efficiencies of the main merged π^0 background contributions on their decay modes. Considering the final state of interest reachable via decay chains with known branching fractions in the PDG, the total contamination of merged π^0 backgrounds to the signal decays could be up to 25% by simply scaling the branching fractions.

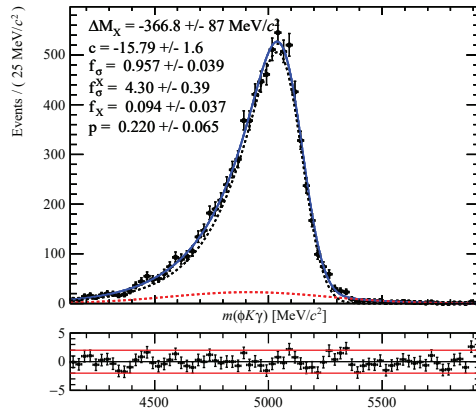
The backgrounds from partially reconstructed B decays are highly suppressed by imposing the HOP cut. The decays with a missing pion are supposed to be the dominant contribution because they are close to the signal region and the HOP criteria is less powerful close to the signal region. The simulated $B^0 \rightarrow \phi K^{*0} \gamma$ sample is used to study the background shape. An ARGUS convoluted with a Gaussian resolution function is used to fit the reconstructed $\phi K^+ \gamma$ invariant mass distribution in the simulated $B^0 \rightarrow \phi K^{*0} \gamma$ sample. The fit result on the simulated $B^0 \rightarrow \phi K^{*0} \gamma$ sample is shown in Fig. 5.12.

The mass fit on the $\phi K^+ \gamma$ invariant mass distribution and its fit results are shown in Fig. 5.13,



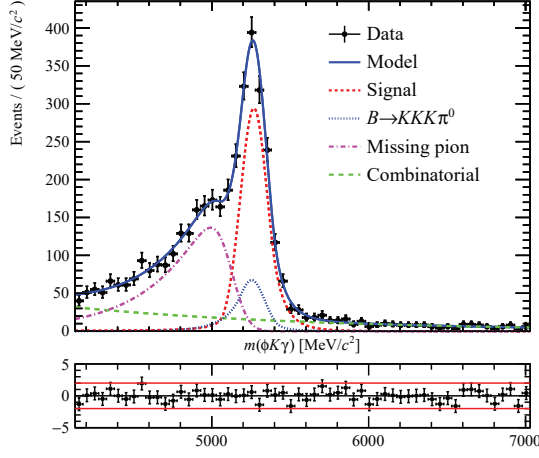
Parameter	Value
ΔM	$-14.1 \pm 1.8 \text{ MeV}/c^2$
f_σ	0.96 ± 0.03
α_L	0.79 ± 0.04
α_R	1.9 ± 0.1
n_L	10.0 ± 1.7
n_R	2.4 ± 0.5

Figure 5.11: Fit of the invariant mass distribution of $\phi K^+ \gamma$ for simulated $B^+ \rightarrow \phi K^+ \gamma$ sample. The parameters of the model from the fit are reported in the tables on the right.



Parameter	Value
ΔM	m_π
f_σ	0.96 ± 0.04
c	-15.8 ± 1.6
p	0.22 ± 0.06

Figure 5.12: Fit of the invariant mass distribution of $\phi K^+ \gamma$ in simulated $B^0 \rightarrow \phi K^{*0} \gamma$ sample. The parameters of the model from the fit are reported in the tables on the right. A wide Gaussian function is used to take into account the other reconstruction and selection effects which causes the distribution to differ slightly from an ARGUS shape.



N_{Signal}	1368 ± 48
μ (MeV/ c^2)	5268.7 ± 4.1
σ (MeV/ c^2)	86.0 ± 3.3
$N_{\text{Combinatorial}}$	831 ± 114
τ (GeV $^{-1}/c^{-2}$)	-0.64 ± 0.12
$C_{B \rightarrow \phi K \pi^0}$	0.25
$C_{B \rightarrow \phi K \pi \gamma (\pi^0)}$	1.1 ± 0.1
c	-8.0 ± 2.1
p	0.18 ± 0.16

Figure 5.13: Fits on the invariant mass distribution of $\phi K^+ \gamma$ in data with the fitted parameters shown in the table on the right.

where the contamination from merged π^0 background is fixed to be 0.25. The signal yield is 1368 ± 48 , obtained from the mass fit, and the uncertainty is statistical only. In the fit model, the tail parameters for the signal model and the merged π^0 background shape are fixed to parameters determined from simulation. The mean and resolution parameters of the signal model are left free in the fit model and means and resolutions for background models are defined relatively to the signal resolution with the ratio fixed to the values determined from simulation. The parameters c and p for the curvature and power of the ARGUS function are left free in the final fit to account for other possible backgrounds from the partially reconstructed B decays.

5.2.3 Separation of the merged π^0 contribution from signals

In the $\phi K^+ \gamma$ invariant mass spectrum, most backgrounds are easily subtracted because their shape differs significantly from the signal shape, for example with the $sPlot$ method. For the background from merged π^0 s, this is not true, as it is virtually indistinguishable from signals. Since it is not desirable to rely on (un-)measured branching fractions and simulation to determine the contamination from merged π^0 s, the key ingredient for this analysis is to find another variable that gives sufficient separation power between signal and the merged π^0 contamination. This can be achieved by exploiting the different calorimeter response between real photons and merged π^0 s, which is captured in a γ/π^0 separation variable.

The γ/π^0 separation variable which exploits the differences in the calorimeter cluster shapes to distinguish photons from merged π^0 s, can be used to separate merged π^0 s from the real photons. The distributions of the γ/π^0 separation variable for photons and merged π^0 s are shown in Fig. 5.14 in the calibration samples of $B^0 \rightarrow K^{*0} \gamma$ decay and $D^0 \rightarrow K \pi \pi^0$ decay from the 2011 and 2012 data samples. The templates obtained from the calibration samples

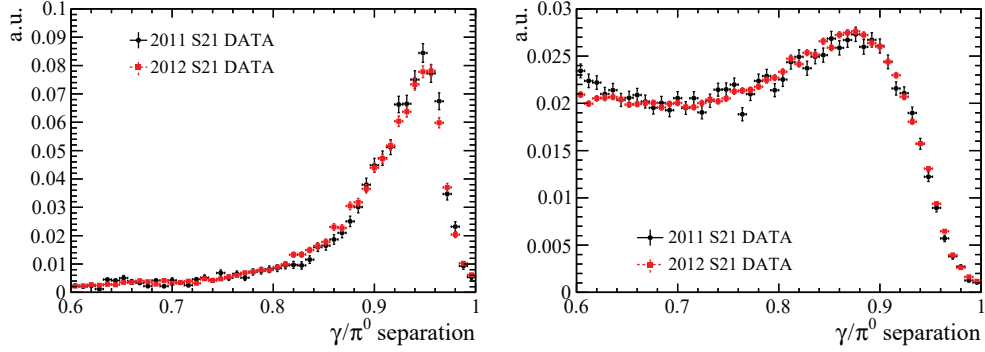


Figure 5.14: Distributions of the γ/π^0 separation variable in the calibration samples of $B^0 \rightarrow K^{*0} \gamma$ decay and $D^0 \rightarrow K \pi \pi^0$ decay.

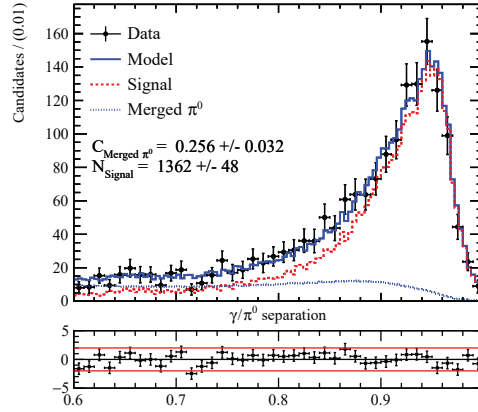


Figure 5.15: Fit of the γ/π^0 separation variable on the background subtracted data sample using the templates from calibration samples.

$B^0 \rightarrow K^{*0} \gamma$ and $D^0 \rightarrow K \pi \pi^0$ can be used to describe the γ/π^0 separation variable seen in the signal with true photons and background of merged π^0 s, respectively.

The distribution of the γ/π^0 separation variable for the background subtracted signals is shown in Fig. 5.15. A fit is performed on the γ/π^0 separation variable to separate the contributions from signal and merged π^0 s. The determined number of signal candidates is 1362 ± 48 where the uncertainty is only statistical. The contamination fraction of the merged π^0 background is fitted to be 0.26 ± 0.03 using templates from the sum of the 2011 and 2012 calibration samples.

The γ/π^0 separation variable is known to be momentum and pseudorapidity dependent. The transverse momentum p_T and pseudorapidity η distributions for the calibration samples and the simulated merged π^0 samples are shown in Fig. 5.16. The merged π^0 contribution in the selected candidates are dominated by the contributions from the decays of $B^+ \rightarrow \phi K^{*+}$ and $B^+ \rightarrow \phi K_2^*(1430)^+$ into the $\phi K^+ \pi^0$ final state. To evaluate the effects due to the momentum and pseudorapidity difference shown in Fig. 5.16 between the possible π^0 background contribution and the calibration sample, the γ/π^0 separation variable distribution in the calibration sample

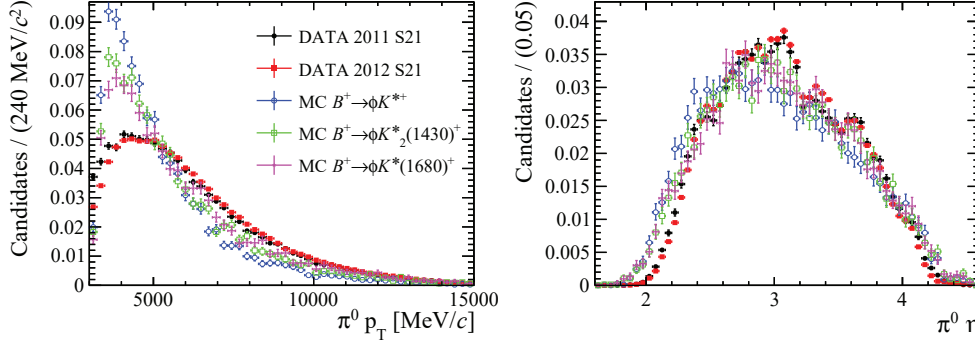


Figure 5.16: Distributions of the transverse momentum (p_T , left) and the pseudorapidity (η , right) of the merged π^0 s from the calibration sample $D^0 \rightarrow K\pi\pi^0$ and the simulated $B^+ \rightarrow \phi K^{*+}$, $B^+ \rightarrow \phi K_2^*(1430)^+$ and $B^+ \rightarrow \phi K^*(1680)^+$ samples.

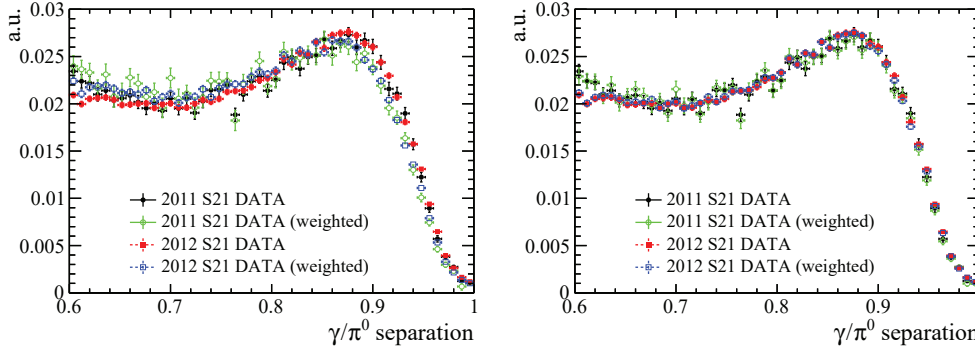


Figure 5.17: The γ/π^0 separation variable distributions with (full markers) and without (open markers) the weights included in the calibration sample $D^0 \rightarrow K\pi\pi^0$. The weights are from the simulated $B^+ \rightarrow \phi K^{*+}$ (left) and $B^+ \rightarrow \phi K_2^*(1430)^+$ (right) samples.

is weighted using the p_T and η distributions in the simulated samples.

The weighted γ/π^0 separation variable distributions in the calibration sample using the weights from the simulated samples together with unweighted distributions are shown in Fig. 5.17. Using the weighted γ/π^0 separation variable distribution, the fit shown in Fig. 5.15 is repeated by using different simulated samples. The fitted number of signals and the merged π^0 contamination are reported in Table. 5.1. The deviation due to the momentum and pseudorapidity dependence is smaller than the statistical uncertainty. This effect will be considered as one of the systematic contributions in the measurements performed later.

5.3 Direct CP asymmetry measurement in the $B^+ \rightarrow \phi K^+ \gamma$ decay

The direct CP asymmetry for the $B^+ \rightarrow \phi K^+ \gamma$ decay, A_{CP} , is approximately given by

$$A_{CP} = A_{CP}^{\text{raw}} - A_P(B^+) - A_D(K^+_{\text{bachelor}}), \quad (5.3)$$

Table 5.1: The number of signal N_{Signal} and the merged π^0 contamination $C_{\text{Merged } \pi^0}$ from the fit on the γ/π^0 separation variable distribution using the templates for merged π^0 s weighted by different simulated sample.

Simulated sample	No weights	$B^+ \rightarrow \phi K^{*+}$	$B^+ \rightarrow \phi K_2^*(1430)^+$	$B^+ \rightarrow \phi K^*(1680)^+$
N_{Signal}	1362 ± 48	1380 ± 47	1365 ± 48	1357 ± 48
$C_{\text{Merged } \pi^0}$	0.26 ± 0.03	0.24 ± 0.03	0.25 ± 0.03	0.26 ± 0.03

where A_{CP}^{raw} is the direct CP asymmetry extracted from data and the K^+ in the $B^+ \rightarrow \phi K^+ \gamma$ decay is named the bachelor kaon. The $A_P(B^+)$ is the asymmetry in the production of B^+ and B^- in pp collisions and is defined as

$$A_P(B^+) \equiv \frac{\sigma_{B^-} - \sigma_{B^+}}{\sigma_{B^-} + \sigma_{B^+}}, \quad (5.4)$$

where σ represents the B meson production cross-section in the LHCb acceptance. The $A_D(K_{\text{bachelor}})$ is the detection asymmetry coming from the differences between negative and positive bachelor kaons that arise in the interaction with matter, detector acceptance and reconstruction.

The determination of the raw CP asymmetry, A_{CP}^{raw} , is done by performing a simultaneous fit on the two datasets with opposite charges of B meson. The raw CP asymmetry can be written as

$$A_{CP}^{\text{raw}} = \frac{N^- - N^+}{N^- + N^+} \Rightarrow N^\pm = \frac{1}{2}N(1 \mp A_{CP}^{\text{raw}}), \quad (5.5)$$

where N^+ and N^- are signal yields for B^+ and B^- respectively and the total signal yield is $N = N^+ + N^-$. The parameters N and A_{CP}^{raw} are the observables to be extracted from the fit.

To account for the potential bias from the non-uniformities in the detector due to the fact that the magnetic field could spread out the opposite charge in different regions of the detector, the data sample is split into the one with magnet polarity up (*MagUp*) and the other with magnet polarity down (*MagDown*). Consequently, to extract the A_{CP}^{raw} , a simultaneous fit is performed on the reconstructed B invariant mass distributions from the four data samples with opposite charges of B meson and different magnet polarities. The four data samples share the same signal model and merged π^0 background model but allow asymmetries in all the background contributions. The contaminations from the merged π^0 background are fitted to be 0.29 ± 0.05 and 0.23 ± 0.04 from the fits on the γ/π^0 separation variable (see Fig. 5.18) for the data sample *MagUp* and *MagDown*, respectively, which are gaussian constrained to these values in the simultaneous fit. The contamination and models of the partially reconstructed background and the combinatorial background are allowed to be different between *MagUp* sample and *MagDown* sample.

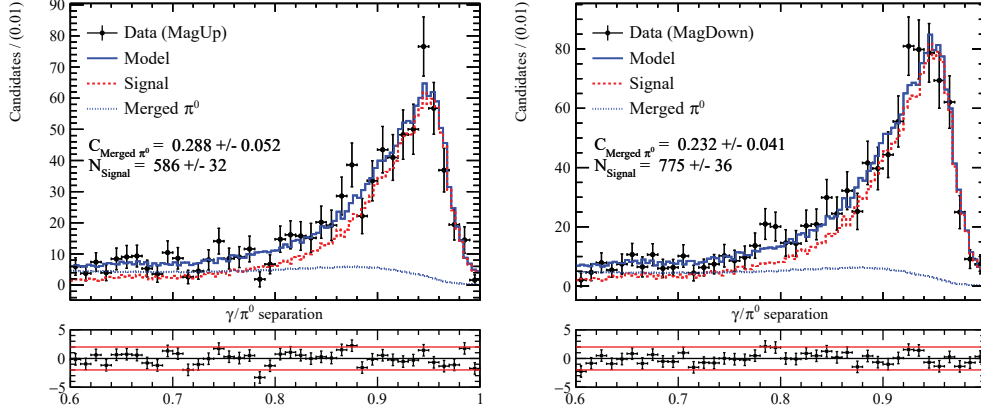


Figure 5.18: Fit of the γ/π^0 separation variable distributions for the data sample with the magnet polarity up (left) and down (right).

The extracted A_{CP}^{raw} value from the simultaneous fit on the four samples is

$$A_{CP}^{\text{raw}} = (-0.2 \pm 2.1)\% \quad (5.6)$$

where the fits are shown in Fig. 5.19 and the fit parameters are reported in Table 5.2. The total extracted number of signal events N_{Signal} is 1363 ± 46 by summing up the number of events in *MagUp* and *MagDown* samples, where the uncertainties are purely statistical. The profile likelihood is also shown in Fig. 5.20 as a function of A_{CP}^{raw} , obtained by minimising the likelihood at each value of A_{CP}^{raw} .

A thousand of pseudoexperiment data samples are used to validate the fit procedure. These pseudoexperiments are generated using the parameters extracted from the fits shown in Fig. 5.19 and Table 5.2. The resolution and pull distributions of the A_{CP}^{raw} parameter are displayed in Fig. 5.21. No significant bias is observed.

The $K^- \pi^+$ detection asymmetry, $A_D(K^- \pi^+)$, is studied in Ref. [119] by comparing the charge asymmetries in prompt $D^+ \rightarrow K^- \pi^+ \pi^+$ and $D^+ \rightarrow \bar{K}^0 \pi^+$ decays (D^+ decays produced directly in pp collisions). The measured asymmetry, $A_D(K^- \pi^+) = (-1.17 \pm 0.12)\%$, is dominated by the different interaction cross sections of K^- and K^+ mesons in matter [39], which is a function of the kaon momentum shown in Fig. 5.22. Thus, the measured $A_D(K^- \pi^+)$ can be approximately considered as $A_D(K^-)$. The momentum of the bachelor kaon in the $B^+ \rightarrow \phi K^+ \gamma$ decay in the background subtracted data sample is also shown in Fig. 5.22 for comparison. Looking at Fig. 5.22, the momentum range of the kaons are the same, thus the mistake due to different kaon momentum spectra is limited to the spread of the asymmetries measured in Ref. [119] which is about $\pm 0.3\%$. To conclude, the kaon detection asymmetry $A_D(K_{\text{bachelor}})$ then is taken as $(-1.2 \pm 0.3)\%$.

The production asymmetry between B^+ and B^- mesons is $(-0.6 \pm 0.6)\%$ obtained from the observed asymmetry in $B^+ \rightarrow J/\psi K^+$ decays [120] after correcting for the kaon detection

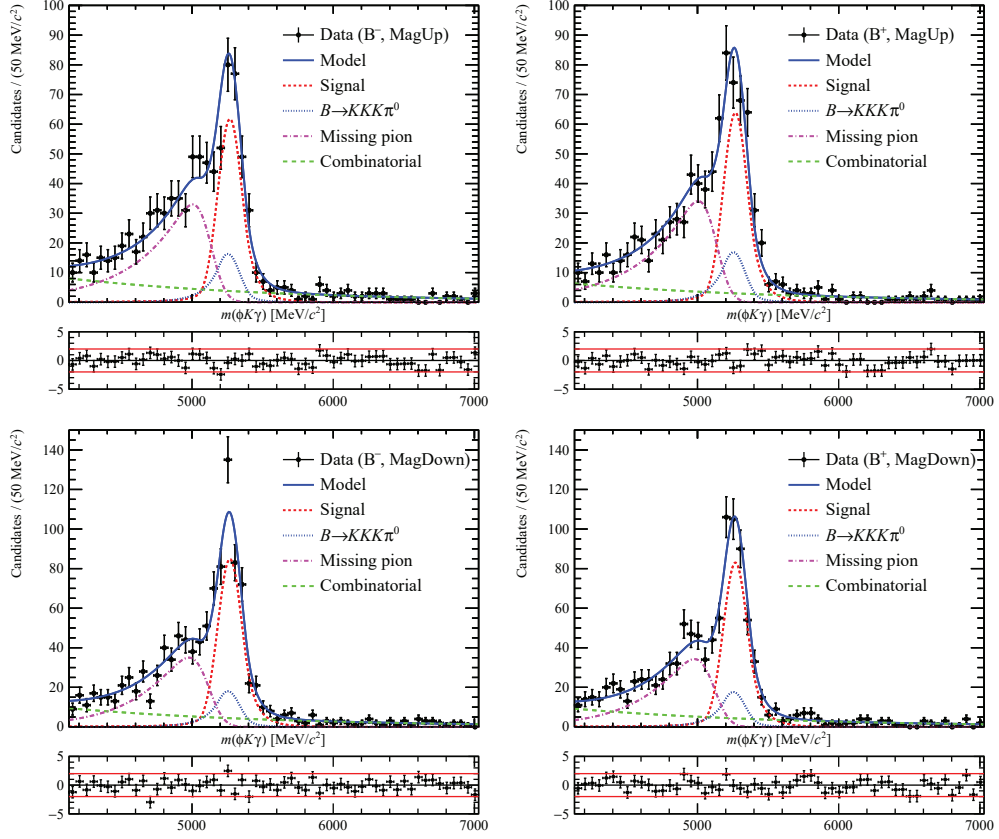


Figure 5.19: Fit of the reconstructed B invariant mass distributions for B^- with magnet polarity up (top left) and polarity down (bottom left) and for B^+ with magnet polarity up (top right) and polarity down (bottom right).

Table 5.2: Fit parameters of the simultaneous fit on the B invariant mass distributions using the data samples with opposite charges and different magnet polarities.

Parameter	<i>MagUp</i>	<i>MagDown</i>
A_{CP}^{raw}	$(-0.2 \pm 2.1)\%$	
N_{Signal}	583 ± 30	780 ± 35
μ (MeV/c^2)	5268.6 ± 5.3	
σ (MeV/c^2)	85.8 ± 3.4	
c	-7.1 ± 2.5	-9.7 ± 3.6
p	0.07 ± 0.17	0.34 ± 0.27
C_{Partial}	1.23 ± 0.14	0.94 ± 0.12
τ ($\frac{1}{\text{GeV}/c^2}$)	-0.66 ± 0.16	-0.67 ± 0.16
$N_{\text{Combinatorial}}^-$	211 ± 40	239 ± 47
$N_{\text{Combinatorial}}^+$	162 ± 35	239 ± 50

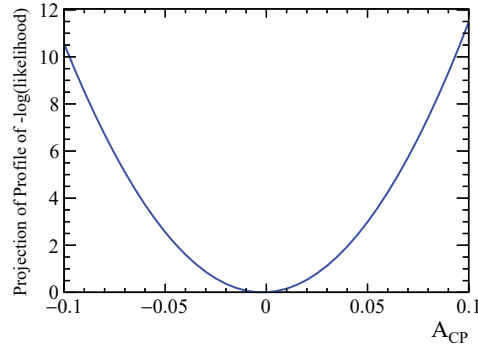


Figure 5.20: Likelihood profile as a function of the A_{CP}^{raw} values.

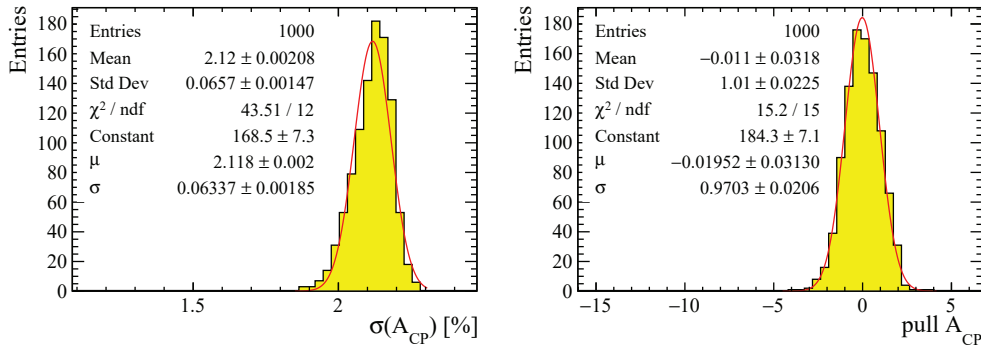


Figure 5.21: The resolution (left) and pull (right) distributions of the A_{CP}^{raw} parameter obtained with 1000 pseudoexperiment data samples.

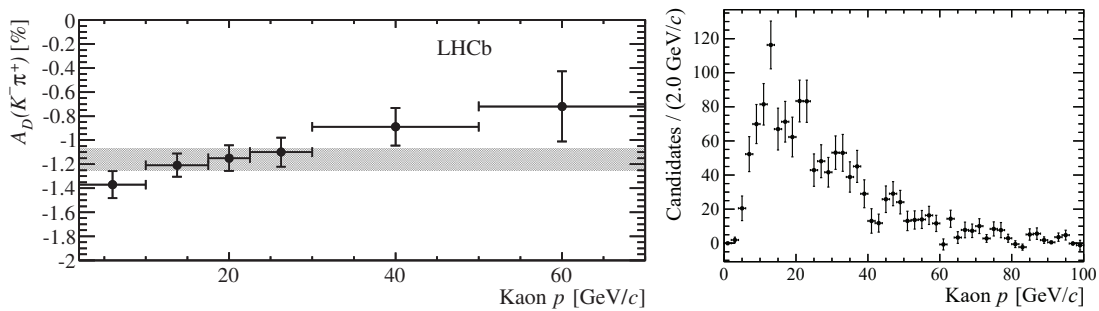


Figure 5.22: Measured $K^- \pi^+$ detection asymmetry as a function of the kaon momentum using prompt $D^- \rightarrow K^+ \pi^- \pi^-$ and $D^- \rightarrow K_s^0 \pi^-$ decays from Ref. [119] shown on the left. The shaded band indicates the average asymmetry integrated over the bins. The bachelor kaon momentum distribution in the $B^+ \rightarrow \phi K^+ \gamma$ decay in the background subtracted data sample is shown on the right.

Table 5.3: Systematic uncertainties on the measured A_{CP}^{raw} .

Source	Uncertainty
Fit model	$\pm 0.01\%$
γ/π^0 separation reweighting	negligible
B^+ production asymmetry	$\pm 0.6\%$
K^+ detection asymmetry	$\pm 0.3\%$
Quadratic sum	$\pm 0.7\%$

asymmetry and the direct CP asymmetry $(0.3 \pm 0.6)\%$ [39].

The systematic contribution to the A_{CP} measurement from the fit model is evaluated by

- varying the fixed parameters $\alpha_{L(R)}$ and $n_{L(R)}$ in the double-tailed Crystal Ball function for the signal model within their uncertainties (see Fig. 5.10);
- varying the fixed parameters ΔM , f_σ , $\alpha_{L(R)}$ and $n_{L(R)}$ in the double-tailed Crystal Ball function for the merged π^0 background model within their uncertainties (see Fig. 5.11);
- varying the fixed parameter f_σ in the gaussian resolution function for the partially reconstructed background model (see Fig. 5.12).

The estimated contributions to the systematic error from the signal model ($\pm 0.008\%$), the merged π^0 background model ($\pm 0.005\%$) and the partially reconstructed background model ($\pm 0.005\%$) are summed in quadrature leading to a systematic uncertainty of $\pm 0.01\%$.

The contamination of the merged π^0 background is re-evaluated with the fits on the γ/π^0 separation variable distributions using the weighted template for the merged π^0 s, as discussed in Section 5.2.3. The values are found to be 0.27 ± 0.05 for *MagUp* sample and 0.22 ± 0.04 for *MagDown* sample from the fits, which results in a negligible difference on the measured A_{CP}^{raw} value compared to using the values 0.29 ± 0.05 for *MagUp* and 0.23 ± 0.04 for *MagDown* from fits in Fig. 5.18.

In summary, the total systematic uncertainty on the measured direct CP asymmetry is $\pm 0.6\%$, detailed in Table 5.3.

The measured direct CP asymmetry A_{CP} in the $B^+ \rightarrow \phi K^+ \gamma$ decay is

$$A_{CP}(B^+ \rightarrow \phi K^+ \gamma) = (1.6 \pm 2.1(\text{stat.}) \pm 0.7(\text{syst.}))\%, \quad (5.7)$$

where the first uncertainty is the statistical uncertainty and the second one is the systematic uncertainty. The dominant contribution to the systematic uncertainty is from the precision of the measured B^+ production asymmetry.

The CP asymmetry in $B^+ \rightarrow \phi K^+ \gamma$ decay amplitudes has been measured by the BaBar and Belle experiments to be $(-26 \pm 14(\text{stat.}) \pm 5(\text{syst.}))\%$ [114] using 85 events and $(-3.0 \pm 11(\text{stat.}) \pm$

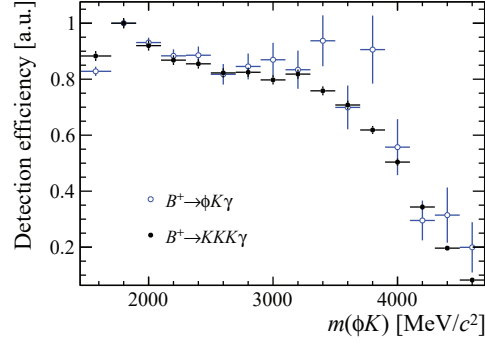


Figure 5.23: The relative detection efficiency as a function of the ϕK^+ invariant mass from the simulated samples. The maximum of the distribution is scaled to 1.

8(syst.))% [40] using 144 events, respectively. At LHCb, with much larger statistics, we can reduce the statistical uncertainty on the measured CP asymmetry by a factor 5 for $B^+ \rightarrow \phi K^+ \gamma$ decay. The SM expected direct CP asymmetry in the radiative decays $b \rightarrow s \gamma$ at the quark level is $-(0.1 - 1)\%$ [121]. This measurement is consistent with the SM prediction.

5.4 Hadronic structures in ϕK invariant mass distribution

The ϕK invariant mass distribution in the $B \rightarrow \phi K \gamma$ was studied by the Belle collaboration [40] in the mass range of $1.5 \text{ GeV}/c^2 < m(\phi K) < 4.0 \text{ GeV}/c^2$. They found that the signal events are concentrated in the low mass region below $2.0 \text{ GeV}/c^2$. The spectra is consistent with the perturbative QCD model prediction for nonresonant $B \rightarrow \phi K \gamma$ decay qualitatively after including the kaon mass [40, 122].

The relative detection efficiencies for the simulated $B^+ \rightarrow K^+ K^+ K^- \gamma$ and $B^+ \rightarrow \phi K^+ \gamma$ samples as a function of the ϕK^+ invariant mass are shown in Fig. 5.23, where the normalisation is done by scaling the maximum of the efficiency distributions to 1. Due to the low statistics of the simulated events generated at the higher ϕK mass region in the simulated $B^+ \rightarrow \phi K^+ \gamma$ sample, the uncertainties on the calculated efficiencies are large. Since the two efficiencies agree within the statistical uncertainties, the simulated $B^+ \rightarrow K^+ K^+ K^- \gamma$ sample is used for the relative efficiency corrections.

To measure the ϕK invariant mass distribution, the fit to the γ/π^0 separation variable distribution is repeated in bins of ϕK mass. The resulting signal yields and the contamination fractions of merged π^0 s as a function of the ϕK^+ invariant mass, together with the efficiency corrected ϕK^+ invariant mass distribution, are shown in Fig. 5.24.

The potential contributions to the ϕK^+ invariant mass distributions can be from

- $B^+ \rightarrow \phi K^+ \gamma$ decays with the ϕK^+ -system as a resonance with spin $J \geq 1$;
- the nonresonant three-body $B^+ \rightarrow \phi K^+ \gamma$ decays;

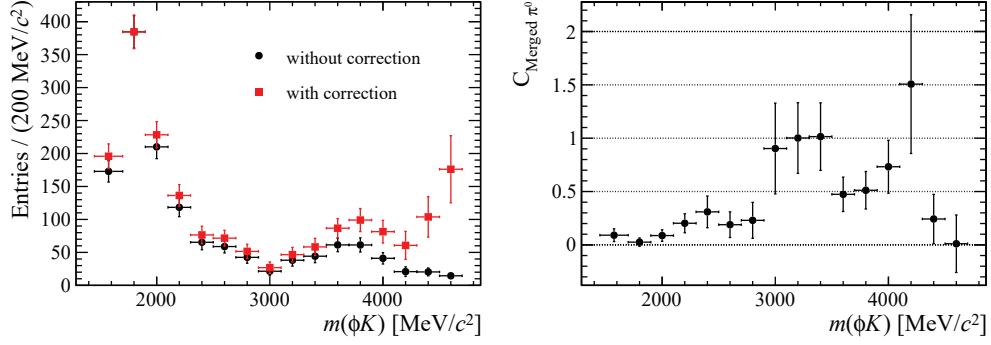


Figure 5.24: The background subtracted ϕK^+ invariant mass distributions without (black dots) and with (red squares) efficiency corrections are shown on the left; the contamination of the merged π^0 background in each ϕK^+ mass bin is shown on the right.

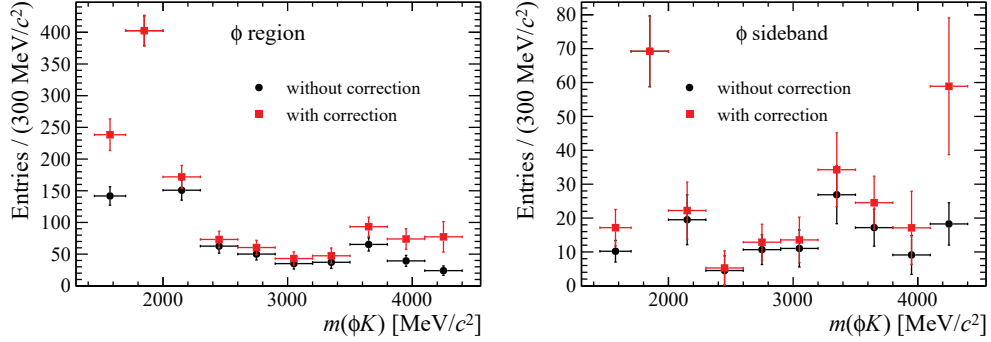


Figure 5.25: Background subtracted ϕK^+ invariant mass distributions in a mass window region $\pm 5 \text{ MeV}/c^2$ of the ϕ mass (left) and the sideband region $[m_\phi + 15, m_\phi + 50] \text{ MeV}/c^2$ (right). The invariant mass distributions without the efficiency corrections are shown in black dots and the ones with efficiency corrections are shown in red squares.

- the B^+ decays with a final state of $K^+ K^+ K^- \gamma$ but without a ϕ intermediate state.

The decays without ϕ intermediate state are studied using the signal candidates in the ϕ invariant mass distribution sideband region $[1035, 1070] \text{ MeV}/c^2$. The $K^+ K^+ K^-$ invariant mass distributions for the background subtracted B^+ sample, with the subtraction of the merged π^0 backgrounds, are shown in Fig. 5.25 for a ϕ signal region (a mass window $\pm 5 \text{ MeV}/c^2$ of the ϕ mass) and the sideband region. In the ϕ sideband region, the same excess in the low ϕK^+ mass region as in the ϕ region observed, but the excess at the high ϕK^+ mass region is more clear in the sideband region than in the signal region. This result supports that the structure at ϕK^+ invariant mass region above $3 \text{ GeV}/c^2$ is likely due to the contributions from $B^+ \rightarrow K^+ K^+ K^- \gamma$ decays without a ϕ intermediate state in the $K^+ K^-$ invariant mass distributions.

In conclusion, the ϕK^+ invariant mass distribution in the $B^+ \rightarrow \phi K^+ \gamma$ decay is consistent with studies performed by the Belle collaboration. No clear evidence of the contribution from any resonances is found. Since the events populated at the low ϕK^+ invariant mass region,

the nonresonant three-body decays $B^+ \rightarrow \phi K^+ \gamma$ could be the dominant contributions in the decays of a B^+ meson decaying into the $\phi K^+ \gamma$ final state.

5.5 Photon polarisation measurement

The helicity formalism [22] is used to describe the decay amplitudes of the $B^+ \rightarrow f_s \gamma$ decay where f_s is a resonance of spin-parity J^P with the z -component m decaying into two particles ϕ and K^+ of spins and helicities s_ϕ, λ_ϕ and s_{K^+}, λ_{K^+} , respectively. In the $[\phi K^+]$ rest frame, the decay $f_s \rightarrow (\phi \rightarrow K^+ K^-) K^+$ is

$$B^+ \rightarrow [\phi(-\vec{p}_3) K^+(\vec{p}_3)] \gamma \rightarrow K^+(\vec{p}_1) K^-(\vec{p}_2) K^+(\vec{p}_3) \gamma, \quad (5.8)$$

with $\vec{p}_1 + \vec{p}_2 + \vec{p}_3 = 0$. The amplitude A_m for the sequential decay is proportional to

$$A_m \propto \sum_{J, \lambda_\phi} \langle K^+(\vec{p}_1) K^-(\vec{p}_2) | \Delta H_\phi | \phi(-\vec{p}_3, \lambda_\phi) \rangle \times \langle \phi(-\vec{p}_3, \lambda_\phi) K^+(\vec{p}_3) | \Delta H_{f_s} | f_s(0; J, m) \rangle, \quad (5.9)$$

where $m = +1$ corresponds to the left-handed photon and $m = -1$ to the right-handed one. The first factor is a p -wave decay of the vector ϕ into two kaons and the second one describes the transition of the initial hadronic system $[\phi K^+]$ into a system of ϕ and K mesons.

5.5.1 Angular distribution in the $B^+ \rightarrow \phi K^+ \gamma$ decay

We define two coordinate systems related to the decay of interest. The z -axis in the $[\phi K]$ rest frame is antiparallel to the photon momentum: $\vec{p}_\gamma / |\vec{p}_\gamma| = -\hat{e}_z$. We define the z' -axis as being orthogonal to the plane defined by the 3-momenta of final state kaons, *i.e.* the $[\phi K^+]$ decay plane, while the y' -axis is directed along \vec{p}_3 :

$$\hat{e}_{z'} = \frac{\vec{p}_1 \times \vec{p}_2}{|\vec{p}_1 \times \vec{p}_2|}, \quad (5.10)$$

$$\hat{e}_{y'} = \frac{\vec{p}_3}{|\vec{p}_3|}, \quad (5.11)$$

and $\hat{e}_{x'} = \hat{e}_{y'} \times \hat{e}_{z'}$.

The angle θ is defined as the angle between the z - and z' -axes, *i.e.* between the photon momentum and normal to the $[\phi K]$ decay plane. There are polar and azimuthal angles (η, φ) for the vector \vec{p}_3 in the (x, y, z) frame. Note that these angles are defined in the $[\phi K^+]$ rest frame and the angle φ is unobservable. The momenta and angle conventions are represented in Fig. 5.26.

In an analogous way in the ϕ rest frame, one has $\phi(\vec{p} = 0) \rightarrow K(\vec{p}_1^*) K(-\vec{p}_1^*)$, and the polar angle θ^* of the vector \vec{p}_1^* is defined with respect to the y' axis, while the azimuthal angle ϕ^* measures the rotation of \vec{p}_1^* around this axis. It is not independent and can be simply

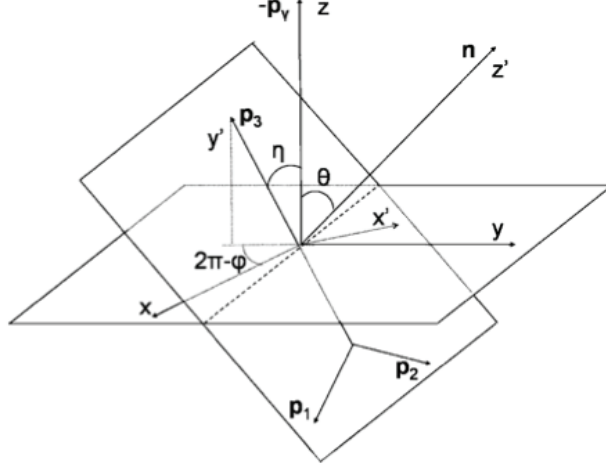


Figure 5.26: Angle conventions for the decay $B^+ \rightarrow [\phi \rightarrow K^+(\vec{p}_1)K^-(\vec{p}_2)]K^+(\vec{p}_3)\gamma(\vec{p}_\gamma)$. Figure from Ref. [22].

expressed as a function of η and θ . To summarise, we have

$$\cos\theta = \hat{e}_z \cdot \hat{e}_{z'}, \quad (5.12)$$

$$\cos\eta = \hat{e}_z \cdot \hat{e}_{y'}, \quad (5.13)$$

$$\cos\theta^* = \hat{e}_{y'} \cdot \vec{p}_1^* / |\vec{p}_1^*|, \quad (5.14)$$

$$\sin\phi^* = \cos\theta / \sin\eta, \quad (5.15)$$

where \vec{p}_1^* is the momentum of the fastest kaon resulting from ϕ decay in the ϕ rest frame.

5.5.2 Extraction of the photon polarisation parameter

In the following, we assume that the main contributions to the ϕK^+ -system is only the $J = 1$ term, which corresponds to inclusion of s - and d -waves for the $J^P = 1^+$ state and p -wave for the $J^P = 1^-$ state. The first factor in Eq. 5.9 is the standard expression for p -wave decay of the vector ϕ resonance into two kaons:

$$\bar{a}_1 \cdot D_{\lambda_\phi 0}^{1*}(\phi^*, \pi - \theta^*, 0), \quad (5.16)$$

where \bar{a}_1 is the p -wave amplitude of the decay $\phi \rightarrow K^+ K^-$ and the Wigner-D functions $D_{mm'}^J$ define the rotations on the spin space. The second factor in Eq. 5.9 can be expanded into the sum over the partial waves with each partial wave amplitude a_l entering with the factor

$$a_l \cdot \sqrt{2l+1}(l, 0, 1, \lambda_\phi | J, \lambda_\phi) \cdot D_{M\lambda_\phi}^{J*}(\phi, \pi - \eta, 0), \quad (5.17)$$

where the ϕ helicity is $\lambda_\phi = 0, \pm 1$, the relative orbital momentum of the states ϕ and K^+ is $l = 0, 1, 2$ for s -, p - and d -wave and $(l, 0, 1, \lambda_\phi)$ are Clebsch-Gordan coefficients.

The obtained differential decay rate [22] is

$$\begin{aligned} \frac{d\Gamma}{d\Omega} \propto & [c_1 \sin^2 \theta^* (\cos^2 \eta + \cos^2 \phi^* \sin^2 \eta) \\ & + c_2 \sin^2 \theta^* (\cos^2 \eta + \sin^2 \phi^* \sin^2 \eta) \\ & + c_3 \cos^2 \theta^* \sin^2 \eta + c_4 \sin 2\phi^* \sin^2 \theta^* \sin^2 \eta \\ & + \frac{1}{2} \sin 2\theta^* \sin 2\eta (c_5 \cos \phi^* + c_6 \sin \phi^*) \\ & + \lambda_\gamma (c_7 \sin^2 \theta^* \cos \eta + \sin 2\theta^* \sin \eta (c_8 \cos \phi^* + c_9 \sin \phi^*))] \end{aligned} \quad , \quad (5.18)$$

where the $d\Omega$ is the phase-space volume integrated over the m_{12}^2 corresponding to the ϕ mass squared and four angles θ^* , ϕ^* , η and unobservable angle φ . The coefficients c_{1-9} can be written as functions of four unknown parameters $r_{1,2}$ and $\delta_{1,2}$, which are given by the partial amplitude ratios $a_{1,2}/a_0 = r_{1,2} \exp(i\delta_{1,2})$, and the photon polarisation parameter λ_γ (detailed in Ref. [22]). To extract the parameter λ_γ , the four parameters $r_{1,2}$ and $\delta_{1,2}$ are required, so a three-dimensional angular fit has to be performed on the angular distributions. There are five unknown parameters to extract from nine independent angular structures.

5.5.3 Subtraction of the merged π^0 background

The background subtracted data sample using the invariant mass of $\phi K^+ \gamma$ as the discriminating variable only in the $sPlot$ method contains the contributions from the merged π^0 background. The angular distributions of the merged π^0 background are difficult to model because they are from different decay paths and the dynamics of some decays are not well known.

To extract the angular distributions of the signal only, the reconstructed B mass and γ/π^0 separation distribution are used as discriminating variables in $sPlot$ as shown in Fig. 5.27. In this two-dimensional fit, the parameters in the function describing the mass, only the yield of each component are left free in the fit. The background contributions can be either from a real photon or from a merged π^0 and both are considered. Then the fit results are reported in Table 5.4 and they are consistent with the results shown in the previous sections.

The angular distributions in the background subtracted data sample are shown in Fig. 5.28. As discussed in Section 5.4, the nonresonant three-body decay $B^+ \rightarrow \phi K^+ \gamma$ seems to be the dominant contribution. So far, the available theoretical studies are all based on the assumption that the ϕK^+ -system is a resonance with spin-parity J^P and $J \geq 1$. To perform the angular fits, the angular distributions for the nonresonant three-body decay should be taken into account.

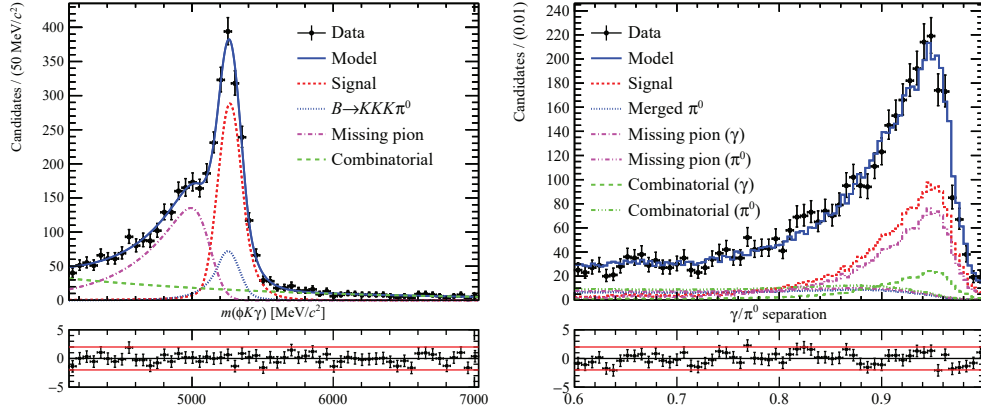


Figure 5.27: Fits on the $\phi K \gamma$ invariant mass (left) and the γ/π^0 separation variable (right) distributions.

Table 5.4: Fitted yields of each component from the two-dimensional fit on the B invariant mass and the γ/π^0 separation variable.

Component	Yield
Signal	1341 ± 53
$B \rightarrow \phi K \pi^0$	365 ± 46
Missing pion (γ)	1046 ± 58
Missing pion (π^0)	423 ± 52
Combinatorial (γ)	511 ± 50
Combinatorial (π^0)	333 ± 48

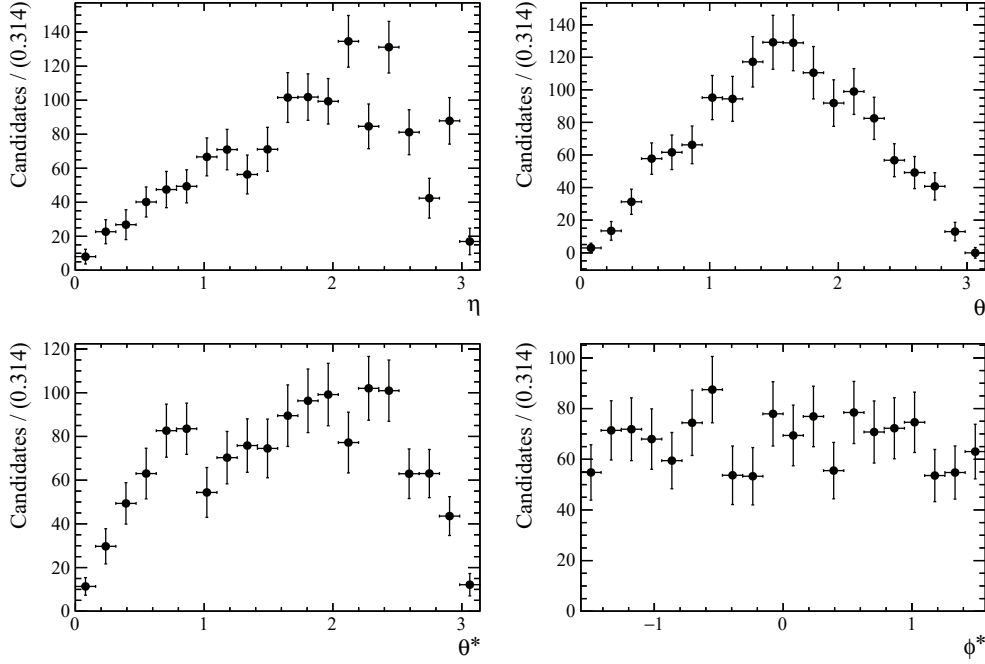


Figure 5.28: The angular distributions in the background subtracted data sample.

5.5.4 Angular acceptance

The LHCb detector acceptance and the reconstruction and selection introduce an angular dependent efficiency, also called angular acceptance. If the angles are independent, the acceptance can be factorised in the three angles η , θ^* and ϕ^* as

$$\epsilon(\eta, \theta^*, \phi^*) = \epsilon(\eta) \times \epsilon(\theta^*) \times \epsilon(\phi^*), \quad (5.19)$$

where $\epsilon = \frac{\text{candidates reconstructed and selected in simulation}}{\text{all signal candidates produced in simulation}}$ in bins of the corresponding angle.

The acceptances in the simulated $B^+ \rightarrow \phi K^+ \gamma$ sample for the angles are shown in Fig. 5.29 by assuming they are generated independently. The acceptance of each angle is fitted to Legendre polynomials truncated at order 4 due to the statistics of the sample.

$$P(x) = 1 + c_1 x + c_2 \frac{1}{2} (3x^2 - 1) + c_3 \frac{1}{2} (5x^3 - 3x) + c_4 \frac{1}{8} (35x^4 - 30x^2 + 3) \quad (5.20)$$

where x means $\cos \eta$, $\cos \theta^*$ or $\sin \phi^*$ which satisfies $x \in [-1, 1]$. As an alternative strategy, the distributions in Fig. 5.29 can directly be used in the angular fit to model the acceptances.

5.5.5 Summary

In the $B^+ \rightarrow \phi K^+ \gamma$ decay, the photon polarisation could be measured from the angular distributions of the final state. To be able to probe the polarisation of the emitted photons,

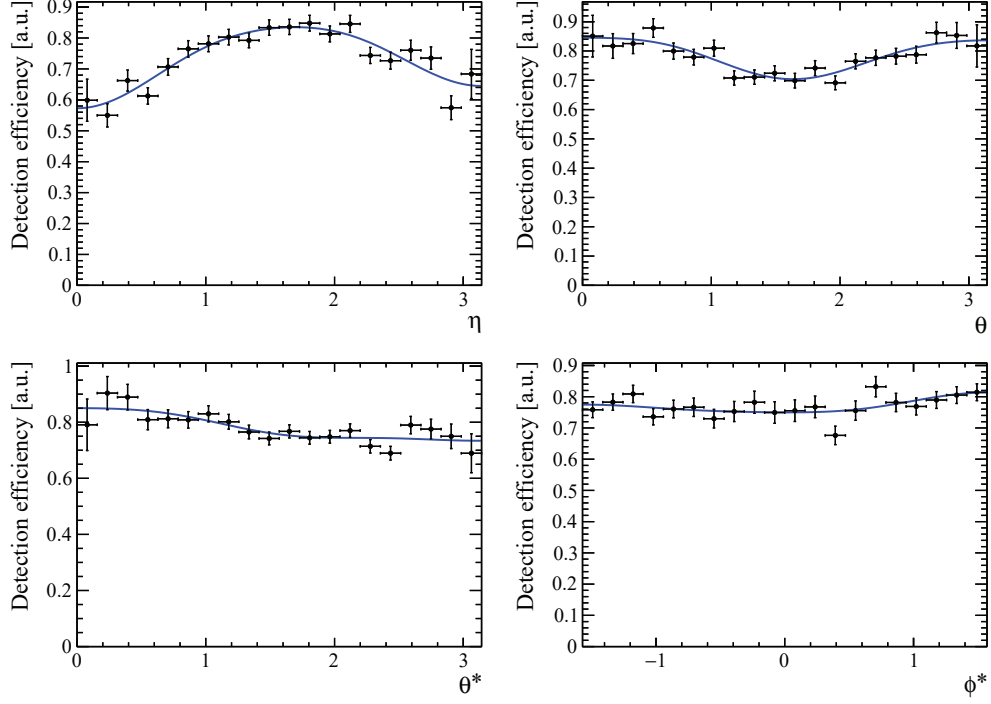


Figure 5.29: The angular acceptances for angles η , θ , θ^* and ϕ^* from the simulated sample. The blue curves are the fits to polynomials.

the ϕK^+ -system is required to be a resonance with $J \geq 1$ and there must be interferences between the different partial waves in the ϕK^+ -system. Studies on the hadronic structures of the ϕK^+ -system suggest that the dominant contribution in the $B^+ \rightarrow \phi K^+ \gamma$ decay could be the nonresonant three-body decay, hence the possibility to measure the photon polarisation in the current theoretical framework is small.

To perform a fit on the angular distributions in the $B^+ \rightarrow \phi K^+ \gamma$ data sample, there are no experimental issues remained in the analysis as discussed in the previous sections. The main challenge is to understand the angular distributions for the nonresonant three-body decays $B^+ \rightarrow \phi K^+ \gamma$.

5.6 Conclusion

Merged π^0 background is the main experimental difficulty for the selection of signal candidates. The strategy proposed in this thesis to use the γ/π^0 separation variable can effectively separate the signal radiative B decays with real photons from the backgrounds with merged π^0 s.

The direct CP asymmetry of the $B^+ \rightarrow \phi K^+ \gamma$ decay amplitudes is measured to be

$$A_{CP}(B^+ \rightarrow \phi K^+ \gamma) = (1.6 \pm 2.1(\text{stat.}) \pm 0.7(\text{syst.}))\%. \quad (5.21)$$

Chapter 5. CP violation in $B^+ \rightarrow \phi K^+ \gamma$ decays

This is the most precise measurement in this decay so far and the value is consistent with the SM prediction.

The first attempt to look into angular distributions in this decay is presented. In order to extract λ_γ from this method, there must be interferences between the different partial waves in the vector state ϕK^+ -system. The studies performed in this thesis and the previous studies done by the Belle collaboration show that in the ϕK^+ invariant mass spectra, there is no clear evidence for the existence of resonances. Thus, the chance of measuring the photon polarisation in this decay is slim.

6 Reconstruction of $B^+ \rightarrow \phi K^+ \gamma$ decays with converted photons

About 20% of the photons convert into electron-positron pairs at LHCb before the magnet. These electron-positron pairs are separated when traversing the magnetic field and reconstructed by the tracking system. The converted photons offer a much better resolution than the calorimetric photons because of the good tracking resolution.

6.1 Reconstruction of the converted photons

Converted photons are reconstructed from two oppositely charged electrons. Depending on the position where the conversion occurred, the photons are built either using the e^+ and e^- reconstructed as downstream tracks (DD) or as long tracks (LL) [123]. In the case of a photon converted in the VELO with too few VELO hits for long track reconstruction (mainly downstream end of the VELO) and in the first tracking station upstream of the magnet (TT), the converted photon is reconstructed using downstream tracks only; if the conversion occurred mainly in VELO with sufficient VELO hits for the reconstruction of long tracks, the converted photons are reconstructed using long tracks only. Other cases such as one track reconstructed as long track and the other the downstream track are not considered in this study.

Candidate e^+e^- pairs are required to be within the ECAL acceptance and to deposit energies in ECAL with reconstructed electromagnetic clusters having compatible y positions with impact point of the e^+ and e^- tracks. Then, a bremsstrahlung correction is applied to each electron track. Any photon with a position in the ECAL compatible with a straight line extrapolation of the electron track from the associated hit in the TT station is selected and its energy is added to the electron energy from the reconstructed track. If the same bremsstrahlung candidate is found for both the e^+ and the e^- of the pair, the photon energy is added randomly to one of the tracks. The bremsstrahlung corrected e^+ and e^- tracks are extrapolated backward to determine the conversion point and a vertex fit is performed to reconstruct the photon.

The effect of the magnetic field needs to be taken into account properly during the extrapolation. In the case of DD, the two daughters from the converted photon are almost aligned and

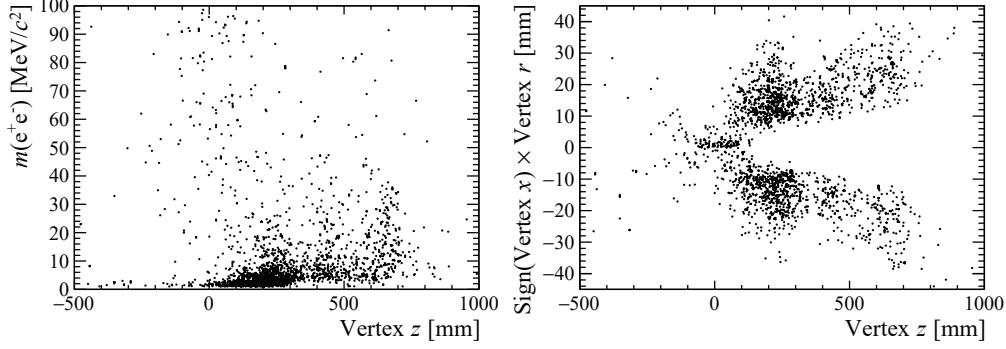


Figure 6.1: The reconstructed invariant mass of the converted photons versus the reconstructed z positions (left) and the r -coordinate of the conversion point versus its z position (right) in simulated $B^+ \rightarrow K^+ K^+ K^- \gamma$ sample using long tracks.

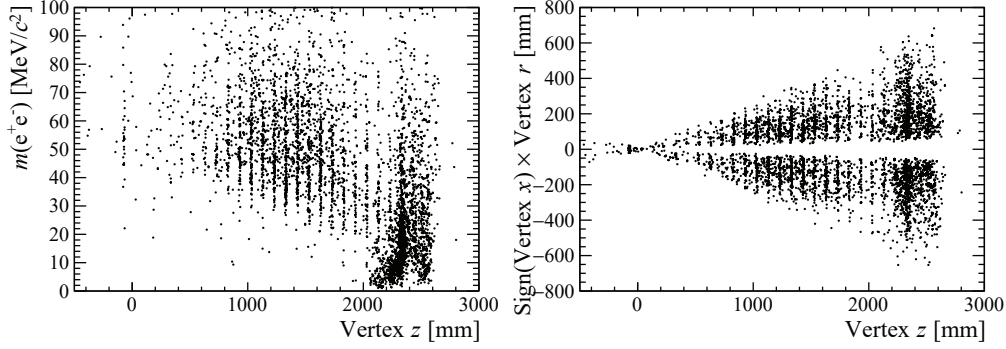


Figure 6.2: The reconstructed invariant mass of the converted photons versus the reconstructed z positions (left) and the r -coordinate of the conversion point versus its z position (right) in simulated $B^+ \rightarrow K^+ K^+ K^- \gamma$ sample using downstream tracks.

the vertex fit cannot converge properly without a well defined vertex. In this case, the tracks are extrapolated from TT towards $z = 0$ (nominal pp interaction point) in steps of 100 mm. At the position where the two tracks are closest, is found and the distance between the two tracks is small enough, this position is considered as the conversion point. The reconstructed invariant mass of the converted photon and the r -coordinate of its conversion point versus the z position of the conversion point in both LL and DD cases are shown in Figs. 6.1 and 6.2 in the simulated $B^+ \rightarrow K^+ K^+ K^- \gamma$ sample, respectively.

The efficiency of converted and reconstructed photons is studied by reconstructing π^0 mesons, with either two calorimetric photons or one calorimetric photon and one converted photon [124]. The ratio of efficiencies of converted photons to calorimetric photons is measured in data and simulation as a function of photon p_T as shown in Fig. 6.3.

The invariant mass and the p_T distributions of the reconstructed photons are shown in Fig. 6.4 using the simulated $B^+ \rightarrow \phi K^+ \gamma$ and $B^+ \rightarrow \phi K^{*0}$ samples. The invariant mass and p_T distributions of the reconstructed B candidates in the simulated $B^+ \rightarrow \phi K^+ \gamma$ and $B^+ \rightarrow \phi K^{*0}$ samples

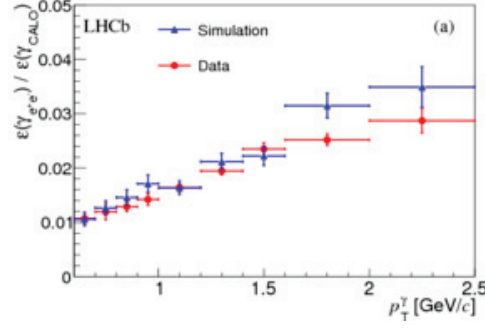


Figure 6.3: The ratio of efficiencies of converted photons to calorimetric photons measured in data (red circles) and simulation (blue triangles) as a function of photon p_T from Ref. [124].

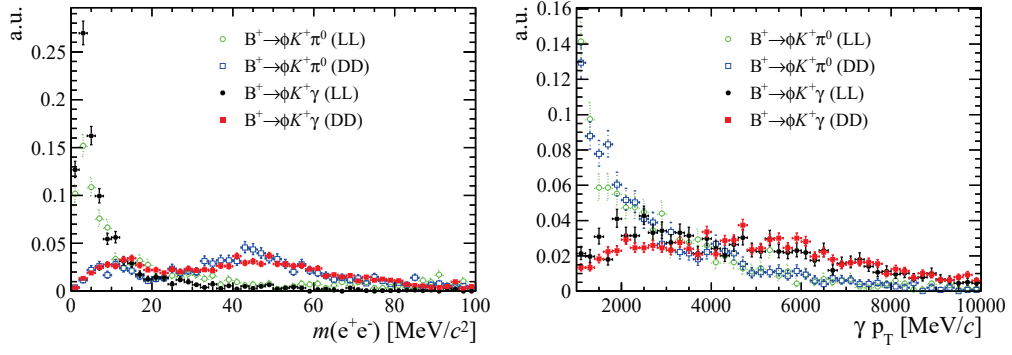


Figure 6.4: Distributions of the reconstructed invariant mass (left) and p_T (right) of the converted photons in the simulated $B^+ \rightarrow \phi K^+ \gamma$ and $B^+ \rightarrow \phi K^* \pi^0$ samples.

are displayed in Fig. 6.5.

6.2 STRIPPING and trigger selections

The STRIPPING line selects three charged tracks and combines them with a converted photon. The selections applied in the STRIPPING line are documented in Table A.4. As seen from the reconstructed B^+ mass distributions in Fig. 6.5, the advantage of using converted photons is that the better resolution of the reconstructed B mass offers better discriminating power in separation of the background in $B^+ \rightarrow K^+ K^+ K^- \gamma$ decays coming from $B^+ \rightarrow K^+ K^+ K^- \pi^0$ decays. The mass resolution on the reconstructed B candidates is worse in the long tracks case due to the worse energy resolution of the reconstructed photons mainly resulting from the difficulty in recovering the bremsstrahlung loss for the electrons.

The signal candidates must be selected with either one of the three L0 trigger lines [55] defined below fired:

- **L0E**: events triggered by at least one of the electrons in the signal candidate (L0Electron_TOS);
- **L0H**: events triggered by at least one of the hadrons in the signal candidate and not by

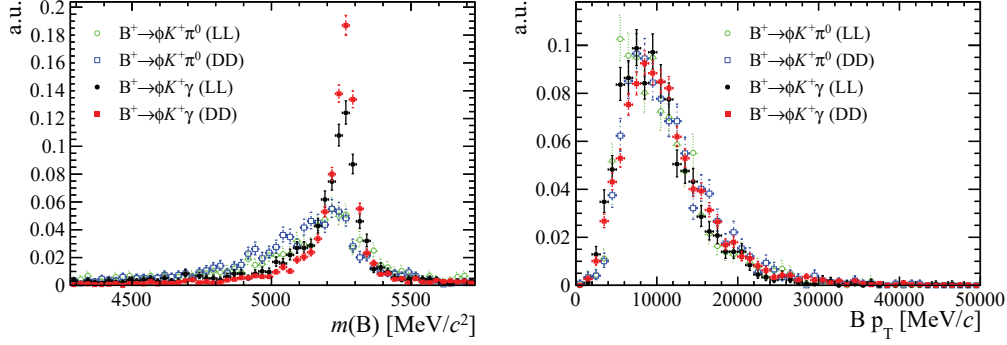


Figure 6.5: Distributions of the invariant mass (left) and p_T (right) of the reconstructed B candidates in the simulated $B^+ \rightarrow \phi K^+ \gamma$ and $B^+ \rightarrow \phi K^{*0}$ samples.

the electron (L0Hadron_TOS and not L0Electron_TOS);

- **L0I**: events triggered by particles not in the signal candidate and not by the previous two cases (L0Global_TIS and not L0Hadron_TOS and not L0Electron_TOS).

TOS (trigger on signal) events are triggered by a given line on the signal itself, independently of the rest of the event. The TOS criterion is satisfied if all of the tracks and calorimeter objects of the trigger have overlap with the ones to reconstruct the signal. TIS (trigger independent of signal) events are triggered by a given line independently of the signal, only due to the rest of the event. In order for an event to be TIS, there must exist at least one trigger object which does not overlap with the signal.

The transverse momentum p_T of the photon and the reconstructed $K^+ K^+ K^-$ invariant mass distributions are shown in Fig. 6.6 using the simulated sample Bu2KKKGamma split into different L0 trigger categories. The **L0E** trigger has higher efficiency to reconstruct the higher momentum photons whilst the other two lines perform better at relatively lower momentum region.

6.3 Offline selections

The candidates are further refined with offline cuts, and the preselections discussed in Chapter 5 are adopted in this chapter apart from the selections related to the photon and its conversion daughters. Converted photons are reconstructed from a loose selection of electron tracks, which is further tightened by requiring $\text{GhostProb} < 0.4$ and $\text{ProbNNe} > 0.2$, where GhostProb is the probability of a track being a fake track (these tracks arise from combinations of unrelated hits which pass the track reconstruction quality requirements).

A gradient boosted decision trees based on Scikit-learn [117] is applied to separate the signal candidates from the combinatorial background. The classifier is trained and tested using the simulated $B^+ \rightarrow K^+ K^+ K^- \gamma$ sample for signal and the upper sideband of the B invariant mass distribution in the range of $[6000, 7000] \text{ MeV}/c^2$ from data for background. The selected

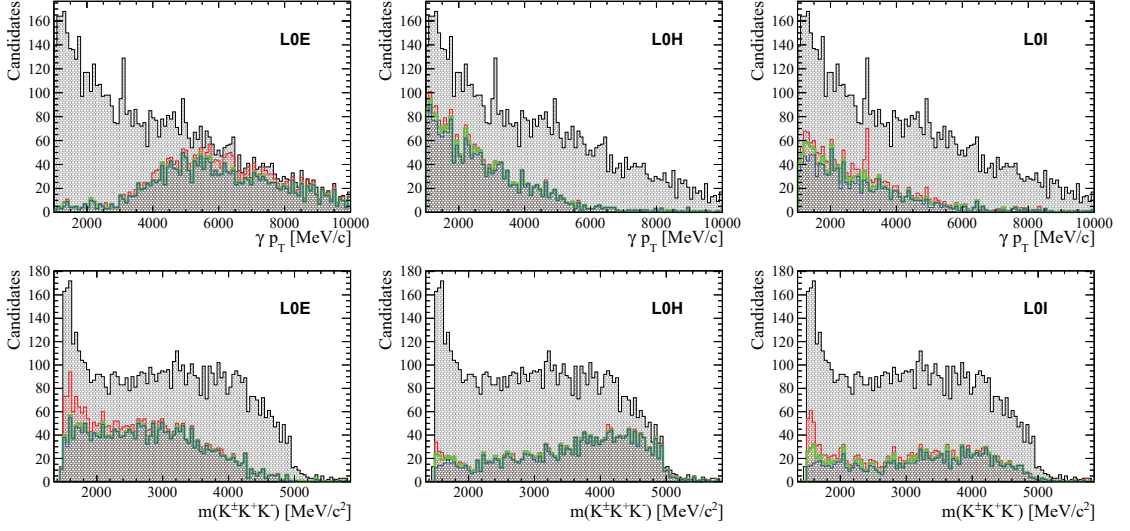


Figure 6.6: The p_T distribution of the converted photons (top) and the invariant mass distribution of the $K^+ K^+ K^-$ -system reconstructed in the simulated $B^+ \rightarrow K^+ K^+ K^- \gamma$ sample with **LOE** (left), **LOH** (middle) and **LOI** (right) fired. The order of the selections applied is the STRIPPING selections (gray), the L0 trigger (red), the HLT1 trigger (green) and the HLT2 trigger (blue).

number of signal candidates in the simulated sample is 1663 for LL and 2223 for DD. The total statistics of the combinatorial background candidates in the chosen sideband range is around an order of 10 times larger than the simulated signal samples. A dataset with 3000 candidates for LL and DD each is randomly chosen from data in the sideband region. About 2/3 of the sample is used as the training and validation sample whilst the remaining 1/3 of the data is reserved as a test sample.

Compared to the analysis using calorimetric photons in Chapter 5, the statistics of the signal and background samples in this analysis is an order of magnitude lower. Therefore, care is taken to maximise the separation power of the BDT given the limited sample sizes by using the k -fold approach [125]. The training and validation sample is randomly split into k sub-samples with approximately an equal amount of events in each sample. The stratified k -fold technique is used to split the samples where each set contains approximately the same percentage of candidates of each target class as the complete set, *i.e.* signal and background. The classifier is trained and optimised by cycling through training k times with one sub-sample left out for validation and $k - 1$ sub-samples used for training. The average output from the k trials is then tested on the reserved test sample and applied to data.

A total of k ($k = 10$ in the analysis presented here) BDTs are trained for both DD and LL samples. The BDT performance as a function of the background rejection and the signal efficiency from different cuts and their response distributions on the reserved test samples with the separation between signal and background are shown in Fig. 6.7 and Fig. 6.8 for DD and LL, respectively. The testing samples and training samples are overlaid on the BDT response distributions to check overtraining. Since the main purpose of this study is to perform an estimation of the

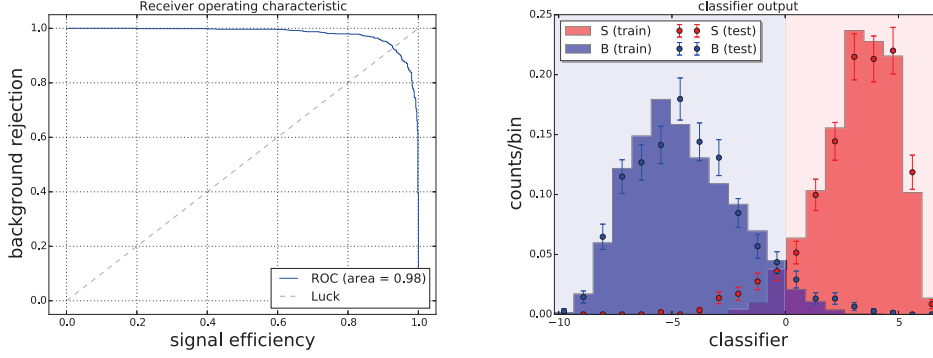


Figure 6.7: The ROC curve (left) and the BDT response distribution (right) of the average of the 10 BDTs on the reserved test sample for DD.

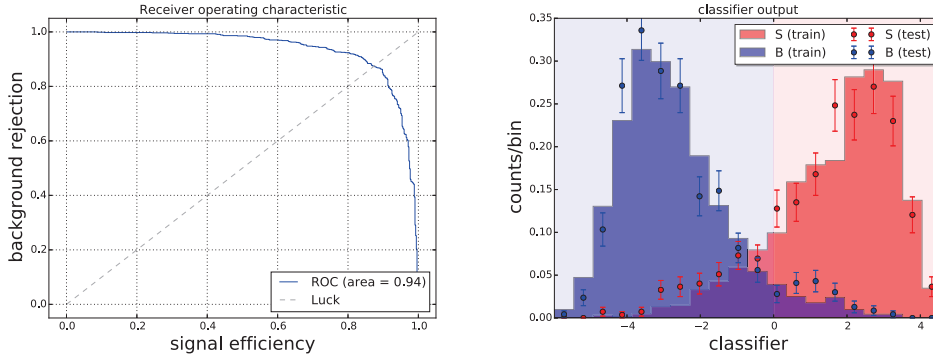


Figure 6.8: The ROC curve (left) and the BDT response distribution (right) of the average of the 10 BDTs on the reserved test sample for LL.

statistics of the selected signal candidates using the converted photons, a slight overtraining observed in the DD case is acceptable at this stage.

The BDT and PID criteria for the kaon identifications are optimised using the same procedure described in Chapter 5. The signal mass region is chosen to be within ± 3 standard deviations of the B^+ mass, where the resolution is assumed to be $40 \text{ MeV}/c^2$ for LL case and $25 \text{ MeV}/c^2$ for DD case based on fits to the simulated $B^+ \rightarrow K^+ K^+ K^- \gamma$ sample. The simulated $B^+ \rightarrow \phi K^+ \gamma$ sample is used as the signal sample for the optimisation of the BDT and PID cuts. To estimate the background contributions in the defined B^+ signal region, an exponential function is used to fit the reconstructed B^+ invariant mass distribution in data in the range of $[7000, 8000] \text{ MeV}/c^2$ and then extrapolated to the signal region. The criterion $\text{ProbNNK} \times (1 - \text{ProbNN}\pi)$ performs better than the criterion ProbNNK in the background rejection. The optimised cuts are $\text{BDT} > 0$ and $\text{ProbNNK} \times (1 - \text{ProbNN}\pi) > 0.3$ (see Chapter 4 for definitions of ProbNNK and $\text{ProbNN}\pi$) for DD and $\text{BDT} > 1$ and $\text{ProbNNK} \times (1 - \text{ProbNN}\pi) > 0.1$ for LL with the figure of merit in 2D shown in Fig. 6.9. The figure of merit and signal efficiency and purity as a function of the BDT cut and PID cut at the optimal point are shown in Fig. 6.10 for

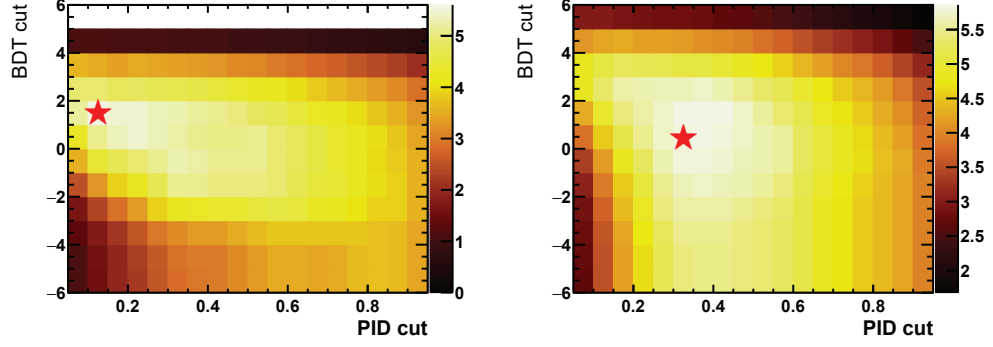


Figure 6.9: Figure of merit for LL (left) and DD (right) in bins of the BDT output and the kaon PID cut. The symbol ★ indicates the maximal figure of merit.

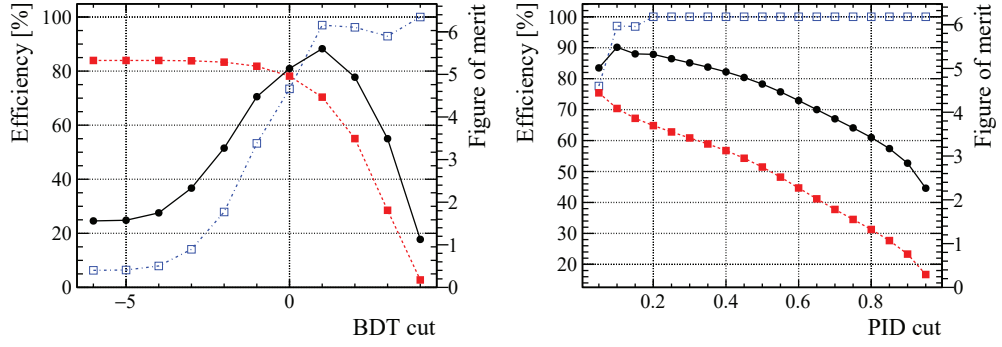


Figure 6.10: The curves of the figure of merit (black dots, right axis), signal efficiency (red full squares) and purity (blue open squares) as a function of the BDT cut with $\text{ProbNNK} \times (1 - \text{ProbNN}\pi) > 0.1$ applied (left) and as a function of the PID cut with $\text{BDT} > 1$ applied (right) for LL.

LL and in Fig. 6.11 for DD.

6.4 Background from partially reconstructed B decays

The HOP method introduced in Chapter 5 is used to further suppress the backgrounds from partially reconstructed B decays. The cuts are chosen to be $a_{\text{HOP}} = 4000 \text{ MeV}/c^2$ and $b_{\text{HOP}} = 100$ for the LL sample and $a_{\text{HOP}} = 3800 \text{ MeV}/c^2$ and $b_{\text{HOP}} = 110$ for the DD sample. The criteria are determined to maximise the signal selection efficiencies (which at least should be larger than 95%) whilst the background rejection should be kept as high as possible. The distributions of M_{HOP}^B versus χ_{FD}^2 in data are shown in Fig. 6.12, where the black vertical dotted line indicates the selection applied. Based on studies from simulated samples shown in Fig. 6.13 where the distributions with and without applying the HOP cut are overlaid for comparison, the HOP cuts do not affect the B invariant mass distributions.

The invariant mass distributions of the reconstructed B candidates with and without the HOP

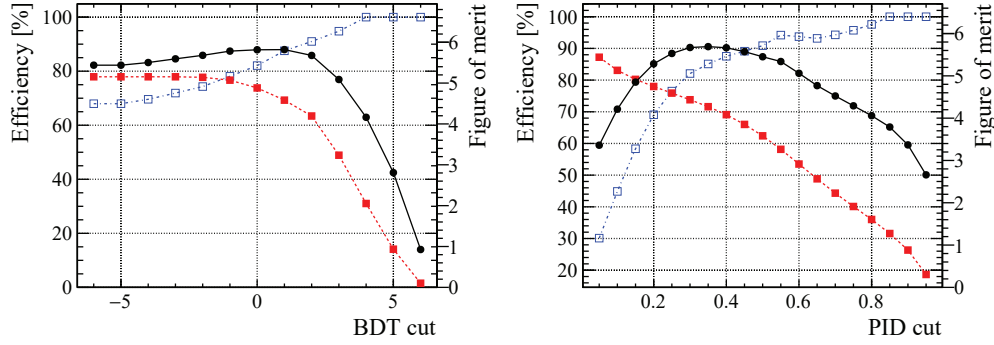


Figure 6.11: The curves of the figure of merit (black dots, right axis), signal efficiency (red full squares) and purity (blue open squares) as a function of the BDT cut with $\text{ProbNNK} \times (1 - \text{ProbNN}\pi) > 0.3$ applied (left) and as a function of the PID cut with $\text{BDT} > 0$ applied (right) for DD.

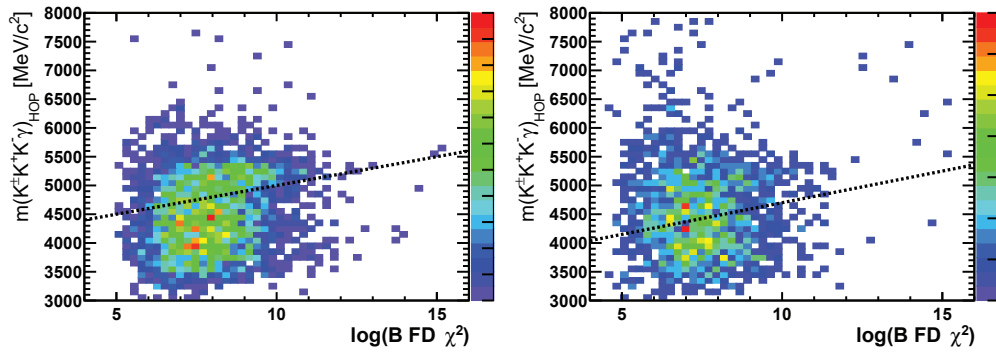


Figure 6.12: The distribution of M_{HOP}^B versus the B flight distance χ^2 in data for LL (left) and DD (right).

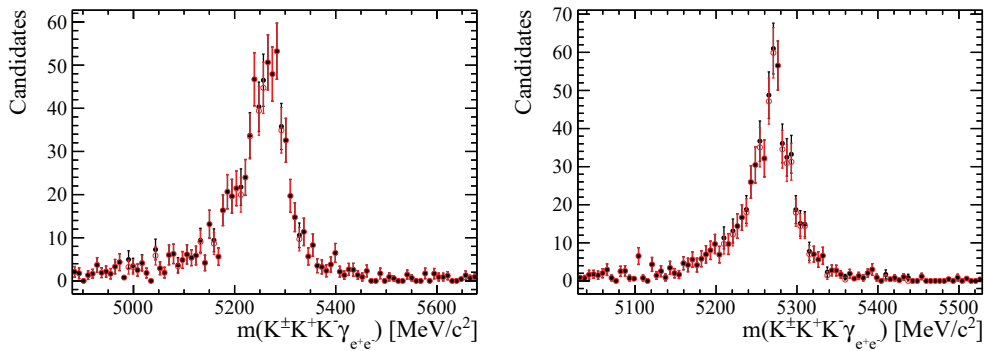


Figure 6.13: The reconstructed B invariant mass distributions for LL (left) and DD (right) in the simulated $B^+ \rightarrow K^+ K^+ K^- \gamma$ sample before (black dots) and after (red circles) applying HOP cut.

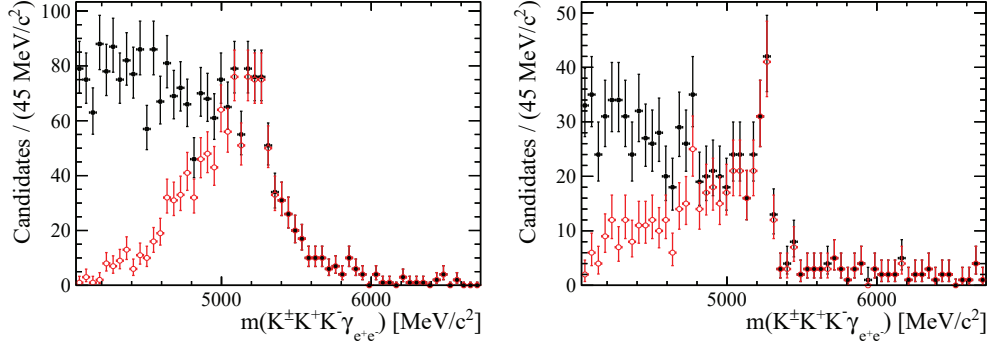


Figure 6.14: The reconstructed B invariant mass distributions for LL (left) and DD (right) in data before (black dots) and after (red circles) applying the HOP cut.

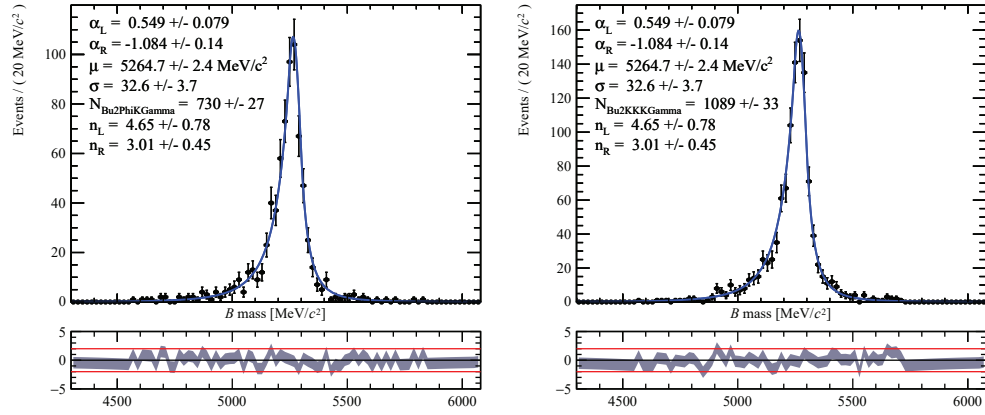


Figure 6.15: Fit of the invariant mass of $K^+K^+K^-\gamma_{e^+e^-}$ in the simulated samples of $B^+ \rightarrow K^+K^+K^-\gamma$ (left) and $B^+ \rightarrow \phi K^+ \gamma$ (right) where the e^+e^- pairs of the converted photons are both long tracks.

cut are shown in Fig. 6.14 in data. The HOP method efficiently suppresses the background from partially reconstructed B decays and in the mean time introduces negligible effect on the signals.

6.5 Signal and background models

The signal lineshapes are described using the double-tail Crystal Ball function with parameters determined from simulation. An unbinned maximum likelihood fit is performed on the simulated $B^+ \rightarrow K^+K^+K^-\gamma$ and $B^+ \rightarrow \phi K^+ \gamma$ samples simultaneously. The results of the mass fits are shown in Fig. 6.15 and Fig. 6.16 for LL and DD, respectively. The photons converted early in the detector traverse more material, thus experience more energy loss due to bremsstrahlung, and therefore the resolution for B candidates made with LL photons is worse.

The background coming from $B^+ \rightarrow K^+K^+K^-\pi^0$ decays contributes to the B^+ signal region

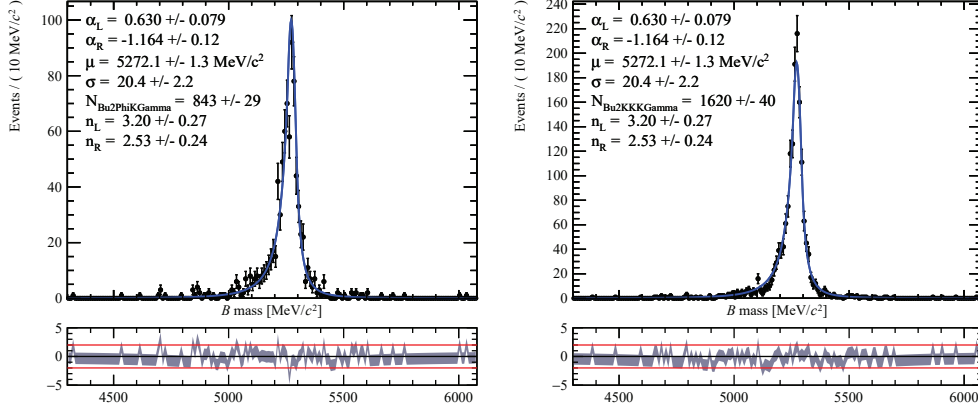


Figure 6.16: Fit of the invariant mass of $K^+ K^+ K^- \gamma e^+ e^-$ in the simulated samples of $B^+ \rightarrow K^+ K^+ K^- \gamma$ (left) and $B^+ \rightarrow \phi K^+ \gamma$ (right) where the $e^+ e^-$ pairs of the converted photons are both downstream tracks.

of the $B^+ \rightarrow K^+ K^+ K^- \gamma$ decays, when one of the two photons from the π^0 decay converts and is reconstructed and the other photon is missing. The mass shape of the reconstructed B^+ invariant mass distribution from this background is fixed from the simulated samples. A double-tail Crystal Ball function is used to fit the reconstructed B^+ mass distributions. An unbinned maximum likelihood fit is performed simultaneously on the three simulated samples of decays $B^+ \rightarrow \phi K^{*+}$, $B^+ \rightarrow \phi K_2^*(1430)^+$ and $B^+ \rightarrow \phi K^*(1680)^+$ to maximise the statistics of the simulated samples. The fit results on the simulated samples are shown in Fig. 6.17.

After the cut on the HOP variable, partially reconstructed B decays with one missing particle still contribute to the background. Two simulated samples of $B^0 \rightarrow \phi K^{*0} \gamma$ decays and $B_s^0 \rightarrow \phi \phi \gamma$ decays are used to determine the shapes of the reconstructed B invariant mass distributions from these backgrounds. The ARGUS function (Eq. 4.7) convolved with a resolution Gaussian function is used to describe the reconstructed $K^+ K^+ K^- \gamma e^+ e^-$ invariant mass distributions. The fit results are shown in Fig. 6.18 for the simulated $B^0 \rightarrow \phi K^{*0} \gamma$ sample and in Fig. 6.19 for the simulated $B_s^0 \rightarrow \phi \phi \gamma$ sample.

6.6 Fit of the B invariant mass distributions

To estimate the number of selected $B^+ \rightarrow K^+ K^+ K^- \gamma$ candidates, a fit is performed on the reconstructed B invariant mass spectra. The signal and background models are fixed from the simulation except the mean value of the B invariant mass.

The reconstructed and selected signal candidates using long-long tracks suffer from higher background contributions from partially reconstructed B decays due to the particle misidentifications but have low contributions from the combinatorics. The kaon identification criteria optimised on the combinatorial background are not sufficient to reduce the backgrounds with

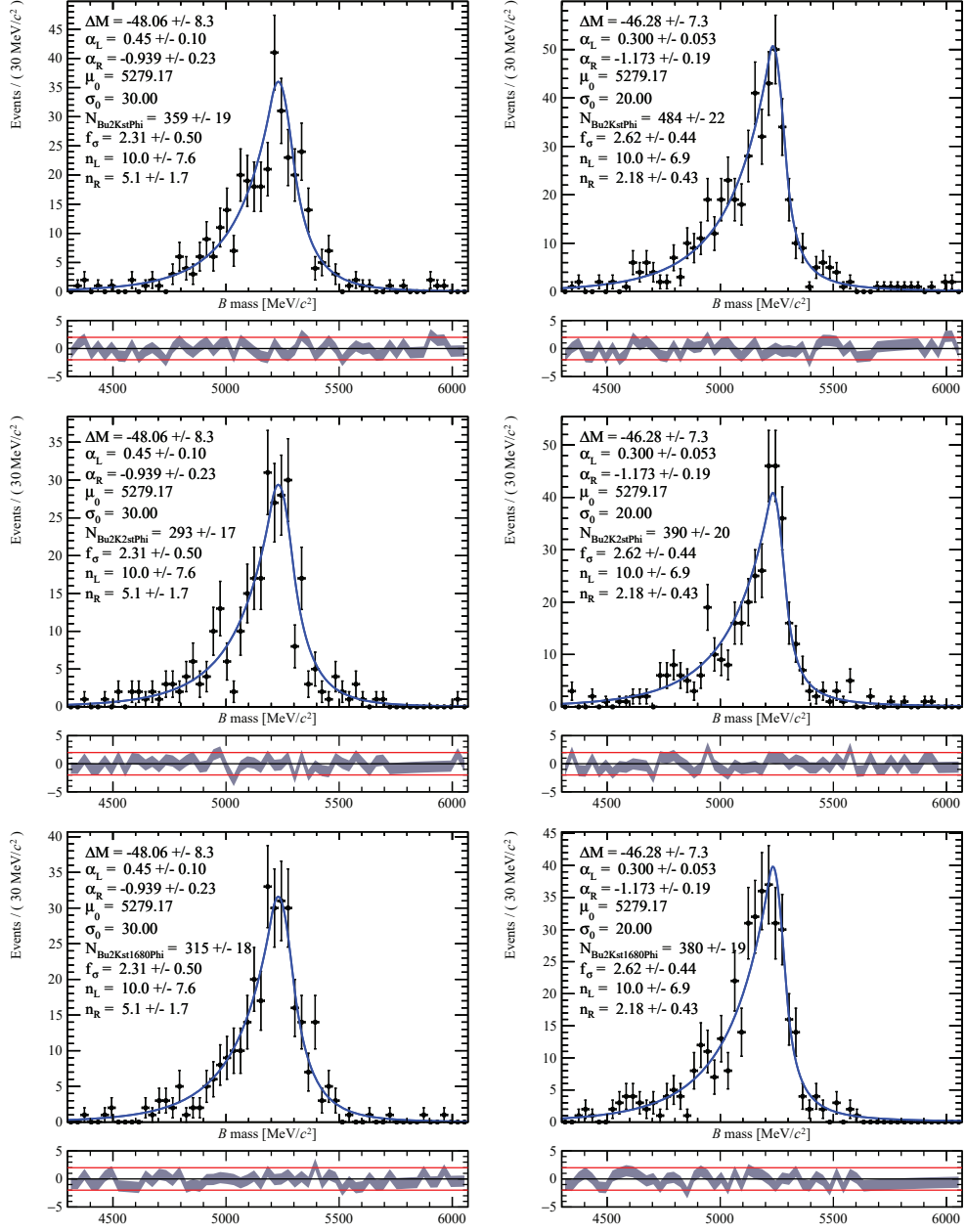


Figure 6.17: Fit of the invariant mass of $K^\pm K^+ K^- \gamma e^+ e^-$ from simulated $B^+ \rightarrow \phi K^{*+}$, $B^+ \rightarrow \phi K_2^{*+}(1430)^+$ and $B^+ \rightarrow \phi K^*(1680)^+$ samples, where the $e^+ e^-$ pairs of the converted photons are both long tracks shown on the left and downstream tracks on the right.

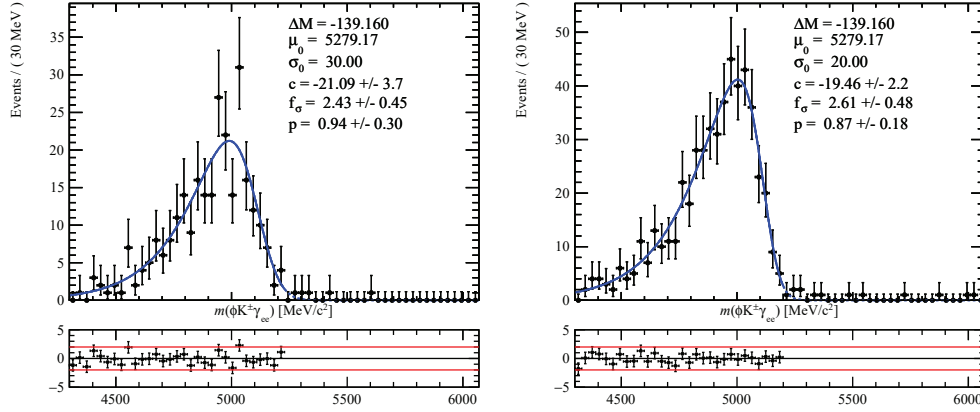


Figure 6.18: The reconstructed $K^\pm K^+ K^- \gamma_{e^+ e^-}$ invariant mass distributions in the simulated $B^0 \rightarrow \phi K^{*0} \gamma$ sample for LL (left) and DD (right) cases.

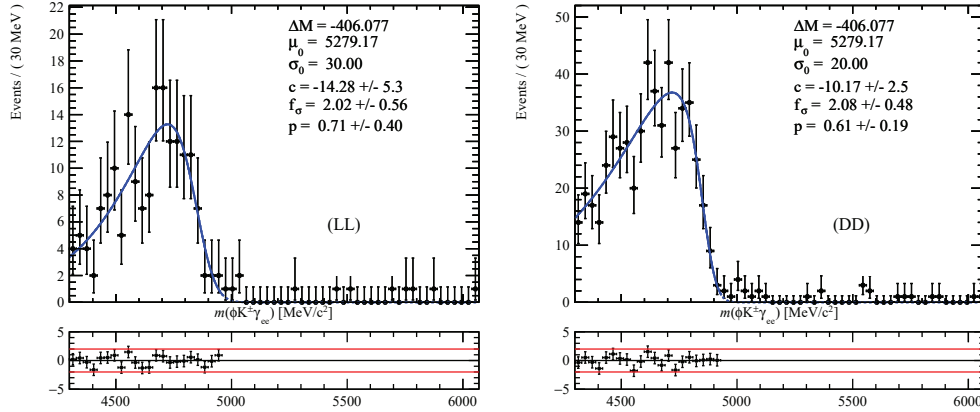


Figure 6.19: The reconstructed $K^\pm K^+ K^- \gamma_{e^+ e^-}$ invariant mass distributions in the simulated $B_s^0 \rightarrow \phi \phi \gamma$ sample for LL (left) and DD (right) cases.

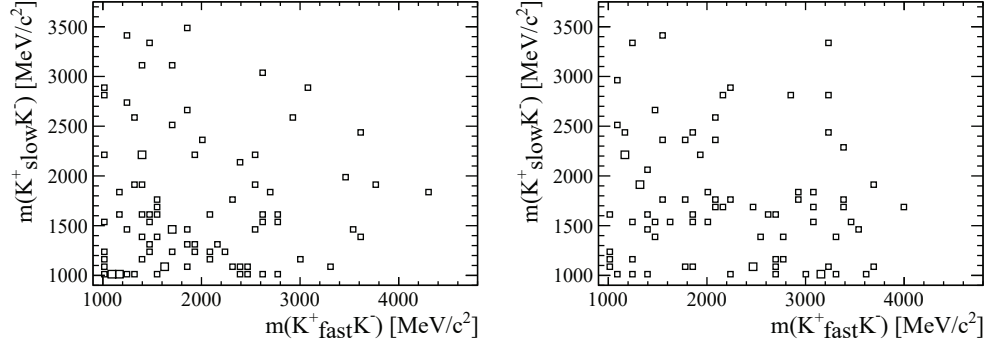


Figure 6.20: The reconstructed $K^+_{\text{slow}} K^-$ invariant mass versus the $K^+_{\text{fast}} K^-$ invariant mass distributions in data from LL (left) and DD (right).

one or more tracks misidentified especially from pions. To perform the mass fit, the kaon identification criteria are tightened to be $\text{ProbNNK} \times (1 - \text{ProbNN}\pi) > 0.3$ for the LL sample to further suppress the background due to particle misidentifications.

The selected $B^+ \rightarrow K^+ K^+ K^- \gamma$ candidates include decay paths of $B^+ \rightarrow \phi K^+ \gamma$, $B^+ \rightarrow \bar{D}^{*0}(\bar{D}^0 \gamma) K^+$, nonresonant $B^+ \rightarrow K^+ K^+ K^- \gamma$. The reconstructed $K^+ K^-$ invariant mass distributions are shown in Fig. 6.20 in the defined signal regions for both LL and DD, where the contributions from $B^+ \rightarrow \phi K^+ \gamma$ can be clearly seen.

The invariant mass fits of the reconstructed $K^+ K^+ K^- \gamma_{e^+ e^-}$ invariant mass distributions on the selected data samples are shown in Fig. 6.21 with the fit parameters reported in Table 6.1. The likelihood profiles as a function of the fitted signal yields (N_{Signal}) are shown in Fig. 6.22, obtained by minimising the likelihood at each value of N_{Signal} . The number of signal candidates determined from the fits are 0 ± 56 and 53 ± 17 with the uncertainties purely statistical for LL and DD, respectively.

There are 1363 ± 46 signal $B^+ \rightarrow \phi K^+ \gamma$ decays fitted from the data using the calorimetric photons in Chapter 5. About 20% of all photons convert before the magnetic field. These photons are then reconstructed with an efficiency of $\sim 5\%$, where the value is estimated from the ratio of efficiencies in Fig. 6.3 and the photon p_T distributions shown in Fig. 6.4. The number of signal $B^+ \rightarrow \phi K^+ \gamma$ decays reconstructed from converted photons is estimated to be 17 ± 9 , where the main contribution to the uncertainty is from the ratio of efficiencies of converted photons to calorimetric photons that is assigned to be 50%. In addition, we assume the ratio $\mathcal{B}(B^+ \rightarrow \phi K^+ \gamma) / \mathcal{B}(B^+ \rightarrow K^+ K^+ K^- \gamma)$ the same as the one $\mathcal{B}(B^+ \rightarrow \phi K^+) / \mathcal{B}(B^+ \rightarrow K^+ K^+ K^-) \sim 0.26$. Therefore, the expected number of $B^+ \rightarrow K^+ K^+ K^- \gamma$ decays is 65 ± 41 , which is consistent with the fitted results.

With the converted photons, there is a good discrimination power of background from the decays with π^0 s using the mass fit of the reconstructed B invariant mass spectra. Due to the low conversion and reconstruction efficiency of the converted photons, the statistics of the reconstructed signal candidates is too low to perform any further studies.

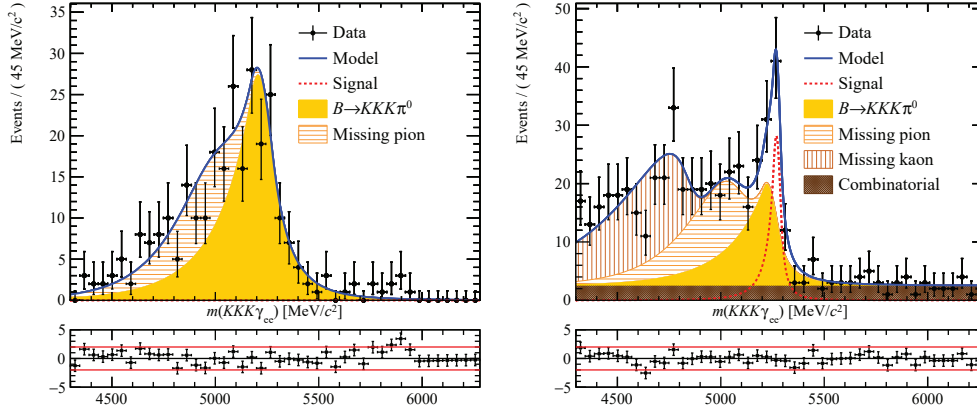


Figure 6.21: Fit of the invariant mass of $K^+ K^+ K^- \gamma e^+ e^-$ in data where the $e^+ e^-$ pairs of the converted photons are either both long tracks (left) or both downstream tracks (right).

Table 6.1: Fit parameters on the selected $B^+ \rightarrow K^+ K^+ K^- \gamma e^+ e^-$ data samples for LL (second column) and DD (third column), respectively. The sign “–” means the contribution from the component is negligible.

Parameter	LL	DD
μ (MeV/ c^2)	5254.1 ± 13.9	5268.7 ± 5.4
N_{Signal}	0 ± 56	53 ± 17
$N_{B \rightarrow K^+ K^+ K^- \pi^0}$	197 ± 21	113 ± 30
$N_{\text{Missing pion}}$	79 ± 18	100 ± 22
$N_{\text{Missing kaon}}$	–	152 ± 17
$N_{\text{Combinatorial}}$	–	110 ± 17

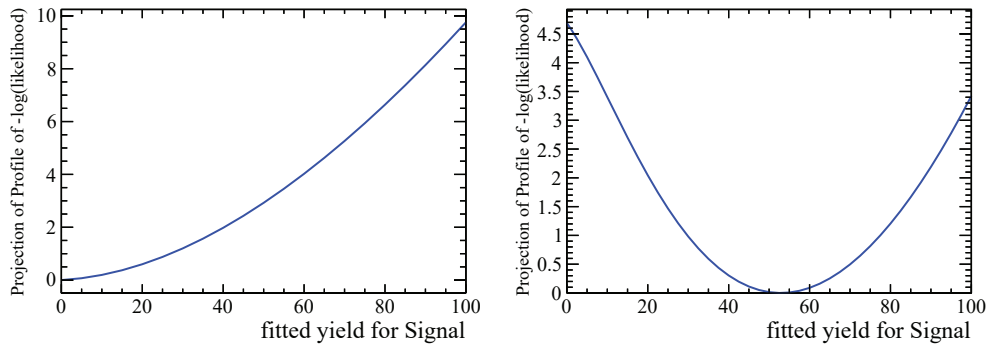


Figure 6.22: Likelihood profiles as a function of the fitted signal yields for LL (left) and DD (right) in data.

6.7 Conclusion

To conclude, with the converted photons, there is a good discrimination of the decays with π^0 s and the decays with photons using the mass fit of the reconstructed B^+ mass. But due to the low statistics of the current data sample, it is difficult to perform further precision measurements in the $B^+ \rightarrow K^+ K^+ K^- \gamma$ decays using converted photons.

7 Conclusions

This thesis work is exploring the measurements of the photon polarisation in $B_s^0 \rightarrow \phi\gamma$ and $B^+ \rightarrow \phi K^+ \gamma$ decays at LHCb. These rare B decays are mediated through loop level diagrams, where heavy particles introduced by models beyond the SM could contribute to the loop. The polarisation of the emitted photons in $b \rightarrow s\gamma$ transitions can indicate us whether there are contributions from new physics. The branching fractions of the two decay modes are measured previously [39] to be

$$\begin{aligned}\mathcal{B}(B_s^0 \rightarrow \phi\gamma) &= (3.52 \pm 0.34) \times 10^{-5}, \\ \mathcal{B}(B^+ \rightarrow \phi K^+ \gamma) &= (2.7 \pm 0.4) \times 10^{-6}.\end{aligned}\tag{7.1}$$

Using the full data set of about 3 fb^{-1} collected with the LHCb detector during Run I in the year of 2011 at the centre-of-energy $\sqrt{s} = 7 \text{ TeV}$ and the year of 2012 at $\sqrt{s} = 8 \text{ TeV}$, the two decay modes are analysed.

In the SM, the predominant left-handedness of the photons in the $B_s^0 \rightarrow \phi\gamma$ decay results in a small A^Δ value which is related to the amount of the “wrongly”-polarised photons, and the SM prediction is $A_{\text{SM}}^\Delta = 0.047^{+0.029}_{-0.025}$ [35]. To measure the A^Δ value in this decay, an untagged time-dependent analysis is performed. The number of signal candidates determined from the B invariant mass fit is 4072 ± 112 after the background subtraction, where the uncertainty is purely statistical. The time-dependent efficiency is calibrated using a control sample of $B^0 \rightarrow K^{*0}\gamma$ decays with statistics six times larger than the $B_s^0 \rightarrow \phi\gamma$ sample. An unbinned simultaneous fit to the $B_s^0 \rightarrow \phi\gamma$ and $B^0 \rightarrow K^{*0}\gamma$ decay time distributions is performed and A^Δ is measured to be:

$$A^\Delta = -0.98^{+0.46}_{-0.52}(\text{stat.})^{+0.23}_{-0.20}(\text{syst.}).\tag{7.2}$$

This result is compatible with the SM expectation within two standard deviations. This is the first time-dependent analysis of a radiative B_s^0 decays and the first experimental study of the photon polarisation in these decays.

Chapter 7. Conclusions

In order to extract the photon polarisation parameter λ_γ from the angular distributions of the hadronic final states in the $B^+ \rightarrow \phi K^+ \gamma$ decay, theoretical studies assume this system as a resonance with spin $J \geq 1$. The Belle collaboration studied the ϕK^+ invariant mass distributions using 144 $B^+ \rightarrow \phi K^+ \gamma$ events, and they found that the spectra is consistent with the perturbative QCD model prediction with nonresonant $B \rightarrow \phi K \gamma$ decays. Thus, to investigate the possibility of measuring the photon polarisation in this decay, the hadronic structure of the ϕK^+ -system is further studied as the first step. The signal $B^+ \rightarrow \phi K^+ \gamma$ decays are reconstructed using both calorimetric and converted photons. Background from $B^+ \rightarrow K^+ K^+ K^- \pi^0$ decays form the main experimental difficulty for the selection of signal candidates when calorimetric photons are used for decay reconstruction. The proposed strategy of fitting the γ/π^0 separation variable can disentangle effectively the signal radiative B decays from these backgrounds. Based on the data sample analysed, about 1400 signal $B^+ \rightarrow \phi K^+ \gamma$ decay candidates are reconstructed with calorimetric photons. No clear evidence of resonances in the ϕK^+ -system is found and the result presented in this analysis is qualitatively consistent with the studies performed by the Belle collaboration. Therefore, the chance of measuring the photon polarisation in this decay is small. Due to the good momentum resolution of converted photons, the reconstructed B invariant mass can be a good discriminating variable to separate signal from $B^+ \rightarrow K^+ K^+ K^- \pi^0$ decays when converted photons are used to reconstruct these decays. The total number of the $B^+ \rightarrow K^+ K^+ K^- \gamma$ decay candidates reconstructed with converted photons is found to be 53 ± 17 , which is not sufficient to perform further measurements. This result is consistent with the expected number of signal events when correcting the yield obtained from calorimetric photons with the photon conversion rate, the reconstruction efficiency and the $K^+ K^-$ mass range.

In addition, the direct CP asymmetry in the $B^+ \rightarrow \phi K^+ \gamma$ decay is measured to be

$$A_{CP}(B^+ \rightarrow \phi K^+ \gamma) = (1.6 \pm 2.1(\text{stat.}) \pm 0.7(\text{syst.}))\%. \quad (7.3)$$

This is the most precise measurement in this decay so far. This value is consistent with the SM prediction of $-(0.1 - 1)\%$.

To conclude, this thesis represents a further step into the ongoing efforts of using $b \rightarrow s \gamma$ transitions to probe beyond SM physics, a field that both benefits from current efforts and continues to be an interesting laboratory to search for new physics.

A The STRIPPING lines

Variables	LoKi functors	Selection cuts
Tracks p_T	PT	$> 500 \text{ MeV}/c$
Tracks p	P	$> 3000 \text{ MeV}/c$
Tracks Ghost Probability (GP)	TRGHOSTPROB	< 0.4
Tracks IP χ^2	MIPCHI2DV (PRIMARY)	> 16
Tracks χ^2/ndf	TRCHI2DOF	< 3
Photon E_T	PT	$> 2500 \text{ MeV}$
Photon CL	CL	> 0.25
Sum of p_T of the di-tracks	ASUM (PT)	$> 1500 \text{ MeV}/c$
Invariant mass of the combination of the di-tracks	AM	$< 2.5 \text{ GeV}$
Vertex χ^2 of the combination of the di-tracks	VFASPF (VCHI2/VDOF)	< 9
Mass window of the reconstructed K^{*0} candidates	ADMASS ('K*(892)0')	$< 150 \text{ MeV}/c^2$
Sum of p_T of the K^{*0} candidate + photon	ASUM (PT)	$> 5000 \text{ MeV}/c$
B^0 candidate invariant mass of the K^{*0} candidate + photon	AM	$\in [4000, 7000] \text{ MeV}/c^2$
Vertex χ^2 of the B^0 candidate	VFASPF (VCHI2/VDOF)	< 9
χ^2 -distance from the related PV for the B^0 candidate	BPVIPCHI2	< 9

Table A.1: A list of cuts applied in the STRIPPING line StrippingB2KstGamma_B2VG.

Appendix A. The STRIPPING lines

Variables	LoKi functors	Selection cuts
Tracks p_T	PT	$> 500 \text{ MeV}/c$
Tracks p	P	$> 3000 \text{ MeV}/c$
Tracks Ghost Probability (GP)	TRGHOSTPROB	< 0.4
Tracks IP χ^2	MIPCHI2DV (PRIMARY)	> 16
Tracks χ^2/ndf	TRCHI2DOF	< 3
Photon E_T	PT	$> 2500 \text{ MeV}$
Photon CL	CL	> 0.25
Sum of p_T of the di-tracks	ASUM (PT)	$> 1500 \text{ MeV}/c$
Invariant mass of the combination of the di-tracks	AM	$< 2.5 \text{ GeV}$
Vertex χ^2 of the combination of the di-tracks	VFASPF (VCHI2/VDOF)	< 9
Mass window of the reconstructed ϕ candidates	ADMASS ('phi (1020) ')	$< 15 \text{ MeV}/c^2$
Sum of p_T of the ϕ candidate + photon	ASUM (PT)	$> 5000 \text{ MeV}/c$
B_s^0 candidate invariant mass of the ϕ candidate + photon	AM	$\in [4000, 7000] \text{ MeV}/c^2$
Vertex χ^2 of the B_s^0 candidate	VFASPF (VCHI2/VDOF)	< 9
χ^2 -distance from the related PV for the B_s^0 candidate	BPVIPCHI2	< 9

Table A.2: A list of cuts applied in the STRIPPING line StrippingB2PhiGamma_B2VG.

Appendix A. The STRIPPING lines

Variables	LoKi functors	Selection cuts
Tracks p_T	PT	$> 300 \text{ MeV}/c$
Tracks p	P	$> 1000 \text{ MeV}/c$
Tracks Ghost Probability (GP)	TRGHOSTPROB	< 0.4
Tracks IP χ^2	MIPCHI2DV (PRIMARY)	> 16
Tracks χ^2/ndf	TRCHI2DOF	< 3
Photon E_T	PT	$> 2000 \text{ MeV}$
Photon CL	CL	> 0
At least one track matches the requirements in tri-tracks list exist	AHASCHILD (TRCHI2DOF <3 and PT $>500 \text{ MeV}/c$ and P $>5000 \text{ MeV}/c$)	True
Sum of p_T of the tri-tracks	ASUM(PT)	$> 1500 \text{ MeV}/c$
Invariant mass of the combination of the tri-tracks	AM	$\in [0,7900] \text{ MeV}/c^2$
p_T of the combination of the tri-tracks	PT	$> 150 \text{ MeV}/c$
Vertex χ^2 of the combination of the tri-tracks	VFASPF (VCHI2/VDOF)	< 10
χ^2 -distance from the related PV for the combination of the tri-tracks	BPVVDCHI2	> 0
Minimum χ^2 -distance of a particle's trajectory to PVs	MIPCHI2DV (PRIMARY)	> 0
Sum of p_T of the tri-tracks + photon	ASUM(PT)	$> 5000 \text{ MeV}/c$
B^\pm candidate invariant mass of the tri-tracks + photon	AM	$\in [2900,9000] \text{ MeV}/c^2$
Vertex χ^2 of the B^\pm candidate	VFASPF (VCHI2/VDOF)	< 9
χ^2 -distance from the related PV for the B^\pm candidate	BPVIPCHI2	< 9
$\cos\theta$ (θ : the angle between B^\pm momentum and the flight direction from the best PV to the decay vertex) of the B^\pm candidate	BPVDIRA	> 0

Table A.3: A list of cuts applied in the STRIPPING line StrippingB2XGamma3pi.

Appendix A. The STRIPPING lines

Variables	LoKi functors	Selection cuts
Tracks p_T	PT	$> 300 \text{ MeV/c}$
Tracks p	P	$> 1000 \text{ MeV/c}$
Tracks Ghost Probability (GP)	TRGHOSTPROB	< 0.4
Tracks IP χ^2	MIPCHI2DV (PRIMARY)	> 16
Tracks χ^2/ndf	TRCHI2DOF	< 3
Photon MM	MM	$< 100 \text{ MeV/c}^2$
Photon E_T	PT	$> 1000 \text{ MeV}$
Photon vertex χ^2 of the combination of the electron-position pairs	VFASPF (VCHI2/VDOF)	< 9
At least one track matches the requirements in tri-tracks list exist	AHASCHILD (TRCHI2DOF<3 and PT>500 MeV/c and P>5000 MeV/c)	True
Sum of p_T of the tri-tracks	ASUM(PT)	$> 1500 \text{ MeV/c}$
Invariant mass of the combination of the tri-tracks	AM	$\in [0, 7000] \text{ MeV/c}^2$
p_T of the combination of the tri-tracks	PT	$> 150 \text{ MeV/c}$
Vertex χ^2 of the combination of the tri-tracks	VFASPF (VCHI2/VDOF)	< 10
χ^2 -distance from the related PV for the combination of the tri-tracks	BPVVDCHI2	> 0
Minimum χ^2 -distance of a particle's trajectory to PVs	MIPCHI2DV (PRIMARY)	> 0
Sum of p_T of the tri-tracks + photon	ASUM(PT)	$> 5000 \text{ MeV/c}$
B^\pm candidate invariant mass of the tri-tracks + photon	AM	$\in [2900, 9000] \text{ MeV/c}^2$
Vertex χ^2 of the B^\pm candidate	VFASPF (VCHI2/VDOF)	< 9
χ^2 -distance from the related PV for the B^\pm candidate	BPVIPCHI2	< 9
$\cos\theta$ (θ : the angle between B^\pm momentum and the flight direction from the best PV to the decay vertex) of the B^\pm candidate	BPVDIRA	> 0

Table A.4: A list of cuts applied in the STRIPPING line StrippingB2XGamma3pi_wCNV.

Bibliography

- [1] A. Riotto and M. Trodden, *Recent progress in baryogenesis*, Annual Review of Nuclear and Particle Science **49** (1999), no. 1 35.
- [2] A. G. Cohen, A. D. Rújula, and S. L. Glashow, *A Matter-Antimatter Universe?*, The Astrophysical Journal **495** (1998), no. 2 539.
- [3] L. Canetti, M. Drewes, and M. Shaposhnikov, *Matter and antimatter in the universe*, New Journal of Physics **14** (2012), no. 9 095012.
- [4] N. Cabibbo, *Unitary Symmetry and Leptonic Decays*, Phys. Rev. Lett. **10** (1963) 531.
- [5] M. Kobayashi and T. Maskawa, *CP-Violation in the Renormalizable Theory of Weak Interaction*, Progress of Theoretical Physics **49** (1973), no. 2 652.
- [6] L. Wolfenstein, *Parametrization of the Kobayashi-Maskawa Matrix*, Phys. Rev. Lett. **51** (1983) 1945.
- [7] CKMfitter Group, *CKMfitter*, <http://ckmfitter.in2p3.fr>.
- [8] CKMfitter Group, J. Charles *et al.*, *Current status of the standard model CKM fit and constraints on $\Delta F = 2$ new physics*, Phys. Rev. D **91** (2015) 073007.
- [9] Super-Kamiokande collaboration, Y. Fukuda *et al.*, *Evidence for Oscillation of Atmospheric Neutrinos*, Phys. Rev. Lett. **81** (1998) 1562.
- [10] SNO collaboration, Q. R. Ahmad *et al.*, *Measurement of the Rate of $\nu_e + d \rightarrow p + p + e^-$ Interactions Produced by ^8B Solar Neutrinos at the Sudbury Neutrino Observatory*, Phys. Rev. Lett. **87** (2001) 071301.
- [11] G. Buchalla *et al.*, *B, D and K decays*, The European Physical Journal C **57** (2008), no. 1 309.
- [12] LHCb collaboration, *Roadmap for selected key measurements of LHCb*, LHCb-PUB-2009-029.
- [13] T. Blake, T. Gershon, and G. Hiller, *Rare b Hadron Decays at the LHC*, Annual Review of Nuclear and Particle Science **65** (2015), no. 1 113.

Bibliography

- [14] R. Ammar *et al.*, *Evidence for penguin-diagram decays: First observation of $B \rightarrow K^* (892) \gamma$* , Phys. Rev. Lett. **71** (1993) 674.
- [15] CLEO collaboration, M. S. Alam *et al.*, *First Measurement of the Rate for the Inclusive Radiative Penguin Decay $b \rightarrow s \gamma$* , Phys. Rev. Lett. **74** (1995) 2885.
- [16] BABAR collaboration, J. P. Lees *et al.*, *Precision Measurement of the $B \rightarrow X_s \gamma$ Photon Energy Spectrum, Branching Fraction, and Direct CP Asymmetry $A_{CP}(B \rightarrow X_{s+d} \gamma)$* , Phys. Rev. Lett. **109** (2012) 191801.
- [17] BABAR collaboration, J. P. Lees *et al.*, *Measurement of $\mathcal{B}(B \rightarrow X_s \gamma)$, the $B \rightarrow X_s \gamma$ photon energy spectrum, and the direct CP asymmetry in $B \rightarrow X_{s+d} \gamma$ decays*, Phys. Rev. D **86** (2012) 112008.
- [18] Belle collaboration, P. Koppenburg *et al.*, *Inclusive Measurement of the Photon Energy Spectrum in $b \rightarrow s \gamma$ Decays*, Phys. Rev. Lett. **93** (2004) 061803.
- [19] D. Atwood, M. Gronau, and A. Soni, *Mixing-Induced CP Asymmetries in Radiative B Decays in and beyond the Standard Model*, Phys. Rev. Lett. **79** (1997) 185.
- [20] D. Atwood, T. Gershon, M. Hazumi, and A. Soni, *Mixing-induced CP violation in $B \rightarrow P_1 P_2 \gamma$ in search of clean new physics signals*, Phys. Rev. D **71** (2005) 076003.
- [21] D. B. *et al.*, *Future prospects for the determination of the Wilson coefficient $C'_{7\gamma}$* , JHEP **08** (2012) 090.
- [22] V. D. Orlovsky and V. I. Shevchenko, *Photon polarization in radiative $B \rightarrow \phi K \gamma$ decay*, PRD **77** (2008) 093003.
- [23] M. Gronau, Y. Grossman, D. Pirjol, and A. Ryd, *Measuring the Photon Polarization in $B \rightarrow K \pi \pi \gamma$* , Phys. Rev. Lett. **88** (2002) 051802.
- [24] M. Gronau and D. Pirjol, *Photon polarization in radiative B decays*, Phys. Rev. D **66** (2002) 054008.
- [25] LHCb collaboration, R. A. *et al.*, *Observation of Photon polarisation in the $b \rightarrow s \gamma$ Transition*, PRL **112** (2014) 161801.
- [26] G. Hiller, M. Knecht, F. Legger, and T. Schietinger, *Photon polarization from helicity suppression in radiative decays of polarized Λ_b^0 to spin-3/2 baryons*, Phys. Lett. **B649** (2007) 152, arXiv:hep-ph/0702191.
- [27] F. Legger and T. Schietinger, *Photon helicity in $\Lambda_b^0 \rightarrow p K \gamma$ decays*, Physics Letters B **645** (2007), no. 2 - 3 204.
- [28] Heavy Flavor Averaging Group, Y. Amhis *et al.*, *Averages of b -hadron, c -hadron, and τ -lepton properties as of summer 2014*, arXiv:1412.7515, updated results and plots available at <http://www.slac.stanford.edu/xorg/hfag/>.

-
- [29] D. Atwood, T. Gershon, M. Hazumi, and A. Soni, *Clean Signals of CP-violating and CP-conserving New Physics in $B \rightarrow P V \gamma$ Decays at B Factories and Hadron Colliders*, arXiv:hep-ph/0701021.
 - [30] F. Krüger and J. Matias, *Probing new physics via the transverse amplitudes of $B^0 \rightarrow K^{*0}(\rightarrow K^- \pi^+) l^+ l^-$ at large recoil*, Phys. Rev. D **71** (2005) 094009.
 - [31] D. Bečirević and E. Schneider, *On transverse asymmetries in $B \rightarrow K^* e^+ e^-$* , Nuclear Physics B **854** (2012), no. 2 321 .
 - [32] Y. Grossman and D. Pirjol, *Extracting and using photon polarization information in radiative B decays*, Journal of High Energy Physics **2000** (2000), no. 06 029.
 - [33] S. Jäger and J. M. Camalich, *On $B \rightarrow V l l$ at small dilepton invariant mass, power corrections, and new physics*, Journal of High Energy Physics **2013** (2013), no. 5 1.
 - [34] LHCb collaboration, R. Aaij *et al.*, *Angular analysis of the $B^0 \rightarrow K^{*0} e^+ e^-$ decay in the low- q^2 region*, JHEP **04** (2015) 024, arXiv:1501.03038.
 - [35] F. Muheim, Y. Xie, and R. Zwicky, *Exploiting the width difference in $B_s \rightarrow \phi \gamma$* , Physics Letters B **664** (2008), no. 3 174 .
 - [36] LHCb collaboration, R. Aaij *et al.*, *Precision measurement of CP violation in $B_s^0 \rightarrow J/\psi K^+ K^-$ decays*, Phys. Rev. Lett. **114** (2015) 041801, arXiv:1411.3104.
 - [37] LHCb collaboration, R. Aaij *et al.*, *Measurement of the CP-violating phase ϕ_s in $\bar{B}_s^0 \rightarrow D_s^+ D_s^-$ decays*, Phys. Rev. Lett. **113** (2014) 211801, arXiv:1409.4619.
 - [38] LHCb collaboration, R. Aaij *et al.*, *Measurement of the CP-violating phase ϕ_s in the decay $B_s^0 \rightarrow J/\psi \phi$* , Phys. Rev. Lett. **108** (2012) 101803, arXiv:1112.3183.
 - [39] Particle Data Group, K. A. Olive *et al.*, *Review of particle physics*, Chin. Phys. **C38** (2014) 090001, and 2015 update.
 - [40] Belle collaboration, T. E. B. *et al.* . H.Šahoo, *First Observation of Radiative $B^0 \rightarrow \phi K^0 \gamma$ Decays and Measurements of Their Time-Dependent CP Violation*, PRD **84** 071101.
 - [41] LHCb collaboration, A. A. Alves Jr. *et al.*, *The LHCb detector at the LHC*, JINST **3** (2008) S08005.
 - [42] LHCb collaboration, R. Aaij *et al.*, *LHCb detector performance*, Int. J. Mod. Phys. **A30** (2015) 1530022, arXiv:1412.6352.
 - [43] S. Amato *et al.*, *LHCb magnet: Technical Design Report*, Technical Design Report LHCb, CERN, Geneva, 2000.
 - [44] P. R. Barbosa-Marinho *et al.*, *LHCb VELO (Vertex Locator): Technical Design Report*, Technical Design Report LHCb, CERN, Geneva, 2001.

Bibliography

- [45] R. Aaij *et al.*, *Performance of the LHCb Vertex Locator*, JINST **9** (2014) P09007, arXiv:1405.7808.
- [46] LHCb collaboration, *LHCb reoptimized detector design and performance: Technical Design Report*, CERN-LHCC-2003-030. LHCb-TDR-009.
- [47] LHCb collaboration, *LHCb inner tracker: Technical Design Report*, CERN-LHCC-2002-029. LHCb-TDR-008.
- [48] LHCb collaboration, *LHCb outer tracker: Technical Design Report*, CERN-LHCC-2001-024. LHCb-TDR-006.
- [49] R. Arink *et al.*, *Performance of the LHCb Outer Tracker*, JINST **9** (2014) P01002, arXiv:1311.3893.
- [50] E. Rodrigues, *Tracking definitions*, Tech. Rep. LHCb-2007-006. CERN-LHCb-2007-006, CERN, Geneva, Feb., 2007. revised version submitted on 2007-03-28 09:34:37.
- [51] LHCb collaboration, R. Aaij *et al.*, *Measurement of the track reconstruction efficiency at LHCb*, JINST **10** (2015) P02007, arXiv:1408.1251.
- [52] S. Amato *et al.*, *LHCb RICH: Technical Design Report*, Technical Design Report LHCb, CERN, Geneva, 2000.
- [53] M. Adinolfi *et al.*, *Performance of the LHCb RICH detector at the LHC*, Eur. Phys. J. **C73** (2013) 2431, arXiv:1211.6759.
- [54] S. Amato *et al.*, *LHCb calorimeters: Technical Design Report*, Technical Design Report LHCb, CERN, Geneva, 2000.
- [55] R. Aaij *et al.*, *Performance of the LHCb calorimeters*, LHCb-DP-2013-004, in preparation.
- [56] O. Deschamps *et al.*, *Photon and neutral pion reconstruction*, Tech. Rep. LHCb-2003-091, CERN, Geneva, Sep, 2003.
- [57] P. R. Barbosa-Marinho *et al.*, *LHCb muon system: Technical Design Report*, Technical Design Report LHCb, CERN, Geneva, 2001.
- [58] A. A. Alves Jr. *et al.*, *Performance of the LHCb muon system*, JINST **8** (2013) P02022, arXiv:1211.1346.
- [59] F. Archilli *et al.*, *Performance of the muon identification at LHCb*, JINST **8** (2013) P10020, arXiv:1306.0249.
- [60] R. Antunes-Nobrega *et al.*, *LHCb trigger system: Technical Design Report*, Technical Design Report LHCb, CERN, Geneva, 2003. revised version number 1 submitted on 2003-09-24 12:12:22.

-
- [61] R. Aaij *et al.*, *The LHCb trigger and its performance in 2011*, JINST **8** (2013) P04022, arXiv:1211.3055.
- [62] *The Gaudi project*, <http://proj-gaudi.web.cern.ch/proj-gaudi/>. project web page.
- [63] G. Barrand *et al.*, *GAUDI - The software architecture and framework for building LHCb data processing applications*, in *Proceedings, 11th International Conference on Computing in High-Energy and Nuclear Physics (CHEP 2000)*, pp. 92–95, 2000.
- [64] *The Gauss project*, <http://lhcb-release-area.web.cern.ch/LHCb-release-area/DOC/gauss/>. project web page.
- [65] I. Belyaev *et al.*, *Handling of the generation of primary events in Gauss, the LHCb simulation framework*, J. Phys. Conf. Ser. **331** (2011) 032047.
- [66] T. Sjöstrand, S. Mrenna, and P. Skands, *Pythia 6.4 physics and manual*, Journal of High Energy Physics **2006** (2006), no. 05 026.
- [67] T. Sjöstrand, S. Mrenna, and P. Skands, *A brief introduction to PYTHIA 8.1*, Comput. Phys. Commun. **178** (2008) 852, arXiv:0710.3820.
- [68] A. Ryd *et al.*, *EvtGen: A Monte Carlo Generator for B-Physics*, , EVTGEN-V00-11-07.
- [69] D. J. Lange, *The EvtGen particle decay simulation package*, Nucl. Instrum. Meth. **A462** (2001) 152.
- [70] P. Golonka and Z. Was, *PHOTOS Monte Carlo: A precision tool for QED corrections in Z and W decays*, Eur. Phys. J. **C45** (2006) 97, arXiv:hep-ph/0506026.
- [71] Geant4 collaboration, S. Agostinelli *et al.*, *Geant4: A simulation toolkit*, Nucl. Instrum. Meth. **A506** (2003) 250.
- [72] *The Boole project*, <http://lhcb-release-area.web.cern.ch/LHCb-release-area/DOC/boole/>. project web page.
- [73] *The Moore project*, <http://lhcb-release-area.web.cern.ch/LHCb-release-area/DOC/moore/>. project web page.
- [74] *The Brunel project*, <http://lhcb-release-area.web.cern.ch/LHCb-release-area/DOC/brunel/>. project web page.
- [75] *The DaVinci project*, <http://lhcb-release-area.web.cern.ch/LHCb-release-area/DOC/davinci/>. project web page.
- [76] G. Barrand *et al.*, *The LHCb detector description framework*, in *Proceedings, 11th International Conference on Computing in High-Energy and Nuclear Physics (CHEP 2000)*, pp. 96–100, 2000.
- [77] *Extensible Markup Language (XML)*, <http://www.w3.org/XML>.

Bibliography

- [78] *The STRIPPING project*, <http://lhcb-release-area.web.cern.ch/LHCb-release-area/DOC/stripping/>. project web page.
- [79] M. Martinelli, *Tracking and Alignment of the LHCb detector*, LHCb-PROC-2014-062. CERN-LHCb-PROC-2014-062.
- [80] F. G. Dupertuis, *Measurement of b -hadron lifetimes and the calibration and performance of the LHCb tracking system*, PhD thesis, École Polytechnique Fédérale de Lausanne, 2014, CERN-THESIS-2014-059.
- [81] O. Callot, *FastVelo, a fast and efficient pattern recognition package for the Velo*, Tech. Rep. LHCb-PUB-2011-001. CERN-LHCb-PUB-2011-001, CERN, Geneva, Jan, 2011. LHCb.
- [82] G. Conti *et al.*, *Inner Tracker Survey Strategy*, Tech. Rep. LHCb-2008-068. CERN-LHCb-2008-068, CERN, Geneva, Dec, 2008.
- [83] R. Aaij *et al.*, *Tesla : an application for real-time data analysis in High Energy Physics*, Tech. Rep. arXiv:1604.05596. CERN-LHCB-DP-2016-001, Apr, 2016. Comments: 14 pages, 8 figures.
- [84] J. Amoraal *et al.*, *Application of vertex and mass constraints in track-based alignment*, Nucl. Instrum. Meth. **A712** (2013) 48, arXiv:1207.4756.
- [85] W. Hulsbergen, *The Global covariance matrix of tracks fitted with a Kalman filter and an application in detector alignment*, Nucl. Instrum. Meth. **A600** (2009) 471, arXiv:0810.2241.
- [86] G. Dujany and B. Storaci, *Real-time alignment and calibration of the LHCb Detector in Run II*, J. Phys. : Conf. Ser. **664** (2015) 082010. 8 p.
- [87] *The LHCb logbooks for LHC Run 2*, <http://lblogbook.cern.ch>.
- [88] I. Belyaev *et al.*, *Kali: The framework for fine calibration of the LHCb Electromagnetic Calorimeter*, Journal of Physics: Conference Series **331** (2011), no. 3 032050.
- [89] M. Calvo *et al.*, *First measurement of the photon polarization in radiative B_s^0 decays*, LHCb-ANA-2014-102.
- [90] A. Puig, *The LHCb trigger in 2011 and 2012*, LHCb-PUB-2014-046.
- [91] L. Anderlini *et al.*, *The PIDCalib package*, Tech. Rep. LHCb-PUB-2016-021. CERN-LHCb-PUB-2016-021, CERN, Geneva, Jul, 2016.
- [92] *PIDCalib Packages*, <https://twiki.cern.ch/twiki/bin/view/LHCb/PIDCalibPackage>.
- [93] M. Calvo Gomez *et al.*, *A tool for γ/π^0 separation at high energies*, LHCb-PUB-2015-016. CERN-LHCb-PUB-2015-016.

-
- [94] LHCb collaboration, *b-hadron lifetime measurements with exclusive $b \rightarrow J/\psi X$ decays reconstructed in the 2010 data*, LHCb-CONF-2011-001.
 - [95] Y. Amhis *et al.*, *Understanding decay time acceptances in $B_s^0 \rightarrow J/\psi \phi$ decays*, LHCb-ANA-2013-008.
 - [96] LHCb collaboration, R. Aaij *et al.*, *Measurements of the B^+ , B^0 , B_s^0 meson and Λ_b^0 baryon lifetimes*, JHEP **04** (2014) 114, arXiv:1402.2554.
 - [97] LHCb collaboration, R. Aaij *et al.*, *Measurement of the ratio of branching fractions $\mathcal{B}(B^0 \rightarrow K^{*0} \gamma)/\mathcal{B}(B_s^0 \rightarrow \phi \gamma)$ and the direct CP asymmetry in $B^0 \rightarrow K^{*0} \gamma$* , Nucl. Phys. **B867** (2013) 1, arXiv:1209.0313.
 - [98] O. Deschamps and A. Puig Navarro, *Measurement of the ratio of branching fractions $B(B^0 \rightarrow K^{*0} \gamma)/B(B_s^0 \rightarrow \phi \gamma)$ and direct CP violation in $B^0 \rightarrow K^{*0} \gamma$* , LHCb-CONF-2012-004.
 - [99] T. Skwarnicki, *A study of the radiative cascade transitions between the Upsilon-prime and Upsilon resonances*, PhD thesis, Institute of Nuclear Physics, Krakow, 1986, DESY-F31-86-02.
 - [100] Ali *et al.*, *Charmless non-leptonic B_s decays to PP, PV and VV final states in the pQCD approach*, Phys. Rev. **D76** (2007) 074018, arXiv:0703162.
 - [101] LHCb collaboration, *Measurement of the direct CP asymmetry in the $B_d^0 \rightarrow K^{*0} \gamma$ decay*, LHCb-CONF-2012-004.
 - [102] ARGUS collaboration, H. Albrecht *et al.*, *Search for hadronic $b \rightarrow u$ decays*, Phys. Lett. **B241** (1990) 278.
 - [103] L. Demortier, *Constructing Ensembles of Pseudo-Experiments*, physics/0312100. Comments: Talk from PhyStat2003, Stanford, CA, USA, September 2003, 5 pages, LaTeX, no figures, PSN WEMT003.
 - [104] N. Brook, *LHCb Computing Model*, Tech. Rep. LHCb-2004-119. CERN-LHCb-2004-119, CERN, Geneva, Dec, 2004.
 - [105] LHCb collaboration, R. Aaij *et al.*, *Precision measurement of the $B_s^0 - \bar{B}_s^0$ oscillation frequency in the decay $B_s^0 \rightarrow D_s^- \pi^+$* , New J. Phys. **15** (2013) 053021, arXiv:1304.4741.
 - [106] LHCb collaboration, R. Aaij *et al.*, *Measurement of CP asymmetry in $B_s^0 \rightarrow D_s^\mp K^\pm$ decays*, JHEP **11** (2014) 060, arXiv:1407.6127.
 - [107] H.-G. Moser and A. Roussarie, *Mathematical methods for $B^0 - \bar{B}^0$ oscillation analyses*, Nuclear Instruments and Methods in Physics Research Section A: Accelerators, Spectrometers, Detectors and Associated Equipment **384** (1997), no. 2 491.

Bibliography

- [108] M. Pivk and F. R. Le Diberder, *sPlot: A statistical tool to unfold data distributions*, Nucl. Instrum. Meth. **A555** (2005) 356, arXiv:physics/0402083.
- [109] Y. Xie, *sFit: a method for background subtraction in maximum likelihood fit*, ArXiv e-prints (2009) arXiv:0905.0724.
- [110] LHCb collaboration, *First experimental study of the photon polarization in radiative B_s^0 decays*, LHCb-PAPER-2016-034. CERN-EP-2016-210.
- [111] LHCb collaboration, R. Aaij *et al.*, *Measurement of the \bar{B}^0-B^0 and $\bar{B}_s^0-B_s^0$ production asymmetries in pp collisions at $\sqrt{s} = 7$ TeV*, Phys. Lett. **B739** (2014) 218, arXiv:1408.0275.
- [112] D. Martínez Santos and F. Dupertuis, *Mass distributions marginalized over per-event errors*, Nucl. Instrum. Meth. **A764** (2014) 150, arXiv:1312.5000.
- [113] K. Cranmer, *Kernel estimation in high-energy physics*, Computer Physics Communications **136** (2001), no. 3 198.
- [114] BABAR collaboration, B. A. *et al.*, *Measurement of B Decays to $\phi K \gamma$* , PRD **75** 051102.
- [115] LHCb collaboration, R. Aaij *et al.*, *Measurements of time-integrated asymmetries in $D^0 \rightarrow K^- K^+$ and $D^0 \rightarrow \pi^- \pi^+$ decays*, LHCb-PAPER-2015-055, in preparation.
- [116] B. P. Roe *et al.*, *Boosted decision trees as an alternative to artificial neural networks for particle identification*, Nuclear Instruments and Methods in Physics Research Section A: Accelerators, Spectrometers, Detectors and Associated Equipment **543** (2005), no. 2–3 577.
- [117] F. Pedregosa *et al.*, *Scikit-learn: Machine Learning in Python*, Journal of Machine Learning Research **12** (2011) 2825.
- [118] M.-H. Schune, F. Polci, and M. Borsato, *HOP an additional tool for decays involving electrons*, Tech. Rep. LHCb-INT-2015-037. CERN-LHCb-INT-2015-037, CERN, Geneva, Nov, 2015.
- [119] LHCb collaboration, R. Aaij *et al.*, *Measurement of CP asymmetry in $D^0 \rightarrow K^- K^+$ and $D^0 \rightarrow \pi^- \pi^+$ decays*, JHEP **07** (2014) 041, arXiv:1405.2797.
- [120] LHCb collaboration, R. Aaij *et al.*, *Measurement of CP asymmetries in the decays $B^0 \rightarrow K^{*0} \mu^+ \mu^-$ and $B^+ \rightarrow K^+ \mu^+ \mu^-$* , JHEP **09** (2014) 177, arXiv:1408.0978.
- [121] J. M. Soares, *CP violation in radiative b decays*, Nuclear Physics B **367** (1991), no. 3 575.
- [122] C.-H. Chen and H.-n. Li, *Vector-pseudoscalar two-meson distribution amplitudes in three-body B meson decays*, Phys. Rev. D **70** (2004) 054006.
- [123] E. Tournefier, *Converted photons: selection, efficiency and angular distribution studies*, Tech. Rep. LHCb-INT-2015-040. CERN-LHCb-INT-2015-040, CERN, Geneva, Nov, 2015.

- [124] LHCb collaboration, R. Aaij *et al.*, *Measurement of the relative rate of prompt χ_{c0} , χ_{c1} and χ_{c2} production at $\sqrt{s} = 7$ TeV*, JHEP **10** (2013) 115, arXiv:1307.4285.
- [125] A. Blum, A. Kalai, and J. Langford, *Beating the hold-out: Bounds for k -fold and progressive cross-validation*, in *Proceedings of the Twelfth Annual Conference on Computational Learning Theory*, COLT '99, (New York, NY, USA), pp. 203–208, ACM, 1999. doi: 10.1145/307400.307439.

Zhirui Xu

Laboratory for High Energy Physics (LPHE),
École Polytechnique Fédérale de Lausanne,
CH-1015 Lausanne, Switzerland.

Education and Research

September.2012 - October.2016, **PhD**, École Polytechnique Fédérale de Lausanne, Lausanne, Switzerland.

Thesis: Searches for the anomalous photon polarisation in radiative B decays at LHCb
Experience in data analysis, the LHCb detector alignment and photonic detector R&D.

September.2009 - June.2012, **M.Sc.**, University of Science and Technology of China, Hefei, China.

Thesis: Study of $\chi_{cJ} \rightarrow \phi K \bar{K} \pi$ with the BESIII detector at BEPCII
Experience in data analysis and software development.

August.2005 - July.2009, **B.S. Physics**, University of Science and Technology of China, Hefei, China.

List of Publications

1. R. Aaij et al. (LHCb collaboration), "First experimental study of photon polarization in radiative B_s^0 decays", [arXiv:1609.02032](#) (submitted to PRL).
2. Z. Xu and M. Tobin, on behalf of the LHCb collaboration, "Novel Real-time Alignment and Calibration of the LHCb Detector in Run II" ([poster](#)), doi : 10.1016/j.nima.2015.11.040 ([proceedings](#)), Frontier Detectors for Frontier Physics (13th Pisa Meeting on Advanced Detectors), La Biodola, Isola d'Elba (Italy), 24-30 May 2015.
3. Z. Xu and G. Haefeli, on behalf of the LHCb SciFi Tracker group, "Silicon Photomultipliers for the LHCb Upgrade Scintillating Fibre Tracker", PoS(TIPP2014)071 ([proceedings](#)) TIPP2014 – Third International Conference on Technology and Instrumentation in Particle Physics, Beurs van Berlage, 2-6 June 2014.
4. The LHCb collaboration, The Tracker TDR for the LHCb upgrade, [CERN-LHCC-2014-001](#).
5. The LHCb SciFi group, "Viability assessment of a scintillating fibre tracker for the LHCb upgrade", [CERN-LHCb-PUB-2014-015](#).
6. S. Gianì, G. Haefeli, C. Joram, M. Tobin and Z. Xu, "Digitization of SiPM signals for the LHCb Upgrade SciFi tracker", [LHCb-PUB-2014-025](#).
7. M. Ablikim et al. (BESIII collaboration), "Study of χ_{cJ} decaying into $\phi K^*(892)K$ ", *Phys. Rev. D* **91**, 112008 (2015).
8. Xu Zhi-Rui and He Kang-Lin, "A photon conversion finder at BESIII", *Chinese Phys. C* **36** 742 (2012).